

N70-35505-514

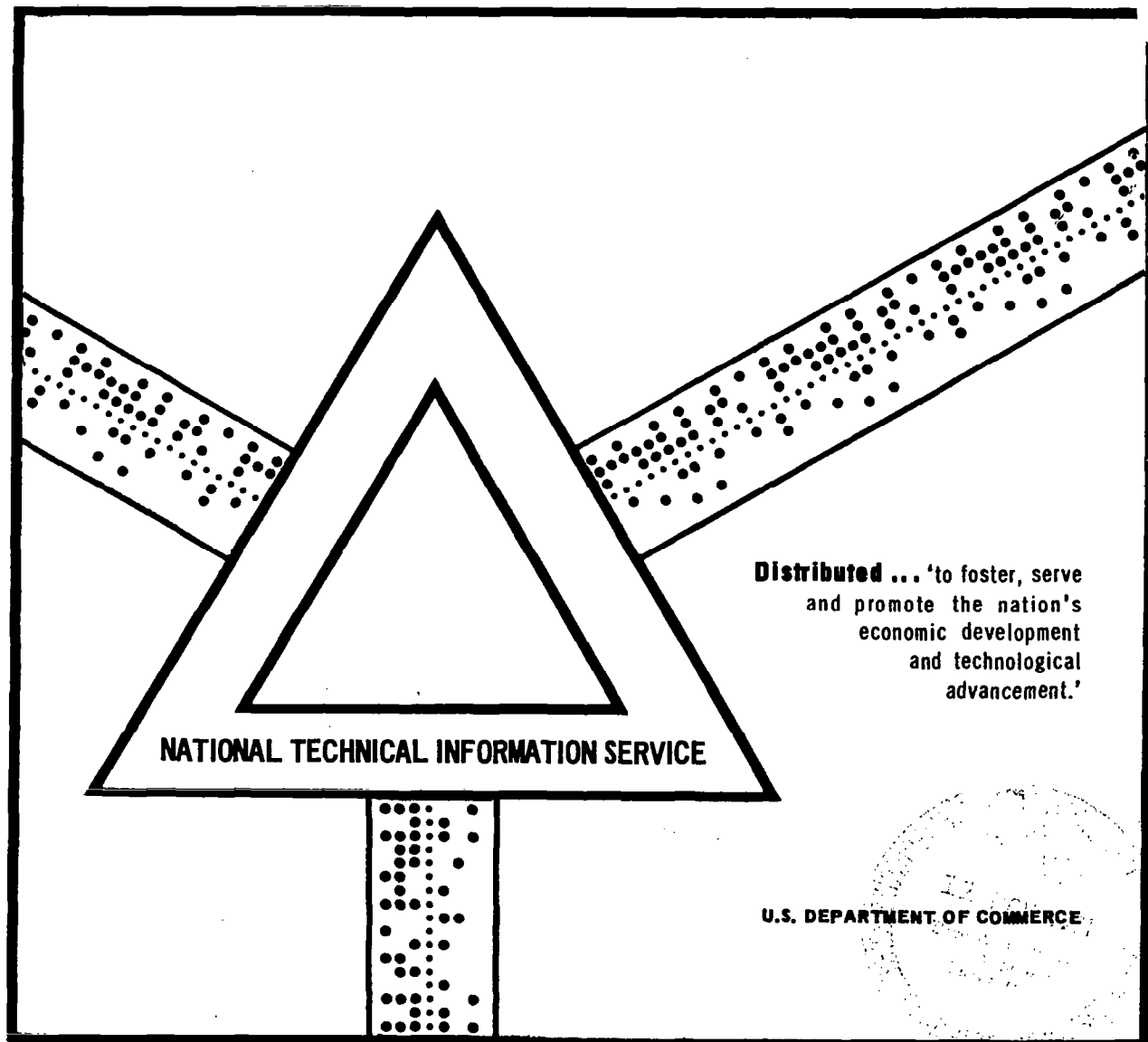
RESEARCH ACHIEVEMENTS REVIEW-VOLUME III-
REPORT NUMBER 8

1969

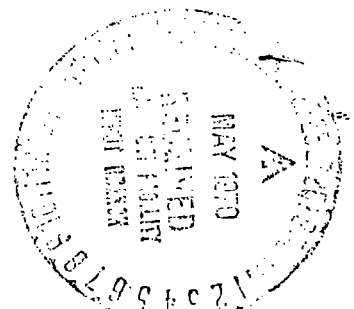
NASA
TM-X
53620
v.3
c.1

LOAN COPY: RETURN TO
AFWL (DOUL)
KIRTLAND AFB, N.

TECH LIBRARY KAFB, NM
0152447



This document has been approved for public release and sale.



NATIONAL AERONAUTICS AND SPACE ADMINISTRATION
WASHINGTON, D. C.

RESEARCH ACHIEVEMENTS REVIEW
VOLUME III **REPORT NO. 8**

METEOROID PHYSICS RESEARCH AT MSFC

SCIENCE AND ENGINEERING DIRECTORATE
GEORGE C. MARSHALL SPACE FLIGHT CENTER
MARSHALL SPACE FLIGHT CENTER, ALABAMA

PREFACE

In February, 1965, Dr. Ernst Stuhlinger, now Marshall Space Flight Center's Associate Director for Science, initiated a series of Research Achievements Reviews which set forth those achievements accomplished by the laboratories of the Marshall Space Flight Center. Each review covered one or two fields of research in a form readily usable by specialists, systems engineers and program managers. The review of February 24, 1966, completed this series. Each review was documented in the "Research Achievements Review Series."

In March, 1966, a second series of Research Achievements Reviews was initiated. This second series emphasized research areas of greatest concentration of effort, of most rapid progress, or of most pertinent interest and was published as "Research Achievements Review Reports, Volume II." Volume II covered the reviews from March, 1966, through February, 1968.

This third series of Research Achievements Reviews was begun in March, 1968, and continues the concept introduced in the second series. Reviews of the third series are designated Volume III and will span the period from March, 1968, through March, 1970.

The papers in this report were presented June 26, 1969

William G. Johnson
Director
Research Planning Office

INTRODUCTION TO METEOROID PHYSICS RESEARCH

By R. J. Naumann

	Page
INTRODUCTION.	1
ACKNOWLEDGMENTS	3

LIST OF TABLES

Table	Title	Page
1.	Energetics of Meteoroid Encounter	1

LIST OF ILLUSTRATIONS

Figure	Title	Page
1.	Summary of various proposed meteoroid environmental models	2
2.	Current meteoroid environment	3

LIGHT GAS GUN EXPERIMENTS

By David Jex

	Page
FACILITY DESCRIPTION	5
EXPERIMENTS CONDUCTED.	5

LIST OF TABLES

Table	Title	Page
1.	Areas of Involvement and Specific Experiments Conducted.	6

LIST OF ILLUSTRATIONS

Figure	Title	Page
1.	Simulated meteoroid impact on solar cell panel	6
2.	Simulated meteoroid impact of bumper shield configuration	7

CONTENTS (Continued). . .

	Page
3. Bumper shield and secondary surface damage.	8
4. Results of bumper shield test series	8
5. Comparison of normalized results of the bumper shield test series with a similar independent study	9
6. Results of honeycomb material test series	10
7. Relation of failure area to impact point for honeycomb material test series	10
8. Results of calibration tests on Pegasus panels	11
9. Output waveform profiles of Pegasus panels	11
10. Target configuration for dielectric study	12
11. Electromagnetic disturbance waveform associated with dielectric study	12

SIMULATED METEOROID IMPACT TESTING ON MDA CONFIGURATION

By R. C. Ruff

	Page
SUMMARY	15
INTRODUCTION	15
HYPERVELOCITY LAUNCH TECHNIQUES.	15
PENETRATION TESTS.	17
CURRENT RESEARCH	25
CONCLUSIONS	29
REFERENCE	29

LIST OF ILLUSTRATIONS

Figure	Title	Page
1.	Materials Division Meteoroid Simulation Facility	16
2.	Schematic diagram of range tank	17
3.	Schematic diagram of improved sabot stripper	18
4.	Target configuration for MDA wall penetration tests	19

CONTENTS (Continued). . .

	Page
5. Impact test on MDA Series 1.	19
6. Basic MDA configuration compared both to magnesium bumper and to no insulation	20
7. Basic MDA configuration compared to 0.635-cm (0.250-in.) backup.	21
8. Example of damage when no insulation was used.	22
9. Example of damage when insulation was used.	23
10. Target configuration for MDA external electrical cable tunnel tests.	24
11. Example of damage received by cable when protected only by bumper	25
12. Target configuration for MDA window bumper tests	26
13. Window condition immediately after test (left) and after being wiped with dry cloth (right) . . .	26
14. Window after cleaning with alcohol.	27
15. Multilayers of aluminum foil and high density foam.	28
16. Multilayers of aluminum foil and cork	28
17. Multilayers of aluminum foil and red polyurethane foam	29
18. Multilayers of aluminized mylar and red polyurethane foam	29
19. Multilayer target density versus both penetrated thickness and areal density.	30
20. Bumper penetration as photographed by an image converter sequence camera	30
21. Sequential views of a complete penetration of bumper and backup plate.	31

MHD ACCELERATOR RESEARCH

	Page
By Patrick N. Espy.	33

LIST OF ILLUSTRATIONS

Figure	Title	Page
1.	Plasma range showing firing console	34
2.	Plasma range from other side.	34
3.	250 kJ capacitor bank	35
4.	Coaxial gun presently in use.	35

CONTENTS (Continued) . . .

	Page
5. Plasma range with coaxial gun installed.	36
6. Self-luminous plasma emerging from coaxial gun	36

IMPACT CODE DEVELOPMENT

	Page
By R. J. Naumann	37

LIST OF ILLUSTRATIONS

Figure	Title	Page
1.	Computer studies of impact phenomena represent the material by a series of imaginary mass points. As the impact progresses, the motion of these mass points indicates the material flow. The regions where the mass points cluster to form the darker areas are regions in which the material has been compressed by the strong shock waves generated by the impact. Such shock pressures can be as high as 100 million atmospheres (many times the pressure at the center of the earth). Material behavior at such pressures can be determined from quantum mechanical calculations and has been measured at more modest pressures (1 to 2 million atmospheres) by controlled shock experiments	37
2.	Dynamic pressure profiles.	38
3.	Penetration versus impact velocity	39
4.	Decay of the maximum value of σ_{zz} at the axis with distance into the target	39
5.	Two-wave shock structure approaching pellet at rear surface of target	40
6.	Comparison of crater and splash for different size profiles at scaled times of $U_0 t/D = 3, 6$ and $10, 8$	40

SHOCK PROPAGATION IN SOLIDS IN HYPERVELOCITY IMPACT

By Tsun-Sen Fu

	Page
INTRODUCTION	41
THEORETICAL MODEL OF IMPACT-GENERATED SHOCK PROPAGATION IN SOLID MEDIA	42
FORMULATION OF THE CHARACTERISTIC EQUATIONS	43
HUGONOT RELATIONS OF SHOCK WAVES IN SOLID MEDIA	47
SHOCK PROPAGATION LAWS	49

	Page
SHOCK WAVE INTERACTION WITH FREE BOUNDARY.	50
CONSTRUCTION OF NUMERICAL SOLUTIONS FOR SHOCK WAVE PROPAGATIONS	51
AN APPROXIMATION FOR PRESSURE PULSE AT LATE STAGE OF IMPACT	53
NUMERICAL RESULTS AND DISCUSSION.	55
APPENDIX: SOUND SPEED OF c,s MATERIAL BEHIND THE SHOCK	59
REFERENCES	60

LIST OF TABLES

Table	Title	Page
1.	Shock and Adiabatic Sound Speed Constants for Aluminum	49

LIST OF ILLUSTRATIONS

Figure	Title	Page
1.	General features of the hypervelocity impact mechanism	42
2.	Moving shock front in a suddenly enlarged channel	42
3.	Ray tube coordinates system.	43
4.	Geometric relation of equations (2) and (3) for the two-dimensional case	43
5.	Mach angle in physical plane.	44
6.	Relation of (x, y) plane and (β , t) plane	45
7.	Sketch of shock propagation in solid medium (t_c is the time when the first characteristic line reaches the shock centerline, x - axis; the normal shock portion vanishes completely for $t \geq t_c$)	45
8.	Basic coordinate system of axisymmetric case	46
9.	Geometric relation for axisymmetric cases.	46
10.	The ratio of adiabatic sound speed and the scope of Rankine-Hugoniot curve as a function of shock Mach number for c,s material	48
11.	Shock wave and free surface interaction	51
12.	Impact-generated normal shock waves	52

CONTENTS (Continued). . .

	Page
13. Construction of a simple wave solution.	52
14. Approximate shock profile for the strong shock situation (U large).	53
15. Spherical coordinate system with symmetric axis	54
16. The starting point of shock curvature in aluminum	56
17. Numerical example of aluminum impact on aluminum at a velocity of 20 km/sec	57
18. Comparison of peak pressure distribution for an aluminum-on-aluminum impact (impact velocity is 20 km/sec)	58
19. Angular pressure distribution.	58

ONE-DIMENSIONAL MODEL FOR INVESTIGATION OF CHANGES IN CONDUCTIVITY OF DIELECTRICS UNDER SHOCK CONDITIONS

By E. E. Klingman

	Page
ABSTRACT.	63
INTRODUCTION	63
MODEL FOR CALCULATIONS	63
CONCLUSIONS.	76
REFERENCES	76

LIST OF TABLES

Table	Title	Page
1.	Clebsch-Jordan Coefficients.	69

LIST OF ILLUSTRATIONS

Figure	Title	Page
1.	Formation of bands.	64
2.	Energy bands for crystal with N atoms of $1s^2 2s^1$ configuration	64
3.	Four general types of band structure	65

CONTENTS (Continued) . . .

	Page
4. An illustration of the difference in discrete and continuous energies of single atom and continuous energy bands and forbidden energies of periodic potential.	65
5. Model chosen to determine $V_1(\alpha)$	66
6. Coordinate system for ion-atom pairs	67
7. Additive energy as a function of lattice parameter	68
8. Slater representation of crystal potential	70
9. Potential energy of electron in hydrogen and alkali atoms	70
10. Variation of potential as a function of lattice parameter.	71
11. Illustrating n-dependence of bandwidth	72
12. Energy band structure for model used	72
13. Alternate method of depicting energy gaps resulting from model.	73
14. Different possibilities of overlapping wave functions.	75

✓ HIGH TEMPERATURE EQUATION OF STATE FOR ALUMINUM

By R. J. Naumann

	Page
SUMMARY.	79
INTRODUCTION.	79
FORMULATION	80
COMPUTATIONAL RESULTS	85
CONCLUSIONS.	92
REFERENCES	93

LIST OF TABLES

Table	Title	Page
1.	Summary of Hugoniot Data for Aluminum	91

CONTENTS (Continued) . . .

LIST OF ILLUSTRATIONS

Figure	Title	Page
1.	Comparison of solid and liquid potentials.	83
2.	Behavior of heat capacity for solids and liquids in the high temperature regime	85
3.	Transition of heat capacity from liquid to gaseous behavior	86
4.	Gibbs energy isotherms.	87
5.	Melting curve deduced from Gibbs energy plot	87
6.	Pressure isotherms	88
7.	Energy isotherms	89
8.	Isotherms on S-V plot	89
9.	Isoenergy lines.	89
10.	D-u plots comparing computed results with experimental data points	90
11.	P-u plots comparing computed results with experimental data points	90
12.	T-u plots.	92
13.	S-u plots	92

LOW LIGHT LEVEL TV OBSERVATIONS

	Page
By Stuart Clifton.	95

LIST OF ILLUSTRATIONS

Figure	Title	Page
1.	Image orthicon and accessory equipment mounted in the DC-3 for airborne meteor observations	96
2.	A meteor as observed by the image orthicon system	97
3.	An angular rate distribution of meteors as recorded by the image orthicon during observations throughout November, 1969.	97
4.	The decrease in apparent brightness of an object with increasing angular velocity	98
5.	A typical peak-height light curve as recorded by a photomultiplier tube observing the television monitor	98

✓ PHOTOELECTRIC OBSERVATIONS OF METEORS TO 6.4 MAGNITUDE

By R. J. Naumann

	Page
SUMMARY.	101
INTRODUCTION.	101
THEORETICAL LIMIT OF A PHOTOMULTIPLIER METEOR DETECTION SYSTEM.	101
CALIBRATION.	105
METEOR OBSERVATIONS.	106
CONCLUSIONS.	110
REFERENCES.	110

LIST OF TABLES

Table	Title	Page
1.	Meteors Observed in 17 Hours, 22 Minutes Observing Time.	109

LIST OF ILLUSTRATIONS

Figure	Title	Page
1.	120-Hz sky background and level shift caused by a 3.45 magnitude meteor (50 mV/cm, 10 ms/cm)	107
2.	a. Typical meteors observed — 3.58-magnitude meteor (50 mV/cm, 100 ms/cm)	107
	b. 5.16-magnitude meteor (50 mV/cm, 50 ms/cm).	107
	c. 4.5-magnitude meteor (50 mV/cm, 50 ms/cm)	107
3.	Results of this study compared with photographic work of Hawkins and Upton	108
4.	Filter attenuation at different pulse durations	108
5.	Influx rates of this study compared with those observed by Hawkins and Upton.	110

CONTENTS (Concluded). . .

OBSERVATORY PLANS AND ASTRONOMICAL APPLICATIONS

	Page
By James McGuire	111

LIST OF TABLES

Table	Title	Page
1.	Observational Conditions of Observatory Site.	111

LIST OF ILLUSTRATIONS

Figure	Title	Page
1.	Location of observatory site at Redstone Arsenal.	111
2.	View of eastern horizon from observatory site.	112
3.	View of southern horizon from observatory site.	112
4.	View of western horizon from observatory site	113
5.	View of northern horizon from observatory site	113
6.	12-foot diameter dome located at observatory site	114
7.	Ferson telescope having a 16-inch primary mirror	114
8.	Celestron Pacific telescope	115
9.	Celestron telescope with a low light level TV camera and rich field adaptor attached	116

INTRODUCTION TO METEOROID PHYSICS RESEARCH

By

R. J. Naumann

INTRODUCTION

Since the time man first began to seriously consider spaceflight, it was recognized that the existence of small bits of material in space ranging from micron-size dust to huge boulders presented a possible hazard to space vehicles. This hazard results from the extremely high relative velocities of the particles, ranging from earth escape (11 km/sec) to parabolic retrograde (72 km/sec), with an average of approximately 20 km/sec. The energetics of impacts at these velocities are summarized in Table 1.

Many efforts have been made to assess the meteoroid hazard to space vehicles. The problem is two-fold. First, the natural environment must be defined in terms of flux or number density as a function of mass and velocity. Secondly, the damage to a given structure as a function of mass and velocity must be specified. With these two ingredients, the hazard to a particular space vehicle may be determined by integrating over the mass and velocity distributions to find the probability of encounter with a particle that will cause critical damage.

Early attempts to define the mass-flux distribution relied on visual observation of meteors and subjective estimates of their brightness compared to fixed stars. Later, photography provided a more precise method for obtaining magnitudes. However, photographic methods are limited to about first or second magnitudes. The problem of interpreting the observed brightness in terms of energy or mass remained. This was solved by assuming some luminous efficiency, or fraction of energy converted to light. Later experiments such as Trailblazer, which launched an artificial meteor of known mass and velocity into the atmosphere, provided a somewhat firmer basis for this interpretation.

Structural damage was estimated by extrapolating ballistic data at a few kilometers per second to meteoroid velocities — approximately a five-fold extrapolation.

The number of hazard models was almost equal to the number of investigators, since each had his own opinion of how to do the various interpretations and extrapolations, as may be seen in Figure 1. It was not until penetration experiments were flown

TABLE 1. ENERGETICS OF METEOROID ENCOUNTER

	11 km/sec	20 km/sec	72 km/sec
Available Energy (MJ/kg)	60	200	2500
(eV/amu)	0.6	2	25
Typical Pressures N/m ²	50 × 10 ⁹ to 30 × 10 ¹⁰ (0.5 to 3.0 Mb)	15 × 10 ¹⁰ to 75 × 10 ¹⁰ (1.5 to 7.5 Mb)	15 × 10 ¹¹ to 75 × 10 ¹¹ (15 to 75 Mb)
Temperature of Compressed Material (°K)	0.5 × 10 ⁵	1.5 × 10 ⁵	2 × 10 ⁶

FOR COMPARISON:

Yield of TNT is 1.75 MJ/kg

Typical metallic bond is 0.073 eV/amu (Fe)

Largest ionic bonding energy is 0.4 eV/amu (LiF)

Pressure at interior of earth is 4 × 10¹¹ N/m² (4.0 Mb)

Temperature at interior of sun is 15 × 10⁶°K

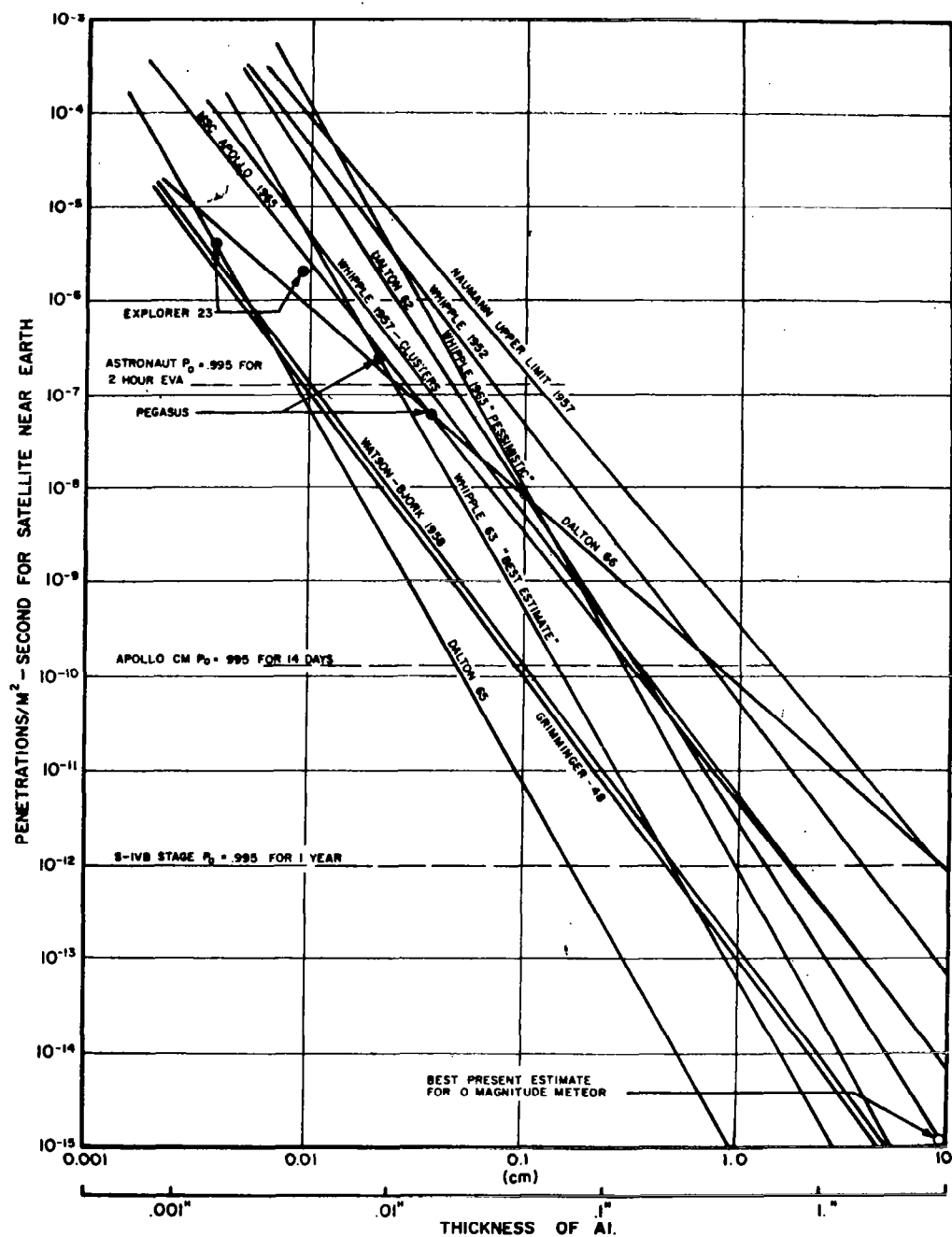


Figure 1. Summary of various proposed meteoroid environmental models.

on satellites that some coherent picture began to emerge. Through use of the more recent measurements and a more refined interpretation, the present picture of the meteoroid environment is illustrated in Figure 2.

Considerable improvements have been made in the development of hypervelocity techniques as well as in theoretical understanding of impact phenomena and of the behavior of matter at the pressures and temperatures associated with meteoroid impact.

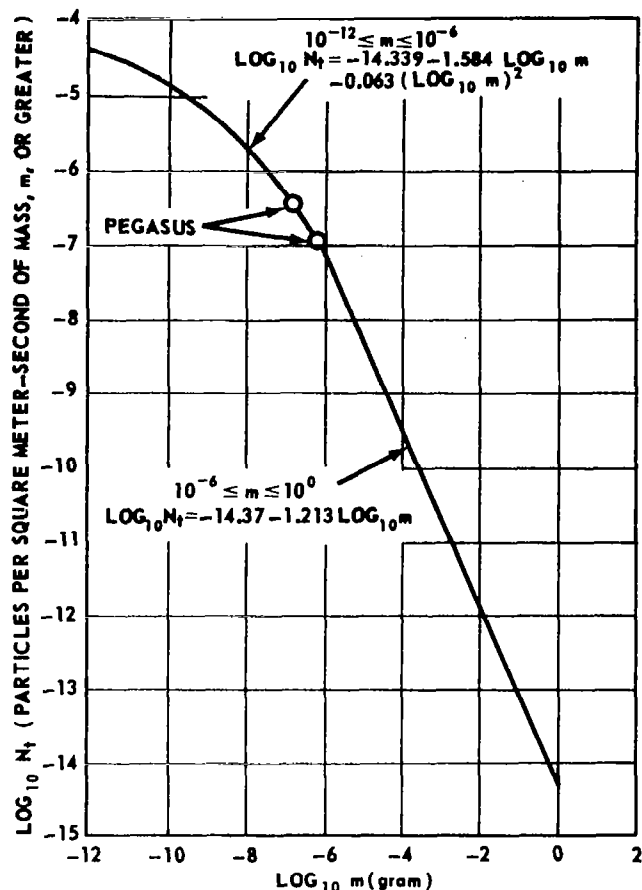


Figure 2. Current meteoroid environment.

MSFC has contributed heavily in the evolution of the present picture of the meteoroid environment as well as in experimental and theoretical work in accelerator development, impact mechanics and related phenomena, and high-pressure, solid-state

physics. It is the purpose of this review to report on some of the more recent accomplishments.

ACKNOWLEDGMENTS

The Astrophysics Branch of the Physics & Astrophysics Division, Space Sciences Laboratory (SSL) wishes to express its gratitude to various NASA Headquarters agencies, especially to OART for its support of the meteoroid program at Marshall Space Flight Center (MSFC). We particularly wish to thank Mr. Charles D'Aiutolo for his interest and encouragement in this program. Also we are deeply indebted to SSL personnel, particularly our Director, Mr. Gerhard B. Heller, and to our former Director, Dr. Ernst Stuhlinger, and to our former Division Chief, Dr. James B. Dozier, and his deputy, Mr. Ray V. Hembree, for their strong endorsement of this activity and for providing management support to these programs.

We wish to express our appreciation to the other MSFC Laboratories that supported this effort and in particular to Mr. Clyde Nevins, of S&E-ASTN-ES, who has cooperated with us extensively in developing design information.

We also wish to acknowledge the efforts of our technicians, Mr. Archie Miller, Mr. Huie James, and Mr. Sam Brown of Brown Engineering Company, and the efforts of Mr. Charles MacKay and Mr. Jim Harrison of S&E-SSL-P, our summer student, William Peters, and our co-op students, Mike Duggan, David Rannefeld, Jerry Washburn, William Langley, Jennifer Hornbuckle, Wanda Neely, and Dean Mitchell, all of whom spent many hours observing and analyzing data.

LIGHT GAS GUN EXPERIMENTS

By

David Jex

FACILITY DESCRIPTION

At present the Space Sciences Laboratory (SSL) is operating two light gas guns. The smaller gun has a nominal 0.1588-cm (0.0625-in.) launch tube, but is capable of launching projectiles up to 0.2381 cm (0.0938 in.) in diameter. Driven by a .375 H&H Magnum rifle cartridge, the gun has a velocity capability of 8.5 km/sec. The larger gun has a nominal launch tube diameter of 0.318 cm (0.125 in.) that can be extended to 0.635 cm (0.25 in.). A 20-mm aircraft cannon cartridge is used as a driver. Velocities approaching 10 km/sec have been achieved. A novel saboting technique allows glass beads as small as 100 μ as well as full bore projectiles to be launched.

Instrumentation for these ranges includes standard instrumentation such as image converter cameras, 100-MHz counters, photomultiplier tube velocity stations, etc. Also there are two field emission Febetron 600 keV pulsed electron guns available that can be used to produce betagrays, flash x-rays, or super-radiant light.

The primary intended uses of this range were to study physical phenomena associated with hypervelocity impact and to develop and calibrate meteoroid detectors. However, the high velocity capability and low operating cost of our range made it very much in demand for providing quick answers to actual design problems at MSFC and at other NASA installations.

EXPERIMENTS CONDUCTED

The light gas gun experiments conducted in the last two years can be grouped under three main headings.

1. Assistance in quick analysis of basic structures exposed to the meteoroid environment.
2. Examination and calibration of existing

meteoroid detectors and basic research for future applications in meteoroid detection analysis.

3. Basic research in understanding the process and characteristics of the impact phenomenon.

These three main headings together with those experiments that logically fall under each are shown in Table 1. The eight specific tests listed under these headings will be discussed in some detail in the following pages.

Assistance in Quick Analysis of Basic Structures Exposed to the Meteoroid Environment

VULNERABILITY OF SOLAR CELLS

At the request of the Astrionics Laboratory of MSFC, the vulnerability of solar cells to be used on the Apollo Telescope Mount was examined. The questions to be answered are: Will a panel of solar cells suffer a catastrophic failure when impacted by a meteoroid and what size meteoroid can the panel withstand and still not suffer catastrophic failure?

Figure 1 shows the results of an impact of a 0.318 cm (0.125 in.) diameter, 0.318 cm (0.125 in.) long cylindrical projectile with a density of 1.2 gm/cm³ at a velocity of 7.92 km/sec. By visually examining the extent of damage and measuring the voltage produced under the same conditions by the panel before and after impact, it was evident that only those cells directly impacted failed. There was no evidence of catastrophic failure such as propagations of cracks or delaminations. Since the projectile size used in this test represented an upper limit on what could be expected on a large solar cell array, it was concluded that large meteoroids did not present a severe hazard to solar cell arrays. Additional tests with smaller projectiles and at oblique impacts defined the expected failure rate of solar cell panels.

TABLE 1. AREAS OF INVOLVEMENT AND SPECIFIC EXPERIMENTS CONDUCTED

1. ASSISTANCE IN QUICK ANALYSIS OF BASIC STRUCTURES EXPOSED TO THE METEOROID ENVIRONMENT
 - a. Vulnerability of Solar Cells
 - b. Bumper Shield Effectiveness
 - c. Protective Characteristics of Honeycomb Material
 - d. Evaluation of Meteoroid Shield on Mariner 71
(Jet Propulsion Laboratory)
 - e. Check on Soft X-ray Device (Naval Research Laboratory)
2. EXAMINATION AND CALIBRATION OF EXISTING METEOROID DETECTORS AND BASIC RESEARCH FOR FUTURE APPLICATION IN METEOROID DETECTION ANALYSIS
 - a. Calibration of Pegasus Panels
 - b. Electromagnetic Pulse Associated With Shocked Dielectrics
3. BASIC RESEARCH IN UNDERSTANDING THE PROCESS AND CHARACTERISTICS OF THE IMPACT PHENOMENON
 - a. Research of Impact Phenomenon (Contract With IIT Research Institute)



Figure 1. Simulated meteoroid impact on solar cell panel.

BUMPER SHIELD EFFECTIVENESS

When it was determined that additional meteoroid protection was needed for the Orbital Workshop, it was proposed to deploy a thin shield or meteoroid bumper around the cylindrical S-IVB tank. To determine the effectiveness of this bumper, it was necessary to determine what size projectile could perforate this shield and remain relatively intact. Empirical data to answer this question were generated in a test series in cooperation with the Astronautics Laboratory, MSFC. The approach taken by this lab was to fix the spacing between the bumper or shield and the secondary surface representing the actual spacecraft surface. Then, by varying the projectile size and bumper thickness, find some relations that could aid in extrapolating to the expected meteoroid impact condition.

Figure 2 shows the actual impact process as viewed by the TRW image converter camera. The profile of the debris cloud can be seen. Figure 3 is a photograph of one of the specimens used. The damage pattern is typical of the results using this cylindrical type projectile. This particular projectile impacted at an angle as may be seen by the oblong hole in the bumper. This also produced the peculiar spray pattern on the rear surface. Projectiles

impacting end-on produced the conventional circular spray pattern. In either case, the depth of penetration into the rear surface is essentially the same. Figure 4 is a graph of the results. It will be noted that the depth of damage in the secondary surface remains constant for each size projectile until it reaches a point where the bumper is no longer sufficient to completely break up the projectile. At this point, there is a noticeable increase in the depth of the damage. The minimum bumper is the thinnest shield necessary to completely fragment the projectile. Any thicker bumper will give adequate protection as far as depth of penetration is concerned. Figure 5 is a comparison of the normalized data that were obtained with lexan on aluminum compared with similar work with aluminum on aluminum by C. J. Maiden at General Motors Defense Research Laboratory. From the figure, it is evident that the bumper is more effective against the lower density lexan ($\rho = 1.2 \text{ gm/cm}^3$) than against aluminum with $\rho = 2.77 \text{ gm/cm}^3$. This effect could be very significant since the bulk density of meteoroids is believed to be less than 1.0 gm/cm^3 .

Additional information on this test series was presented at the OART Meteoroid Impact and Penetration Workshop October 8-9, 1968, at the Manned Spacecraft Center.



Figure 2. Simulated meteoroid impact of bumper shield configuration.

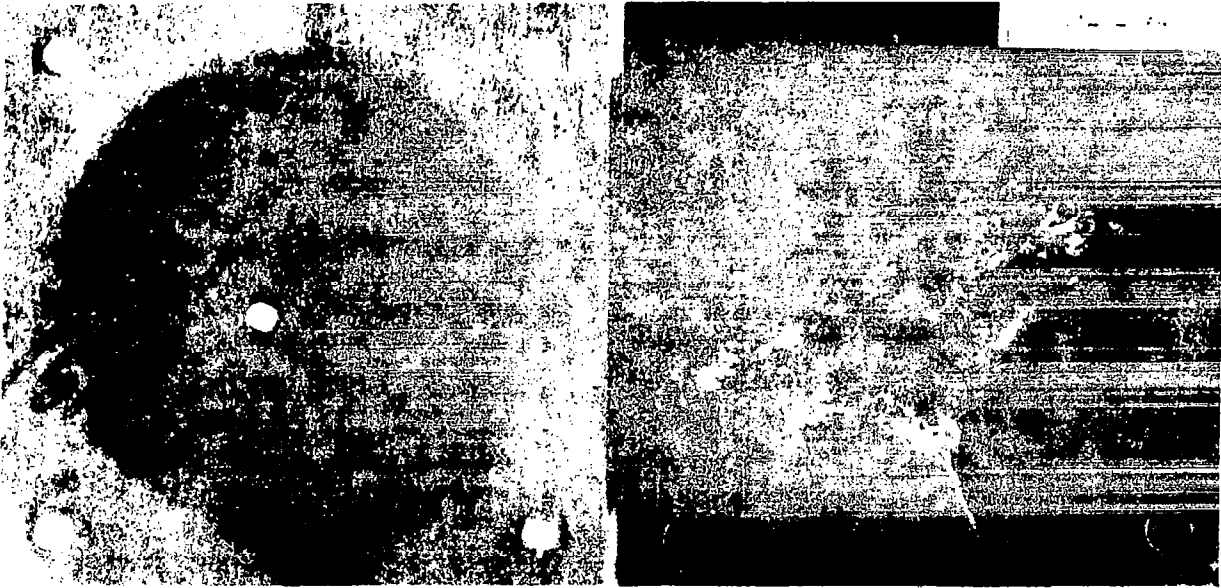


Figure 3. Bumper shield and secondary surface damage.

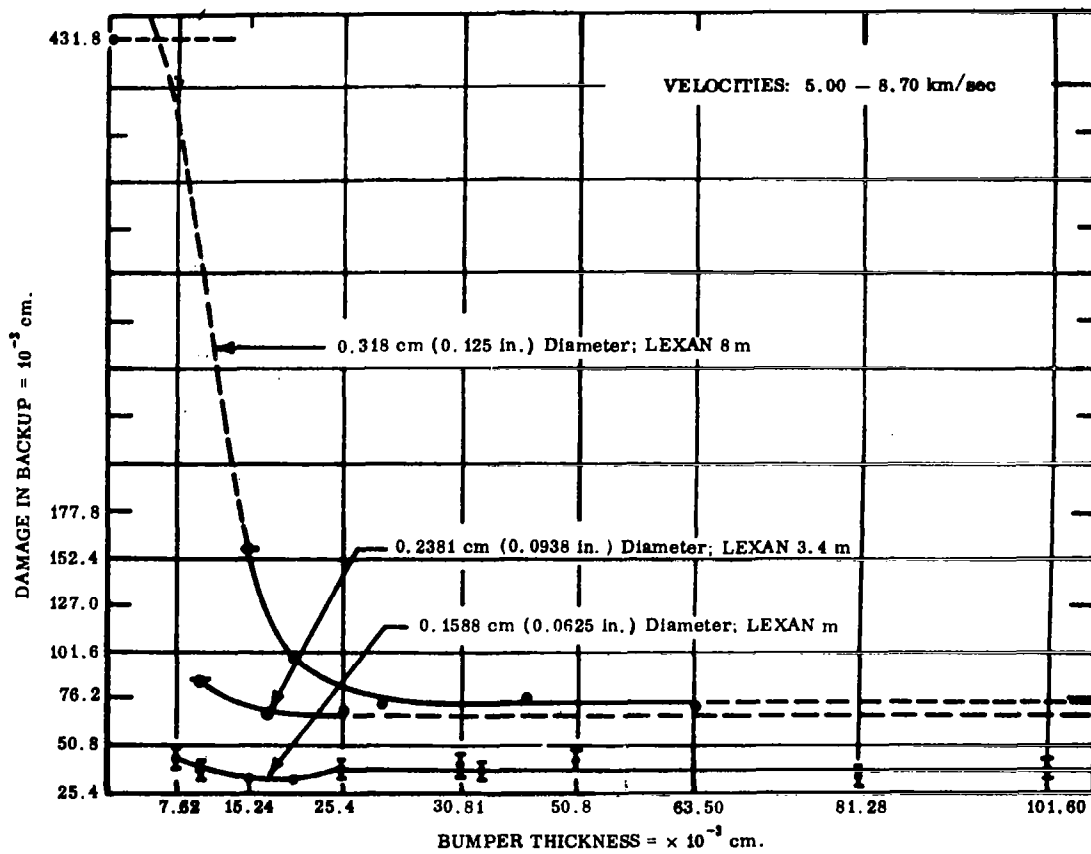


Figure 4. Results of bumper shield test series.

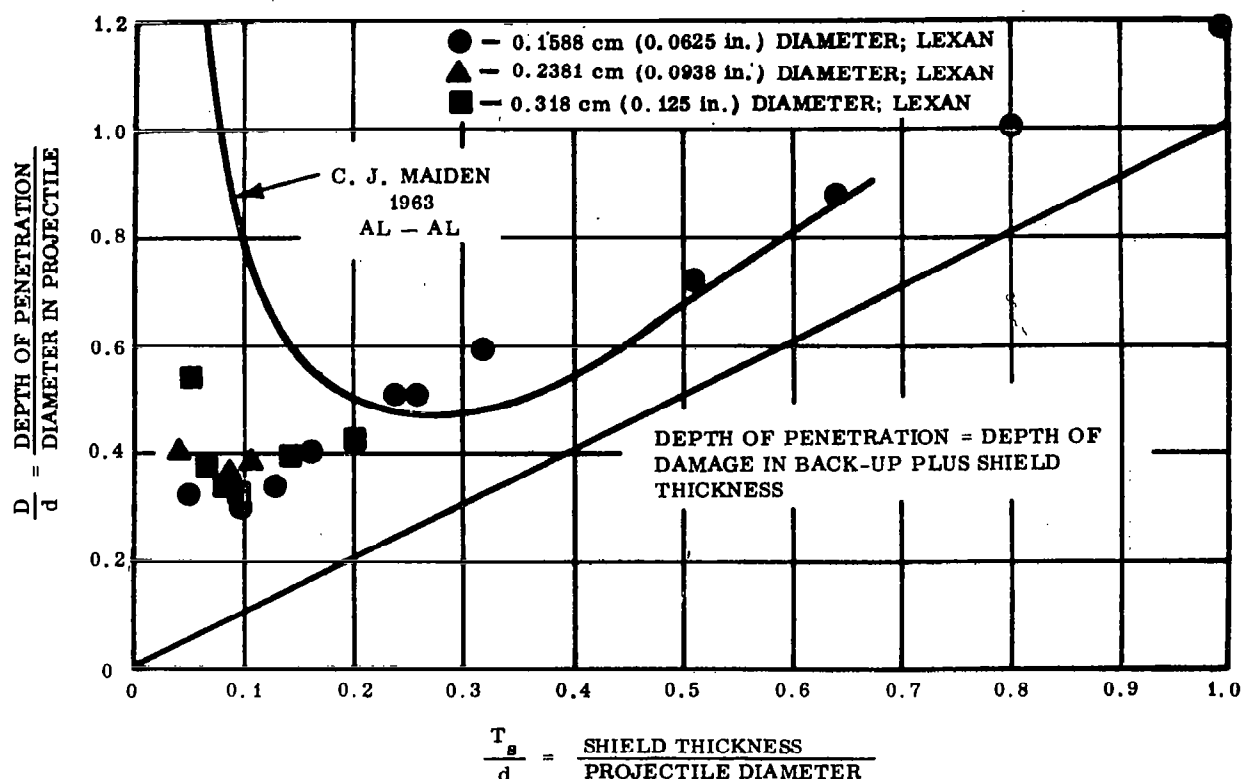


Figure 5. Comparison of normalized results of the bumper shield test series with a similar independent study.

PROTECTIVE CHARACTERISTICS OF HONEYCOMB MATERIAL

Honeycomb material offers attractive advantages as a structural material because of its high rigidity-to-weight ratio. Also, the outer wall naturally serves as a meteoroid bumper, which should improve its protection capability over an equivalent weight single wall. The question arose as to whether the channeling action of the honeycomb structure might offset some of the gain afforded by the double wall. A series of tests was conducted to evaluate this question.

The tests were conducted by holding projectile mass constant and varying velocity until failure of the rear surface was achieved. Figure 6 illustrates the results of these tests. The cutoff point near 80 degrees was estimated from impacts at 75 degrees to the normal. Figure 7 shows the area of failure in relation to the point and angle of impact. It will be noted here that the failure area is within the perimeters of the cell of initial impact, although as

indicated by the dashed lines, the cell walls were destroyed in most cases. This shows that the honeycomb directs, or channels, most of the debris resulting from the primary impact at a point.

Tests on equivalent double-wall structures have not been completed at this time and will be published in a forthcoming report.

EVALUATION OF METEOROID SHIELD ON MARINER 71 AND CHECK ON SOFT X-RAY DEVICES

Because of the capability to launch very small glass beads at high velocities, MSFC was asked by several outside agencies to assist in meteoroid testing of space vehicles and experiments. A series of shots was conducted at the request of the Jet Propulsion Laboratory to evaluate the meteoroid shield effectiveness of the insulation on Mariner 71. Tests were also conducted on a soft x-ray experiment under development by the Naval Research Laboratory.

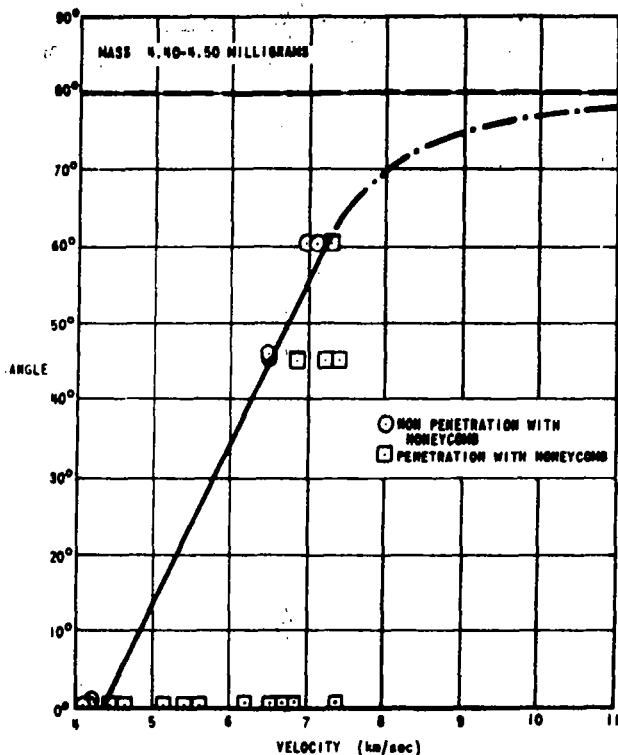


Figure 6. Results of honeycomb material test series.

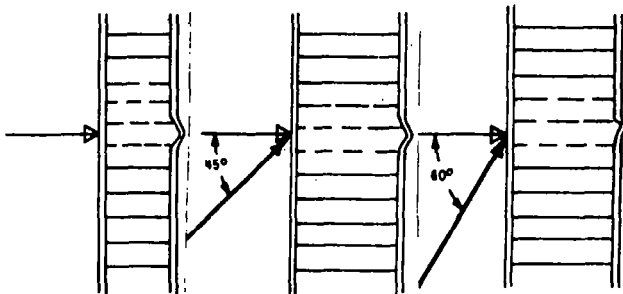


Figure 7. Relation of failure area to impact point for honeycomb material test series.

Examination and Calibration of Existing Meteoroid Detectors and Basic Research for Future Applications in Meteoroid Detection Analysis

CALIBRATION OF PEGASUS PANELS

The Pegasus spacecraft carried the first large area meteoroid detectors into space. The area

of surveillance afforded by these spacecraft allowed a sampling of the meteoroid population in the size range from which significant structural damage can be expected. These data points form the basis for extrapolation of the meteoroid environment to the larger masses that are of critical interest to large manned vehicles. Since these are the only data concerning this size range that are expected to be available in the foreseeable future, a substantial effort was made to calibrate the detector.

Figure 8 shows the results for the 0.04-cm Pegasus panel. Each vertical line represents a mass. The hash marks on the right side of the line represent detected impacts, while the hash marks on the left side of each line represent undetected impacts. In this manner, the threshold velocity may be established for a number of masses. Extrapolation of these points to average meteoroid velocity gives the average threshold mass for the detector. It may be seen that the higher velocities attainable by the SSL facility extended the calibration data to substantially smaller masses and thereby increased the confidence in the extrapolation. Also it is interesting to compare these results with the predicted results using the empirical penetration formula developed by Richard Fish at Ames Research Center. It may be seen that there is even a greater velocity dependence than that predicted by Fish.

Figure 9 shows some of the output waveforms from the Pegasus detector. The photographs are those taken of the oscilloscope that monitored the panel discharge. The photographs illustrate the difference in penetration and nonpenetration. The typical sharp quick discharges on the left are those associated with penetration. The relatively long discharges or no discharges displayed on the right are associated with nonpenetration firings. The interesting fact is that a sharp deep discharge is obtained when the impact is substantially above threshold. However, when near threshold conditions prevail, the discharge becomes more gradual and more shallow until it is no longer detectable.

ELECTROMAGNETIC PULSE ASSOCIATED WITH SHOCKED DIELECTRICS

Several interesting phenomena associated with impacts on dielectrics have been observed recently in the form of electromagnetic disturbances. An insulated copper plate was installed behind a dielectric sheet. A shielded box surrounding the plate served as ground reference as shown in Figure 10. A nonpenetrating impact on the dielectric produces a short positive pulse followed by a long negative deflection, as shown in Figure 11. The top

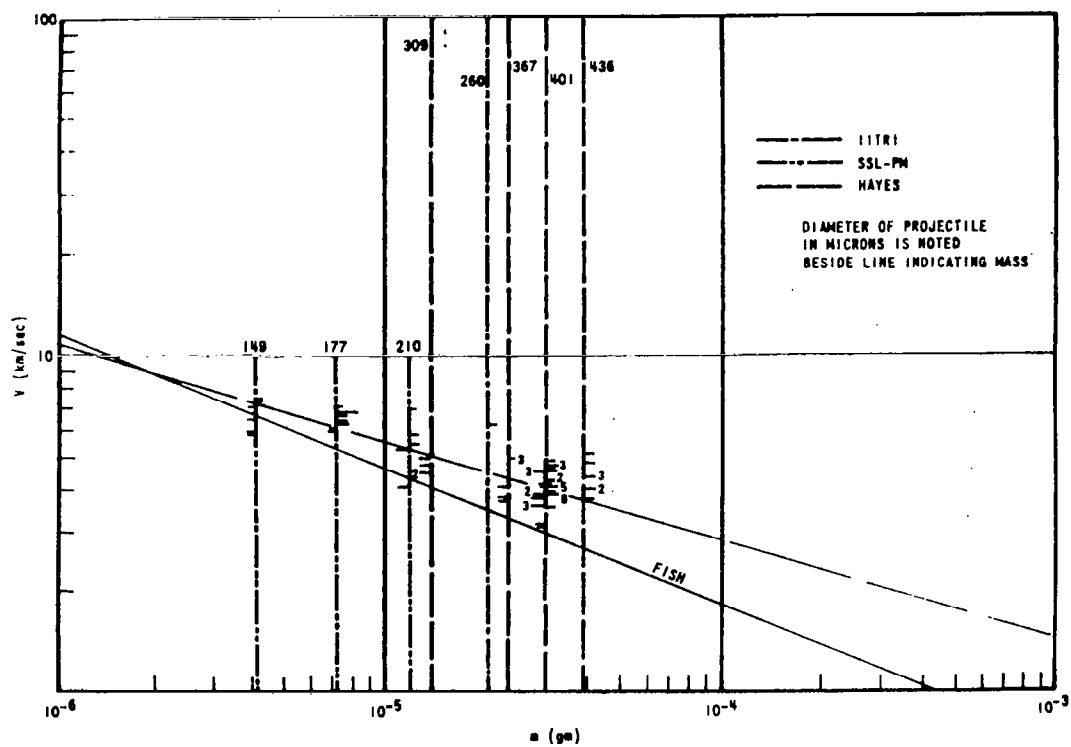


Figure 8. Results of calibration tests on Pegasus panels.

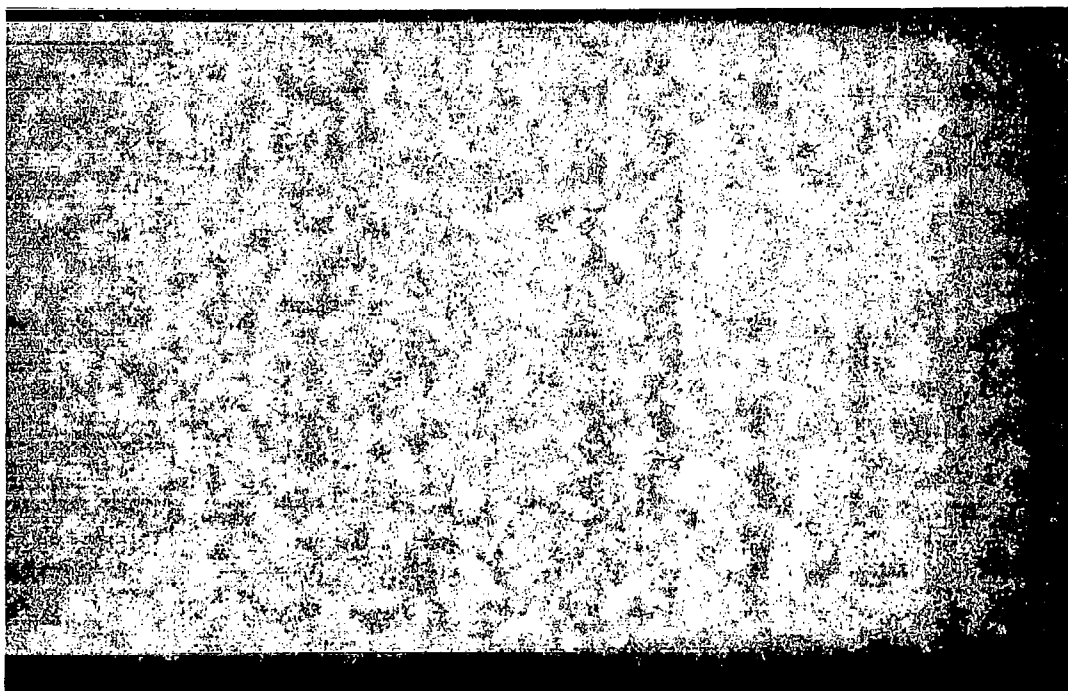


Figure 9. Output waveform profiles of Pegasus panels.

NOT REPRODUCIBLE

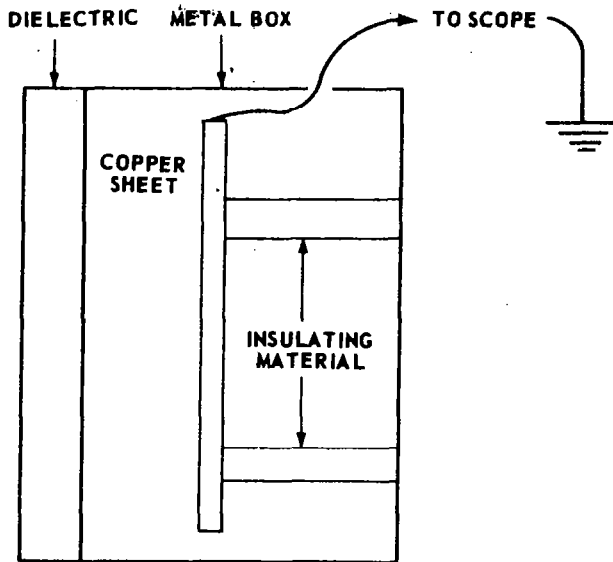


Figure 10. Target configuration for dielectric study.

profile is at 10 V/cm and the bottom profile is at 0.05 V/cm. The time base is the same for both. This long term negative deflection is obviously a result of a charge on the dielectric sheet that may

have been deposited by the projectile, or may have resulted from charge ejection during the impact. The origin of the fast positive spike is not so apparent. Additional tests will be performed to investigate this phenomenon and to determine its potential as a meteoroid impact detector.

Basic Research in Understanding the Process and Characteristics of the Impact Phenomena

RESEARCH ON IMPACT PHENOMENA

To make certain that the basic phenomena associated with hypervelocity impact are understood, an experimental program has been conducted to make basic measurements on the debris cloud that can be compared with computed values. This program has concentrated primarily on the penetration products emerging from a thin sheet when impacted by a flat disk. This configuration was chosen to minimize jetting effects. Also the penetration products at the rear of a thin shield are of considerable importance in analyzing bumper performance.

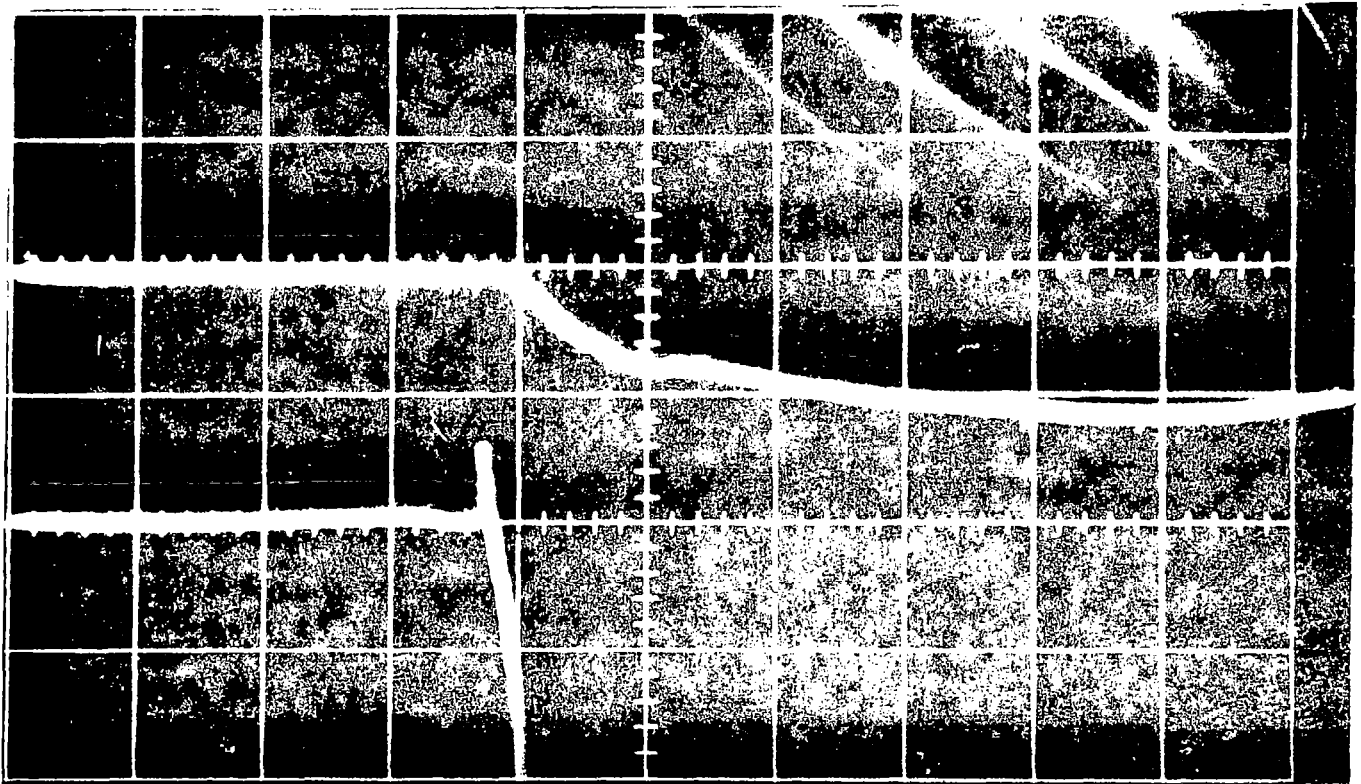


Figure 11. Electromagnetic disturbance waveform associated with dielectric study.

Most of the experimental work was carried out under contract NAS8-20337 at the Illinois Institute of Technology Research Institute by Jerome Jeslis. Measurements include velocity and density distributions in the debris cloud, temperature estimates based on photometry and spectral data, time

resolved spectra, and ionization state. All measurements were done at less than $13.3 \times 10^{-4} \text{ N/m}^2$ (10^{-5} torr) to minimize the effect of collision with ambient atmosphere molecules. The measurements are almost completed and will be published in a contractor report.

1 N70-35507

SIMULATED MÈTÈORÖID IMPACT TESTING ON MDA CONFIGURATION

By

R. C. Ruff

SUMMARY

The results of research programs to improve the experimental capabilities of the Materials Division Meteoroid Simulation Facility of the Astronautics Laboratory are presented herein. The results of penetration threshold measurements on various configurations of the Multiple Docking Adapter (MDA) such as the spacecraft wall, external electrical cable tunnel, and photographic window bumper are discussed. Also given are results of penetration tests on various densities of multilayer insulation materials. The current research efforts are described.

INTRODUCTION

The programs that are presented in this paper were carried out in the Materials Division Meteoroid Simulation Facility of the Astronautics Laboratory. The programs had a dual purpose. One was to give basic data for design purposes and structural analysis. The second was to arrange the tests so that a good understanding of the physics of hypervelocity impact could be acquired.

The following topics will be presented; (1) a brief summary will be presented of the research on hypervelocity launch techniques that were necessary to provide the experimental capabilities needed for penetration testing, (2) some of the results of the MDA configuration tests will be presented, (3) the results of a series of low density multilayer insulation tests will be related to protection efficiency, and (4) some current research studies will be briefly described.

HYPERVELOCITY LAUNCH TECHNIQUES

The Materials Division Meteoroid Simulation Facility is shown in Figure 1. The facility consists

of a two-stage light gas gun with a 1.27 cm (0.5 in.) diameter launch tube. The breech of the light gas gun is on the left with the pump tube, high pressure section, and launch tube extending to the right. At the far right is the dump tank for dispersing the acceleration gases, the x-ray diagnostics section for velocity and integrity determinations, and the target tank.

This light gas gun facility was developed for the Materials Division under a research contract with the intent of providing an inherent flexibility in testing procedures. The success of this endeavor is the fact that projectiles with a mass range from 0.008 to 5.0 grams can be launched at velocities from 5 to 8 km/sec. This facility was delivered approximately 2 years ago. After the first operational checkout firings, it was felt that there were two areas associated with the launch techniques in which improvements would greatly increase the information output of the facility.

The first problem area was in the design of the sabot stripper that was being used. The sabot technique is a method of launching projectiles of various sizes and shapes. The projectile of interest is placed on the front face of a full bore, polycarbonate slug called the sabot. The sabot and projectile must then be separated after leaving the muzzle of the light gas gun. This separating or stripping operation can be described using the schematic diagram of the range tank shown in Figure 2. The projectile and sabot (not shown) are launched from the barrel of the light gas gun shown on the left. As they leave the barrel, the sabot impacts four tungsten stripper pins, while the projectile, being less than full bore, goes between the pins and straight down range through a hole in the sabot trap and onto the target. The impact between the sabot and the stripper pins is a hypervelocity impact and, therefore, completely demolishes both the sabot and the pins. The debris from this impact is then caught on the sabot trap.

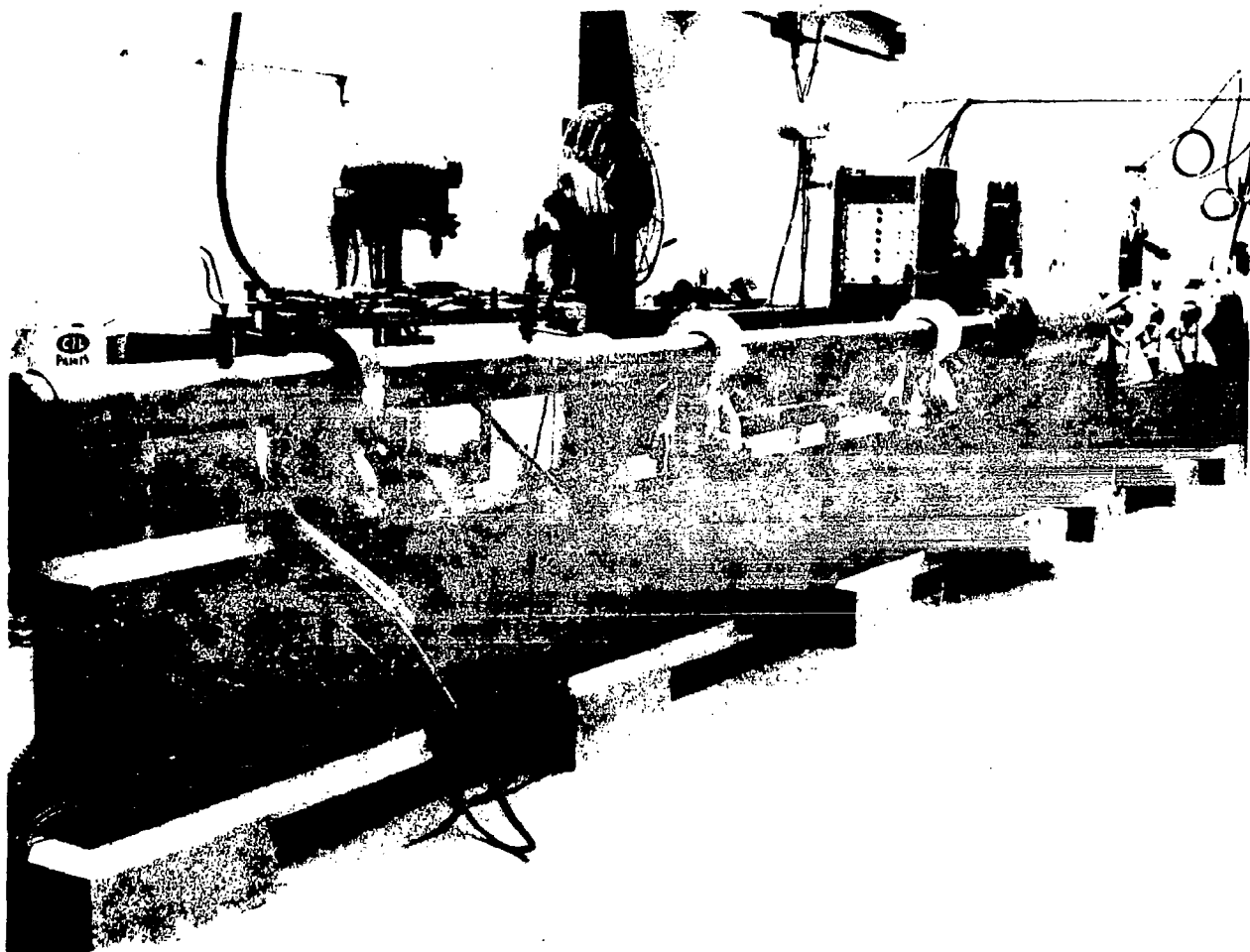


Figure 1. Materials Division Meteoroid Simulation Facility.

It was noticed that with the original design of the stripper pins some debris was getting through the hole in the sabot trap and also impacting the target. Although in most cases the debris damage could be separated from the projectile damage, there were several cases where the results were ambiguous and the test had to be repeated. To avoid this repetition, a short research effort was launched to try to understand the physics of shock-wave focusing and momentum transfer in this type of hypervelocity impact. The parameters available for studying changes in stripper design were the debris pattern on the sabot trap and the physical condition of the projectile.

This research effort resulted in a new stripper design shown in Figure 3. It was found that the front face of the tungsten pins had to be machined with

approximately a 15-degree angle. Too large an angle focussed the shock wave to such a degree that the projectile was caught and damaged. Too small an angle meant that there was not sufficient radial momentum transfer, and some of the dense tungsten debris would go straight down range through the trap and impact the target. It was also found that the leading face of the sabot had to have a bevel that matched that of the stripper pins. If the face of the sabot is left flat, then the impact angle between the pins and the sabots creates a high velocity jet of material that is forced inward and is sufficient to damage the projectile or actually force it off axis so that it will hit the edge of the sabot trap.

The evidence of the success of this new design is that in the last 120 shots there has not been a single failure because of the stripper operation. A

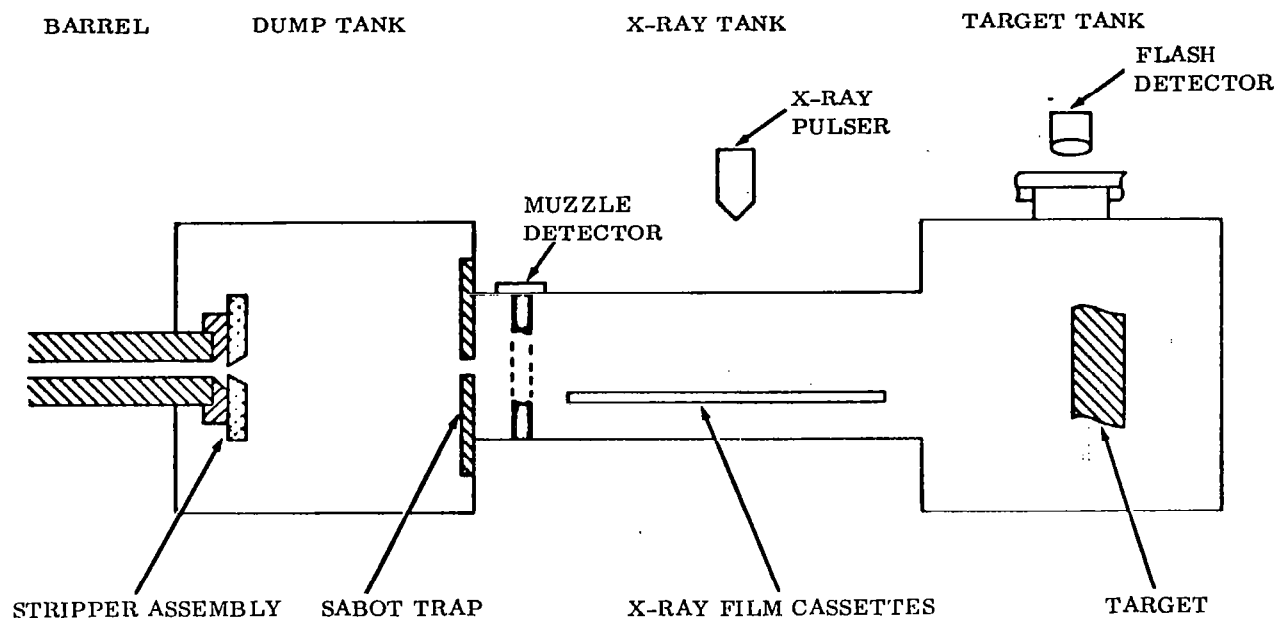


Figure 2. Schematic diagram of range tank.

negligible amount of debris gets through the trap and the projectile always impacts within 1.27 cm (0.5 in.) of the center of the target.

The second problem area was in velocity prediction. It was found that the velocity of the projectile could not be controlled to an accuracy of better than 8 or 10 percent. This is a common problem in many facilities. The standard solution is to take a statistical distribution of velocities to cover the range of interest. It was felt that there could be a considerable savings in money and especially time in making penetration threshold determinations if the velocity could be predicted more accurately.

For these reasons, a program was instituted to measure the variables in the first stage of the light gas gun such as the breech pressure, propellant burning time, and piston velocity. After analyzing these measurements, several changes in the loading and firing procedures were instituted. The velocity uncertainty is now down to ± 1 percent, which is essentially the accuracy of our velocity measuring instrumentation.

After these two design improvements were instituted, it was felt that the facility was ready to begin penetration threshold testing. The facility was ready to launch projectiles of controlled mass and velocity with negligible debris or velocity uncertainty. This

meant that the penetration threshold for an unknown configuration could be zeroed in on rapidly and accurately.

PENETRATION TESTS

MDA Wall Configuration

The MDA wall configuration was tested to determine its penetration threshold. The basic configuration is shown in Figure 4. This specific configuration consists of a 0.0508 cm (0.020 in.) thick 2014-T6 aluminum bumper on the left, a 5.08-cm (2.0-in.) void, a 2.54 cm (1.0 in.) thick section of high performance multilayer insulation, and a 0.196 cm (0.077 in.) thick 2014-T6 aluminum back-up plate that simulates the MDA pressure wall. The multilayer insulation consists of many layers of 0.25 mil doubly aluminized Mylar with red polyurethane foam spacer material.

This basic configuration was tested to determine its penetration threshold as a function of mass and velocity. The results are shown in Figure 5 where the log of the mass is plotted versus the log of the velocity. The test points where no penetration occurred are shown in the filled circles, while penetration

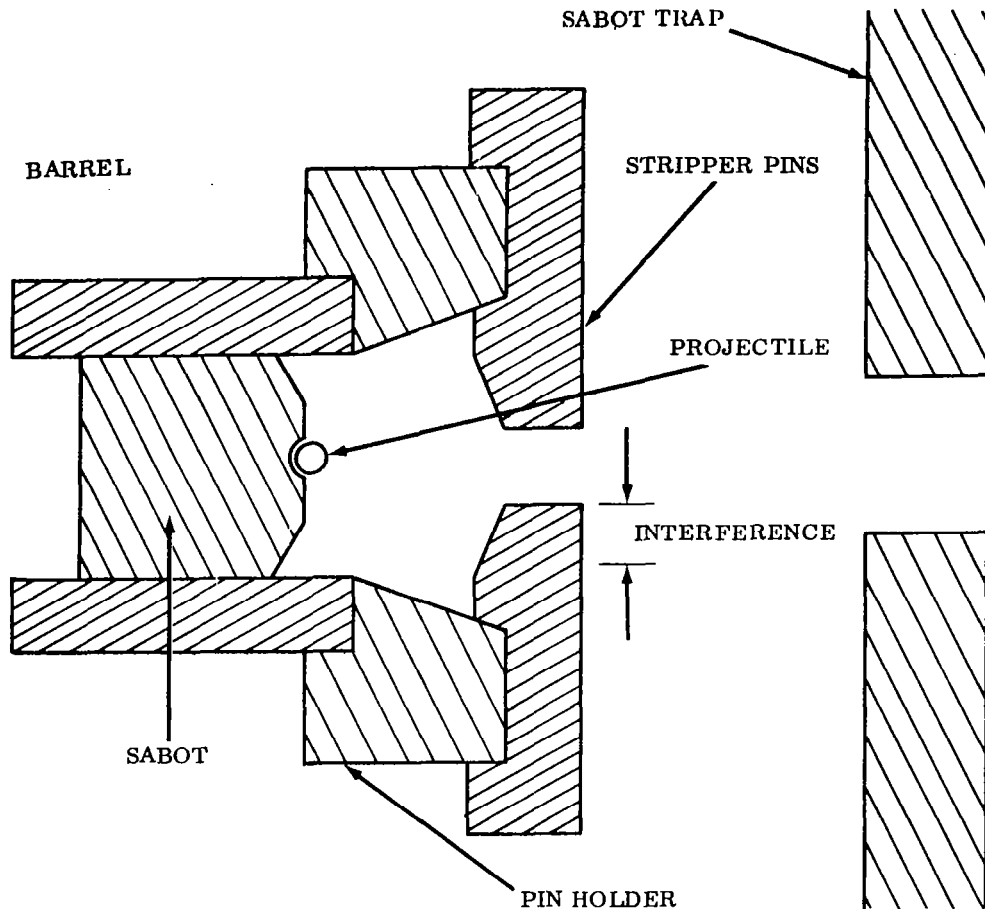


Figure 3. Schematic diagram of improved sabot stripper.

points are shown with open circles. The solid line shows the maximum slope that the penetration threshold curve could have over this velocity range. This is compared to the dashed line which is the Fish curve [1], a penetration curve for a single sheet of aluminum.

Comparison between the two curves shows that the experimental configuration is much more efficient at defeating higher velocity projectiles than is a single sheet of aluminum. Another way of comparison would be to extrapolate both curves to meteoroid velocities. One then would find that the experimental curve gives a much better safety factor than the Fish curve.

Unfortunately, without an experimental method of reaching at least 12 km/sec, the extrapolation of the experimental curve is presently unjustified. Therefore, structural design engineers must use the Fish curve extrapolation to calculate the penetration resistance at meteoroid velocities. Using this calculation, it turns out that the basic configuration is equivalent to approximately 1.27 cm (0.5 in.) of single sheet aluminum.

Penetration threshold determinations were made on several configurations that were variations of the basic configuration. The results from two variations are shown in Figure 6. The first variation was to

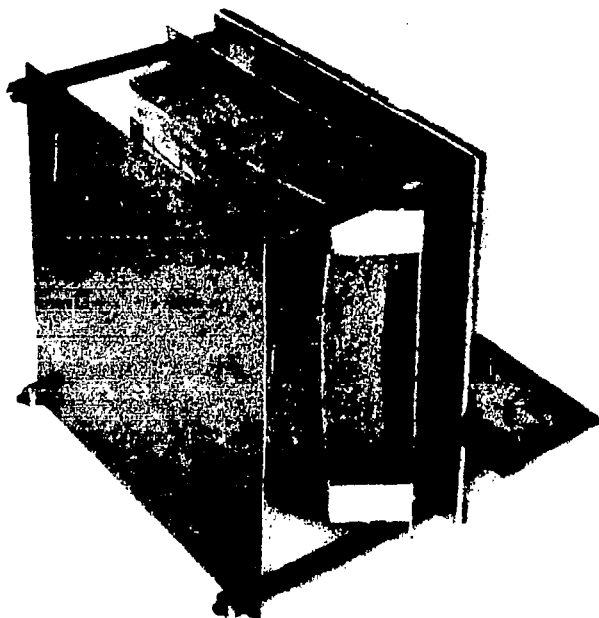


Figure 4. Target configuration for MDA wall penetration tests.

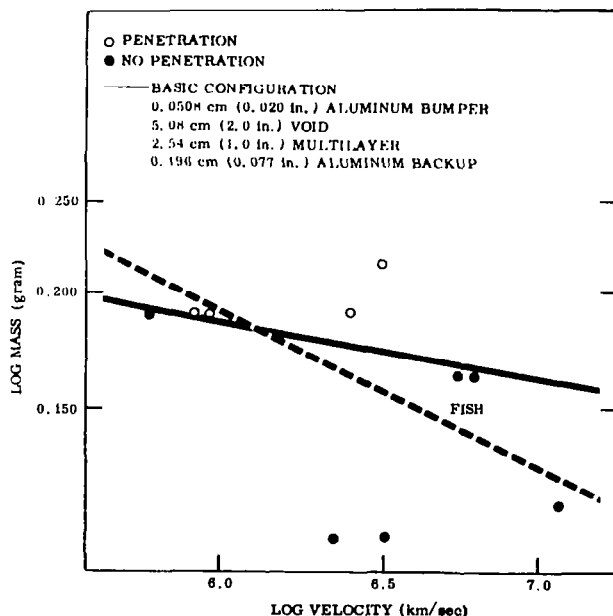


Figure 5. Impact test on MDA Series 1.

replace the 0.0508-cm (0.020-in.) aluminum bumper with an equal mass 0.0813-cm (0.032-in.) magnesium bumper. These results are the open penetration triangle and the closed, no-penetration triangles.

These points again delineate a line of maximum slope. This is the dashed line slightly above the solid line which is the curve for the basic penetration from Figure 5. Therefore, it is seen that the magnesium bumper is more effective in defeating a hypervelocity projectile than an equal mass but more dense aluminum bumper.

The second variation shown in Figure 6 is the removal of the insulation from the basic configuration. Another dashed line showing the maximum slope is drawn through the square data points. It can be seen that without insulation the configuration is penetrated by a projectile of half the mass of that which is needed to penetrate the basic configuration with insulation. This curve, therefore, shows the great effectiveness an external multilayer insulation has in increasing penetration resistance. Also, it should be noted that the curve without insulation is essentially parallel to that with insulation.

Test results on other variations of the basic MDA configuration are shown in Figure 7. These tests were made on targets with 0.635 cm (0.250 in.) thick backup plates instead of the basic 0.196-cm (0.077-in.) plate. This configuration is also planned for use on specific parts of the MDA. These tests were also made with insulation (circles) and without insulation (squares). Tests on the targets with insulation provided a penetration threshold point. However, the four data points were not sufficient to provide a threshold curve of maximum slope. The data point for targets without insulation did give a maximum slope.

The results shown in Figure 7 can be analyzed by comparison to the solid line, which is the curve for the basic configuration from Figure 5, and to the Fish curve for single sheet. Indications are that for such thick backup plates the threshold curves are more nearly parallel to the Fish curve. This is reasonable when it is noted that a 0.30-gram projectile is approximately 0.635 cm (0.250 in.) in diameter. Therefore, the bumper thickness to projectile diameter ratio is less than 1:10. This is much less than the optimum range for efficient projectile breakup. This means that this configuration may act very much like a single sheet since the bumper does not contribute much protection. One further observation is that the

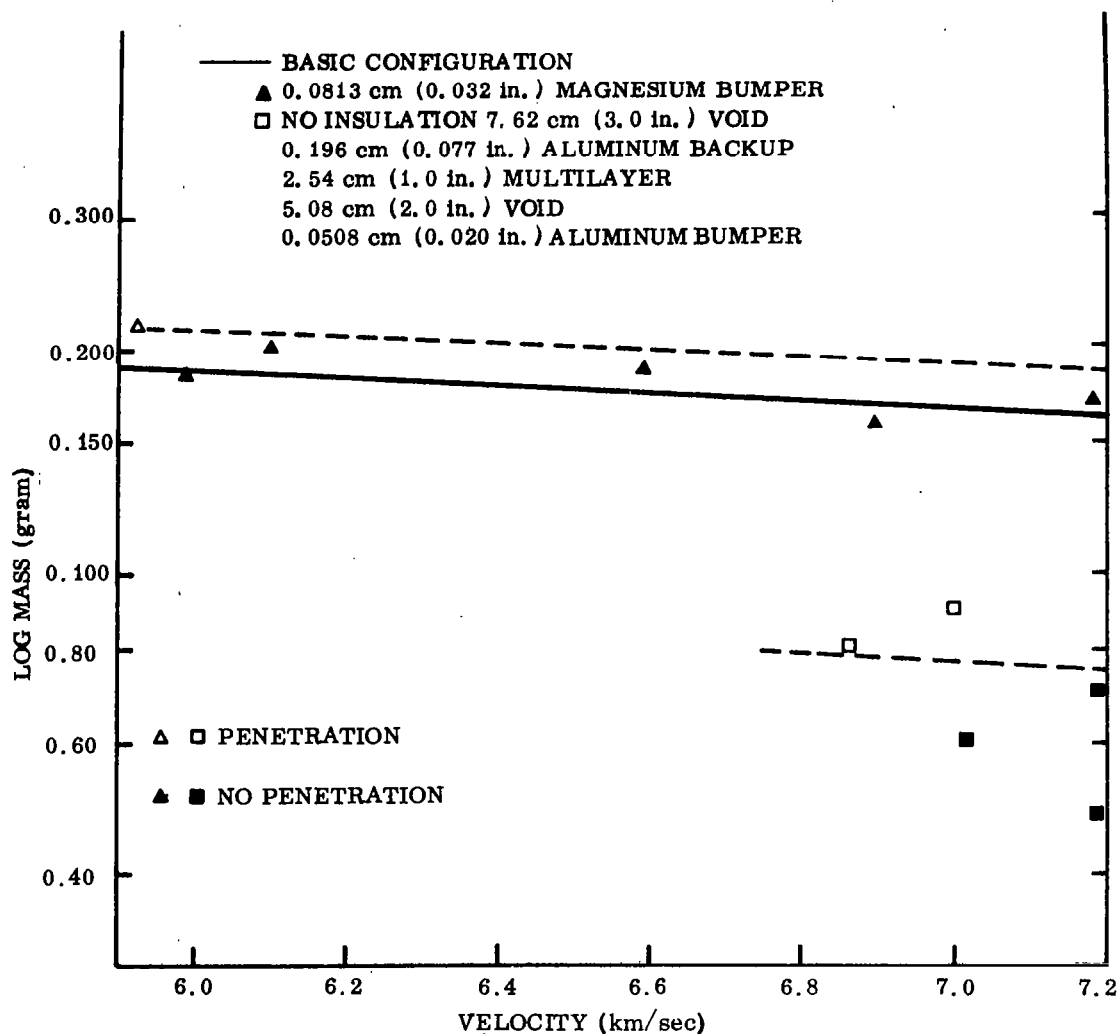


Figure 6. Basic MDA configuration compared both to magnesium bumper and to no insulation.

addition of insulation to the configuration does not double the mass protection as it did at lower masses.

As further evidence of the effectiveness of the multilayer insulation, it is interesting to compare the damage mechanism in a target without the insulation to one with insulation. Figure 8 shows the damage on a backup plate without insulation. The damage is a result of discrete particles coming off the bumper. Each particle is capable of cratering the backup plate, and where there is a sufficient density of particles, they actually knock holes through the backup plate.

Figure 9 shows a target in which insulation was used. Approximately the same projectile and bumper were used as in Figure 8; however, total damage comparisons should not be made because different backup plate thicknesses were used. In Figure 9 it can be seen that there is no longer any particulate type damage. What has happened is that the insulation completely vaporized the small particles that were formed by the bumper impact. Therefore, the damage with insulation is a result of a rapid, high pressure vapor pulse that deformed the plate beyond its elastic limit and actually ruptured the backup plate along radial lines.

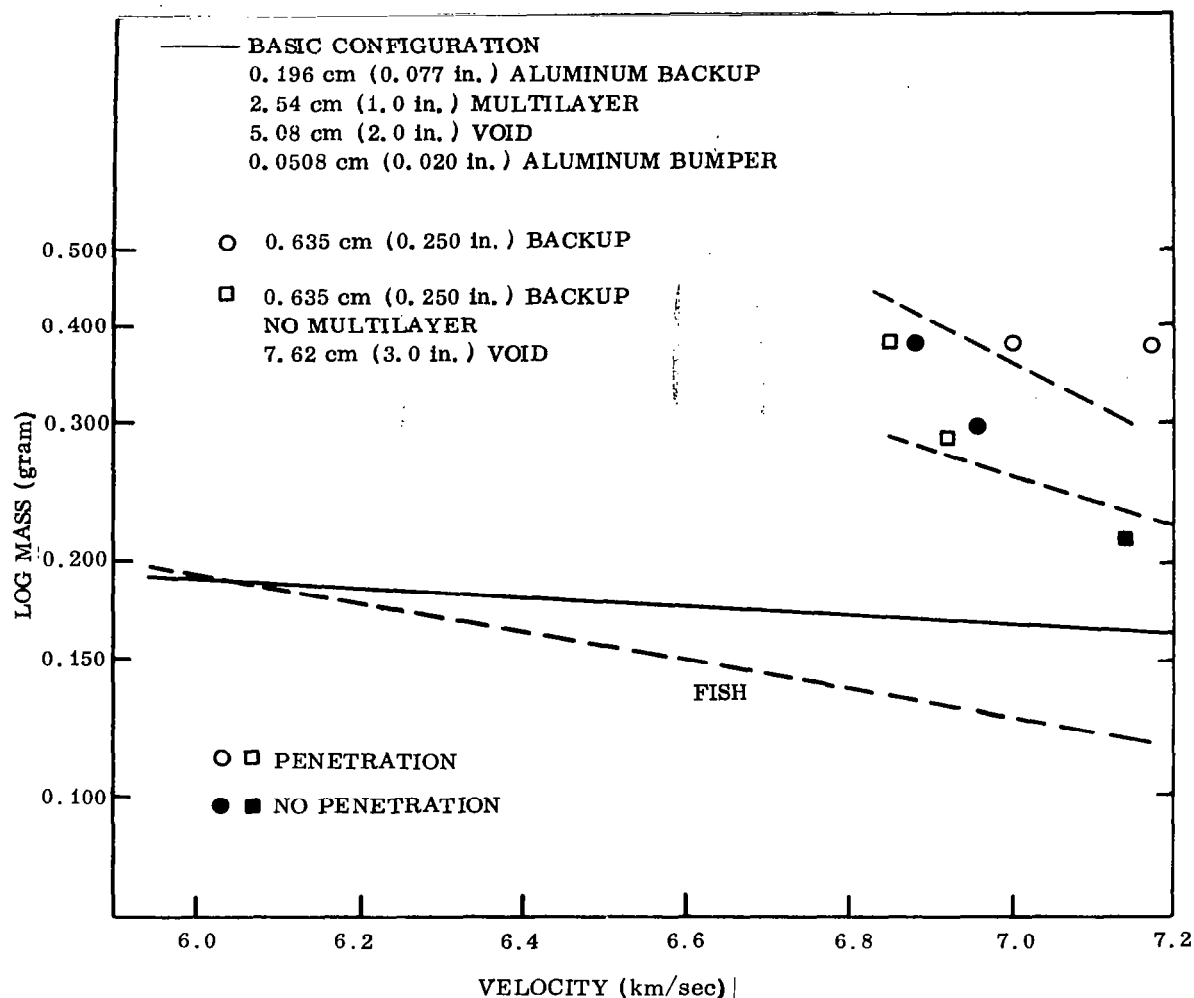


Figure 7. Basic MDA configuration compared to 0.635-cm (0.250-in.) backup.

MDA Electrical Cable Tunnel

Penetration tests were also made on the MDA external electrical cable tunnel. As the name implies, external cable on the MDA may also need to be protected against meteoroid damage. Several possible protection configurations were tested, but only the damage mechanism will be presented here.

Figure 10 shows the test fixture used for these tests. The target consists of a 0.102-cm (0.040-in.) aluminum bumper that shields four bundles of electrical cable. Figure 11 shows the damage that is done to the cable during a simulated meteoroid

impact. It can be seen that the debris from the bumper was in particulate form, as evidenced by the specific cratering on the backup plate. This particulate matter also impacted on the electrical cable and vaporized much of the electrical insulation. However, there was very little actual damage to the cables themselves. Also, after the impact it was seen that none of the stripped cables was physically touching. A possible reason for this is that when the debris impacted the wires, the gas pressure generated by the vaporization of the electrical insulations was sufficient to force the cables apart.

Although there is no physical contact between cables, there are still transient effects that need to

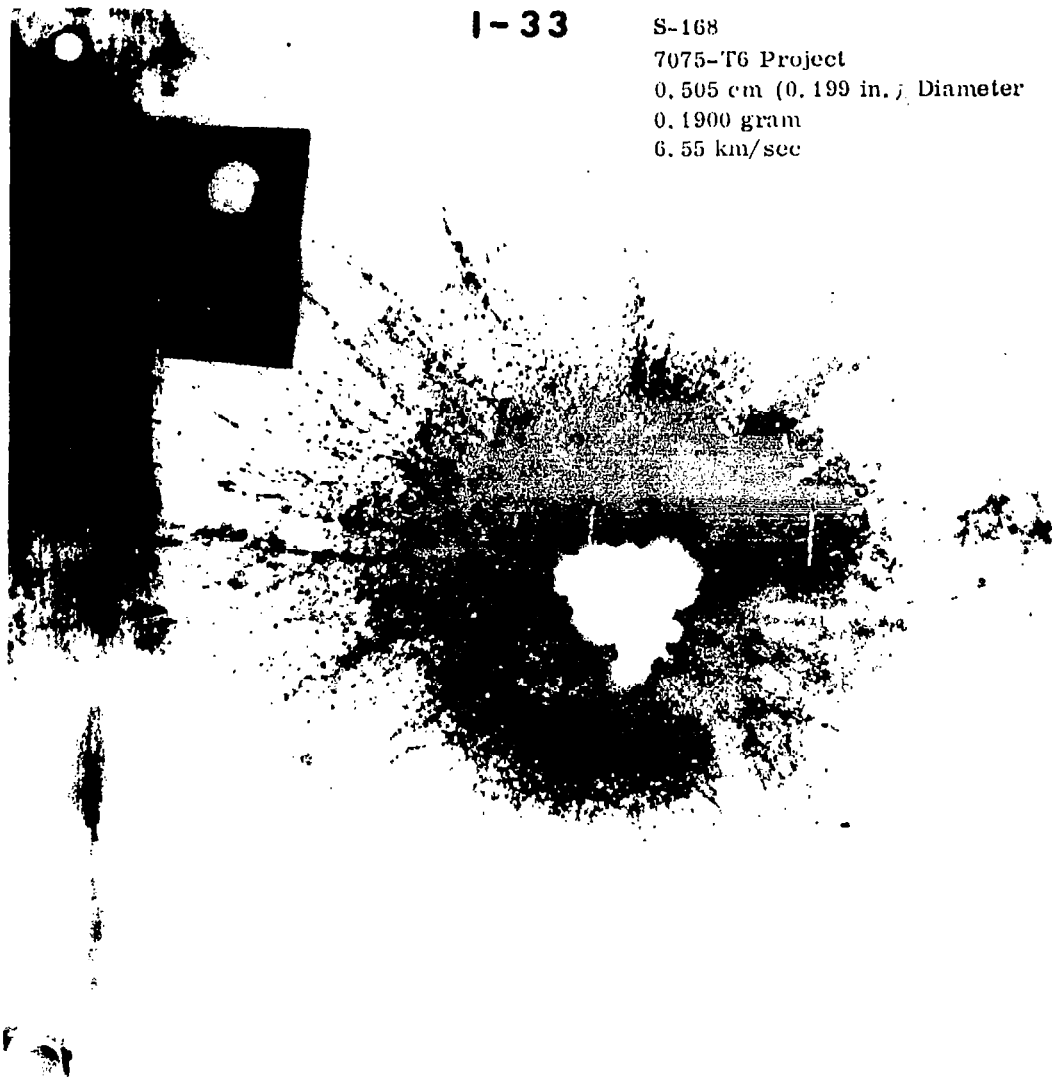


Figure 8. Example of damage when no insulation was used.

be considered. The energy in any hypervelocity impact, such as that between the bumper debris and the electrical insulation, is of sufficient magnitude to form an electrically conductive plasma. Therefore, during an impact, even without physical contact, electrical arcs will be possible between any electrical cables with a voltage difference. For this reason, several double-bumper configurations were tested but will not be discussed here.

MDA Photographic Window Bumper

Penetration tests were also made on the MDA photographic window bumper configuration. This configuration is shown in Figure 12. This configuration consists of a 0.318 cm (0.125 in.) thick fiberglass laminate bumper with 2.54 cm (1.0 in.) of the high performance multilayer insulation bonded

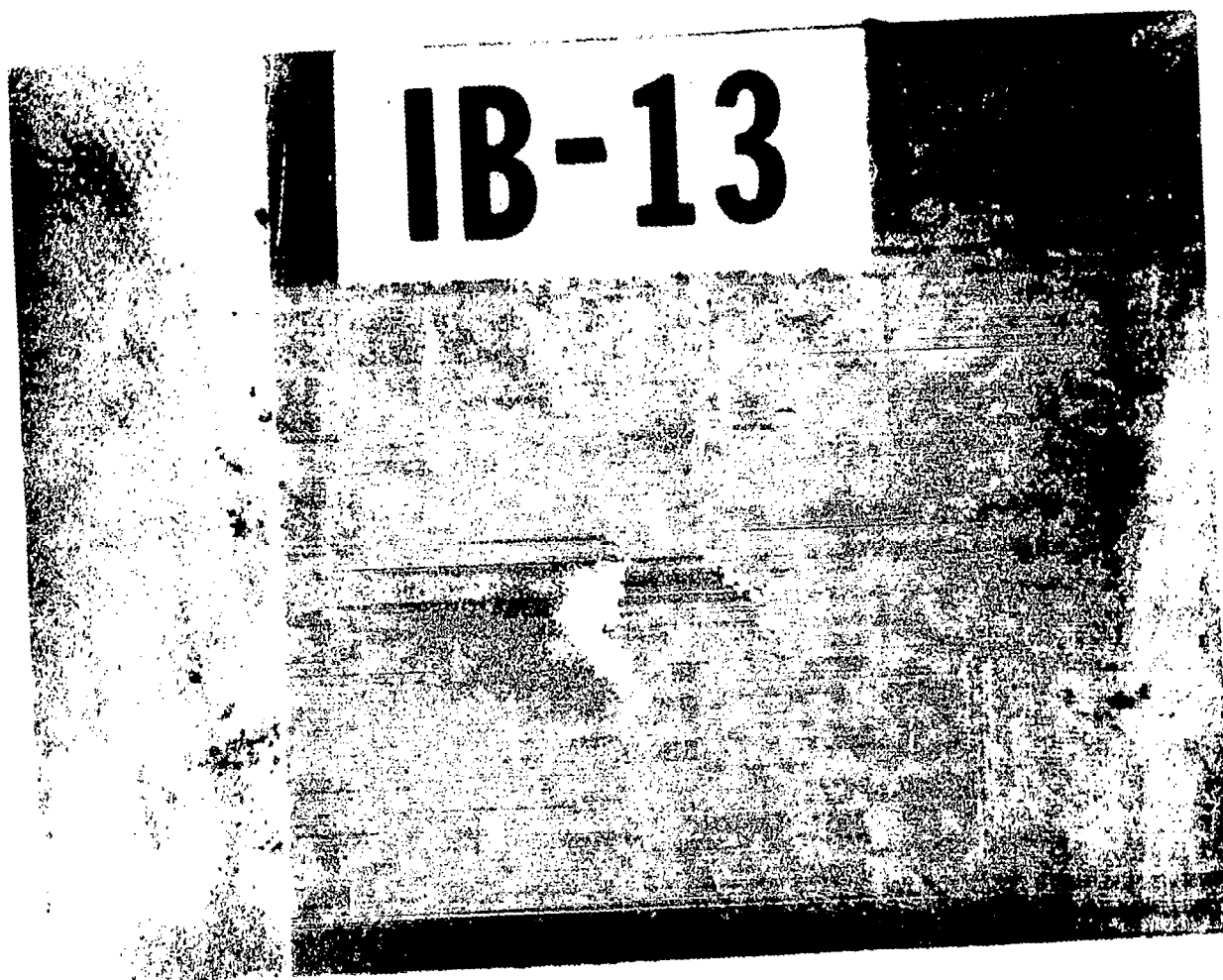


Figure 9. Example of damage when insulation was used.

to the bumper. In this configuration the 5.08-cm (2.0-in.) void is between the insulation and the ultraviolet grade glass of which only a small section is visible. The position of insulation is obviously for the purpose of swinging both the bumper and insulation aside when photographic experiments are desired.

The penetration tests were made with two goals in mind. First, it was desired to find the penetration threshold for the bumper and insulation only. Secondly, it was desired to determine what damage is done to the window when penetration of the bumper and insulation does occur. The penetration tests were made at approximately 6.8 km/sec. To find the threshold, the projectile mass was varied from 0.045 gram down to 0.008 gram. Although the vapor pressure pulse from the impact of the 0.008-gram projectile on the bumper was sufficient to tear a small slit through all layers of the insulation, it was considered the approximate threshold mass

because no particulate material reached the window to cause damage.

Figure 13 shows the damage that was done to the 1.27 cm (0.5 in.) thick window glass by a 0.018-gram projectile at 6.5 km/sec. The view on the left shows the window before it was cleaned in any way. It can be seen that the window is very dark. It is covered with the fine powder produced by the pulverization of multilayer insulation by the bumper debris. This powder adheres quite well as is evidenced by the view on the right which shows the same window after it has been wiped off with a dry paper towel. Some of the surface chipping that is caused by the particulate debris impact can be seen in Figure 13 also. It should be emphasized that even with the larger 0.045-gram projectile, this chipping was strictly surface damage and no structural damage was evident.

Figure 14 is a close-up view of the same glass target shown in Figure 13. This view was taken

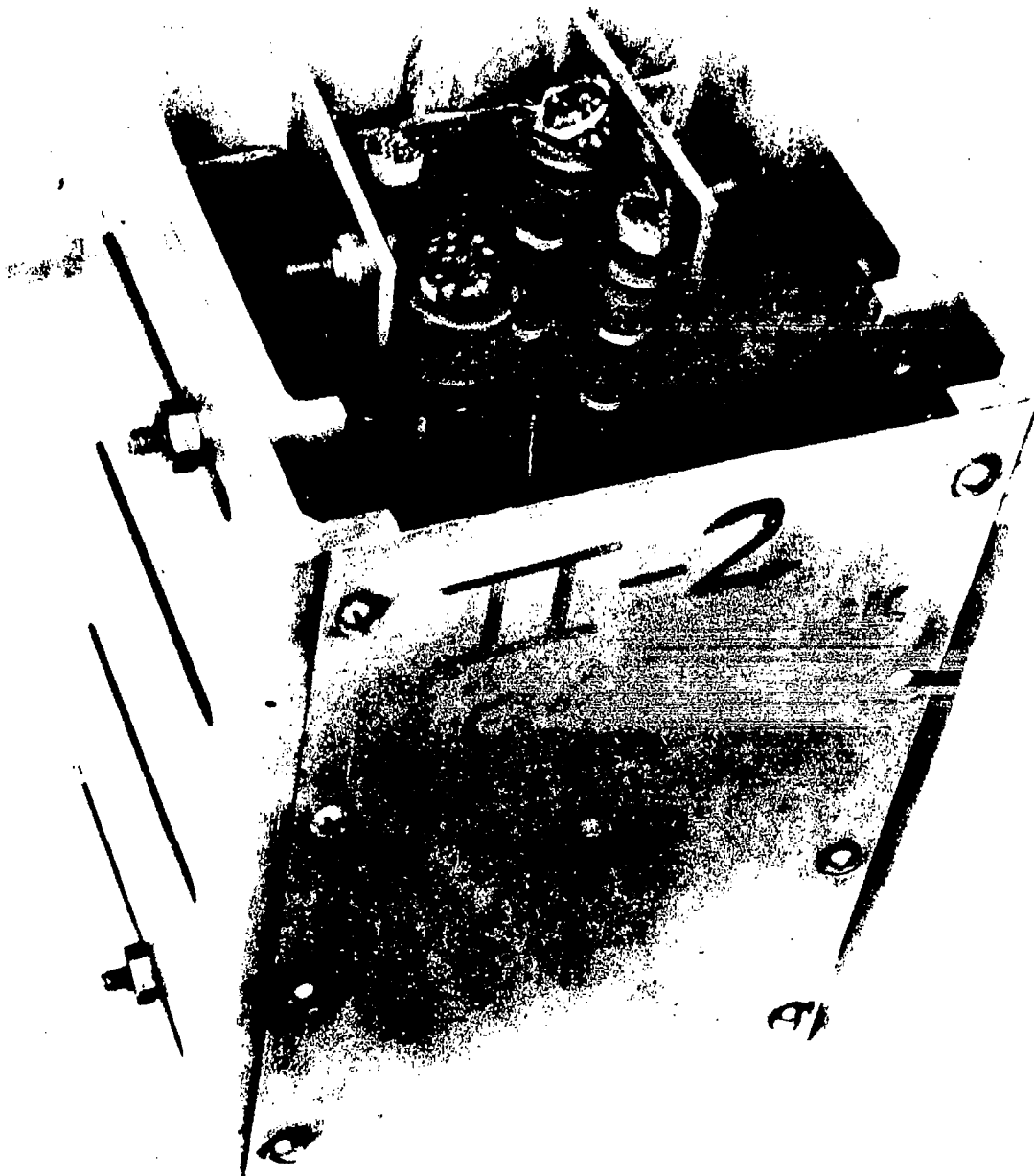


Figure 10. Target configuration for MDA external electrical cable tunnel tests.

after the glass had been cleaned with alcohol. It can be seen that all of the black powder has been removed. There are no smudges on the polished front surface to obscure the saw cut grain on the back surface. The small chips on the glass surface are also quite visible. Although hard to see in this

view, the largest chip shows the conchoidal chip-out, which is the normal damage mechanism in a hypervelocity impact on glass.

The results of these tests show that the window can be protected from meteoroid impact damage



Figure 11. Example of damage received by cable when protected only by bumper.

from a structural standpoint. However, meteoroid damage of the magnitude tested will roughen the surface by chipping over a localized area so that the camera would have to be displaced to an undamaged part of the window. Even this would not help until the black pulverized powder is cleaned from the outside of the window with a solvent.

Low Density Multilayer Insulation

Penetrations were also made on a series of multilayer insulation targets of varying density to

determine what effect density has on the efficiency of defeating a projectile. These targets were all tested with a 0.010-gram aluminum projectile traveling at 6.1 km/sec.

Figure 15 shows the most dense target that was tested. It consists of aluminum foil sheets spaced with a relatively high density adhesive-backed foam. The overall density was 512 kg/m^3 . It can be seen that the projectile penetrated approximately 1.27 cm (0.5 in.). Figure 16 shows approximately 2.54 cm (1.0 in.) of penetration into a medium density (224 kg/m^3) target of aluminum foil and cork. Figure 17 shows a penetration of approximately 5.08 cm (2.0 in.) into a low density (72 kg/m^3) target of aluminum foil and red polyurethane foam. The last target to be shown is in Figure 18. This is a very low density (32 kg/m^3) multilayer target. It is composed of 0.25 mil doubly aluminized Mylar and red polyurethane foam spacers. It is the same material as that called the high performance multilayer insulation used in all the MDA configuration tests. This target was penetrated over 7.62 cm (3.0 in.)

It may seem intuitively obvious that a projectile would penetrate deeper into less dense target material. However, the important conclusions derived from these tests are in the calculations of the penetrated weight. That is, what weight target would be necessary to just stop a given projectile mass. This information is shown in Figure 19. The penetrated thickness is the black line with the scale on the left. The areal density or the weight per unit area necessary to stop the projectile is the dashed line with the scale on the right. Both parameters are plotted versus actual density of material. Looking at the areal density, it can be seen that the very low density (32 kg/m^3) high performance multilayer insulation would need half the weight that the medium and high density materials would need to stop the same projectile. This then is further evidence of the great effectiveness of high performance multilayer insulation in meteoroid protection.

CURRENT RESEARCH

In addition to doing penetration research on basic structures, the current research in the Materials Division Meteoroid Simulation Facility is concerned with studying the reactions of complicated structures to a hypervelocity impact. One method being used is to photograph the target during impact with a sequence camera. The camera being used is a six

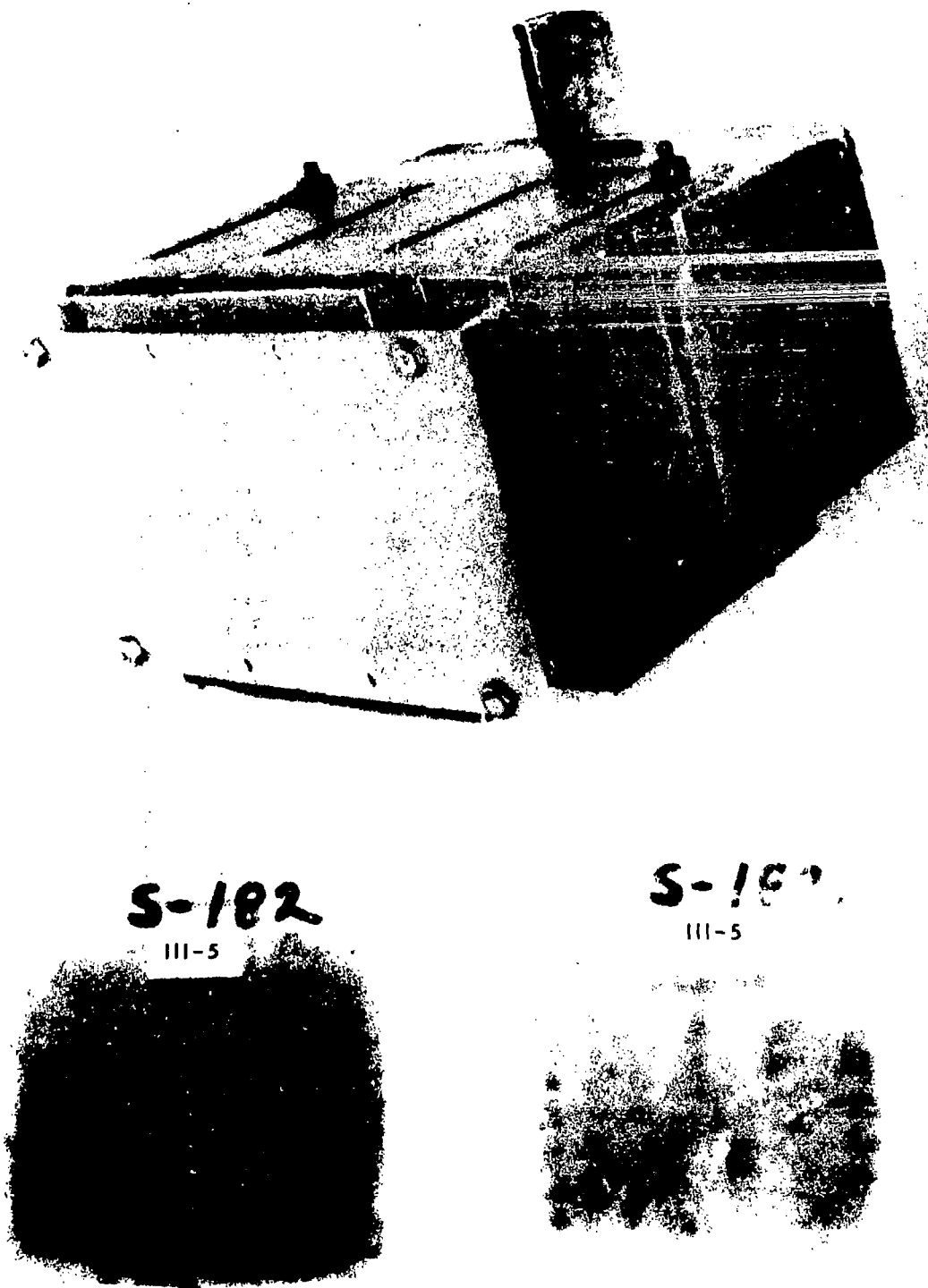


Figure 13. Window condition immediately after test (left) and after being wiped with dry cloth (right).

III-5



Figure 14. Window after cleaning with alcohol.

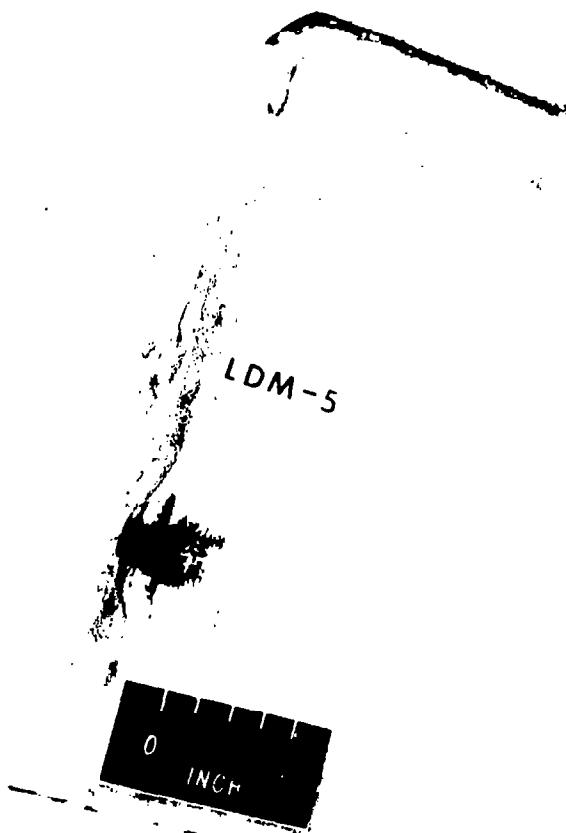


Figure 15. Multilayers of aluminum foil and high density foam.

frame image converter camera with a framing rate of up to 100 million frames per second and exposure times down to 5 nsec.

Figure 20 shows one of the first series of pictures taken with this camera. The four frames were taken at 5- μ sec intervals. The picture at the upper left shows the projectile just coming into view in the grid. This grid was for measurement purposes and was positioned just to the front of a bumper. The second frame at the upper right shows the projectile just having penetrated the bumper. The expanding cloud of debris is already visible. The third frame at the lower left clearly shows the forward traveling debris plus the rearward traveling spray generated in the bumper impact. The fourth frame shows that the debris is not disappearing rapidly but must, in fact, be composed of some relatively slow debris.

Since the foregoing pictures were taken, the optical arrangement for the camera has been greatly

improved. Figure 21 shows two views of a bumper plus backup plate impact with 30 μ sec separating the views. The picture on the left shows the target just after the projectile penetrated the bumper. The grid is behind the backup plate in this arrangement. The debris cloud is already expanding. The bright light on the outside is believed to be the long duration part of the impact flash. The view on the right shows the reaction of the backup plate. The filamentary debris is spall from the back of the backup plate. The tight nucleus of debris in the center is the small plug of material that was punched out of the backup plate.

The optical camera is just one instrument with which a target impact can be studied. Other instruments that will be used are pulsed x-rays, strain gages, and accelerometers. The x-rays will be used for studying the inside of debris clouds and insulation. The strain gages and accelerometers will be used to measure the reaction rates of different structures. This is important because the strength of many materials are strain rate dependent. It is hoped that this type of information will make it much easier for structural design engineers to design meteoroid protection for spacecraft.

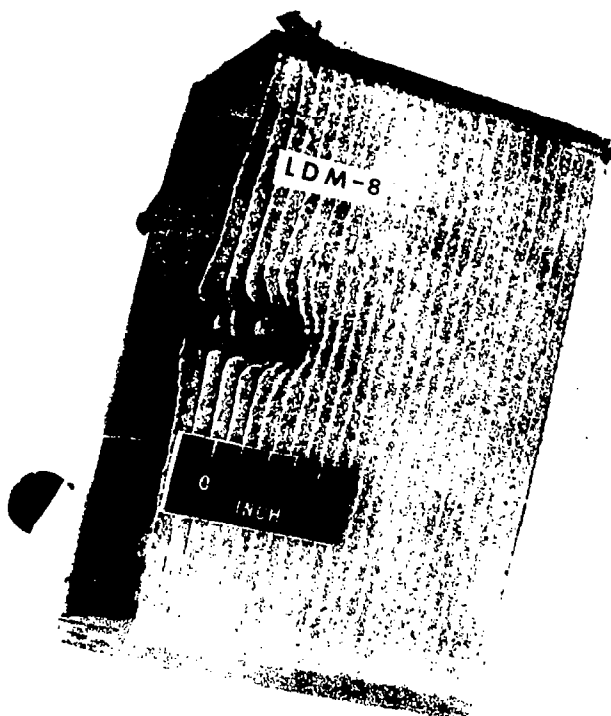


Figure 16. Multilayers of aluminum foil and cork.



Figure 17. Multilayers of aluminum foil and red polyurethane foam.

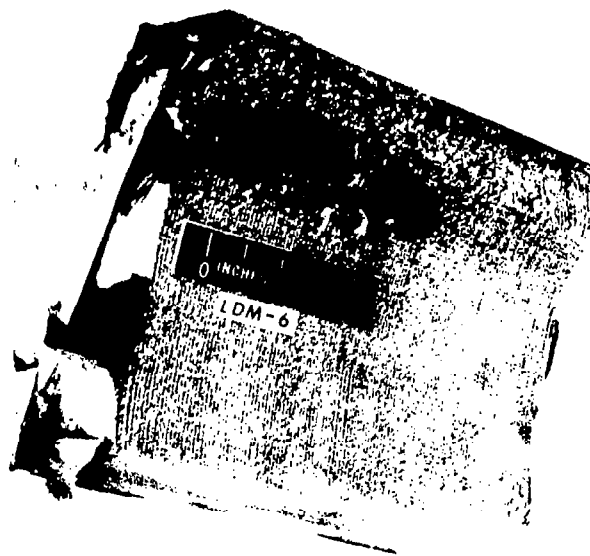


Figure 18. Multilayers of aluminized Mylar and red polyurethane foam.

CONCLUSIONS

The penetration threshold for the basic MDA configuration is 0.190 grams at 5.9 km/sec. The threshold curve for this configuration is much less projectile-velocity dependent than is the curve for an equivalent single sheet. The introduction of a layer of high performance multilayer insulation into the MDA configuration approximately doubles its protective ability relative to projectile mass.

The new sabot stripper design has been a great benefit to the penetration threshold programs by reducing ambiguous test results to a negligible amount. The improvements in launch techniques that allow more accurate velocity predictions have reduced the number of tests needed to arrive at valid penetration threshold data.

Photographic and strain rate monitoring instrumentation can be used to provide information on target reaction to impact. With this information, more effective meteoroid protection structures can be designed.

Tests on various densities of multilayer insulations show that the very low density 0.25 mil doubly aluminized Mylar with red polyurethane foam is approximately twice as efficient as other medium density multilayer structures.

The mechanical damage done to electrical cable protected by a single bumper is not excessive. However, the transient effects such as electrical arcing because of the plasma generated during impact, suggest that a better protection should be found.

REFERENCE

1. Fish, Richard H.; and Summers, James L.: The Effect of Material Properties on Threshold Penetration. Proceedings of the Seventh Hypervelocity Impact Symposium, February 1965.

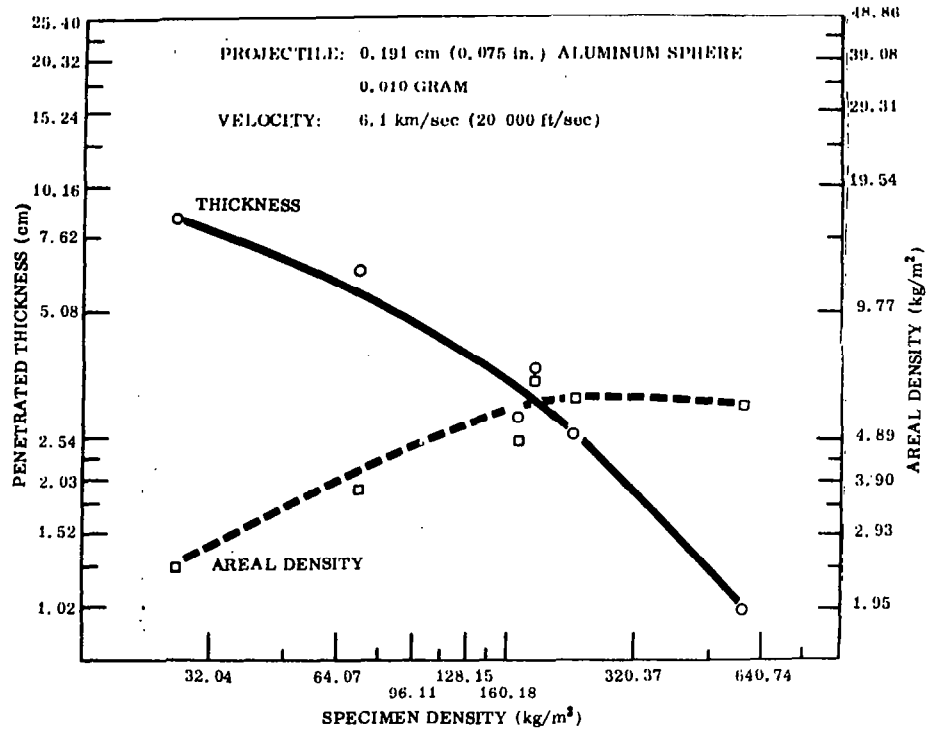


Figure 19. Multilayer target density versus both penetrated thickness and areal density.

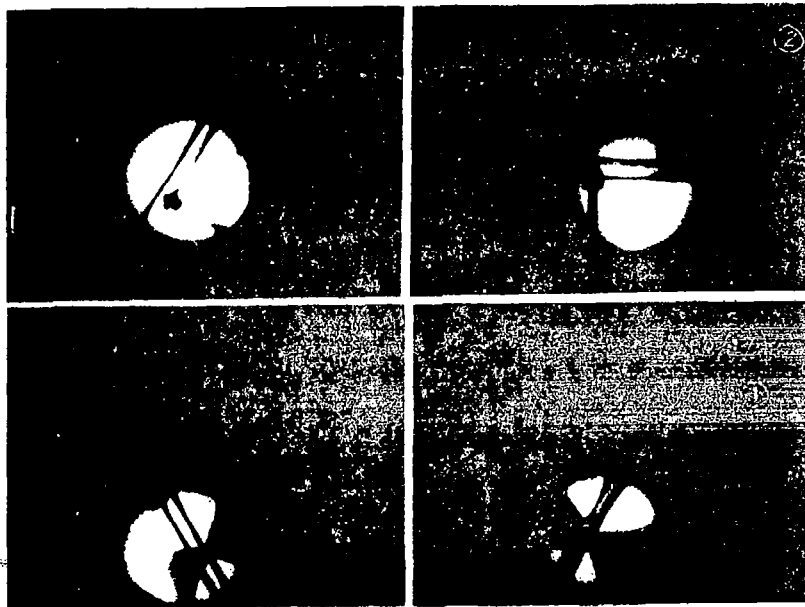


Figure 20. Bumper penetration as photographed by an image converter sequence camera.

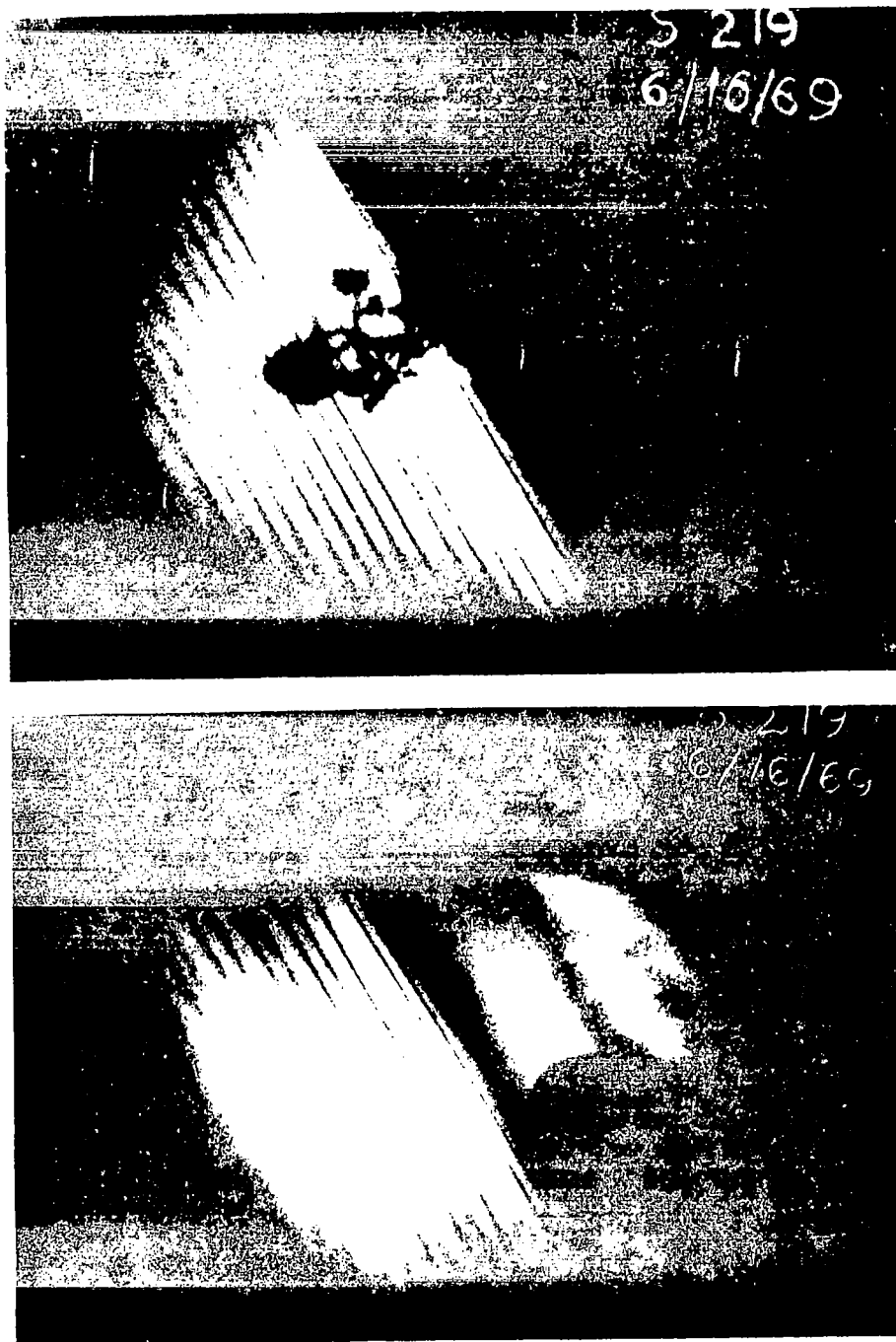


Figure 21. Sequential views of a complete penetration of bumper and backup plate.

N70-3550 8

MHD ACCELERATOR RESEARCH

By

Patrick N. Espy

A continual effort has been made in hypervelocity research to obtain ever-increasing particle velocities for impact testing. Because of their high potential flow rate, hydrogen and helium gases have been used to drive test materials. Using these gases, velocities of some 12 km/sec have been achieved for light gas guns.

As higher velocities were sought, plasmas were considered. Hydrogen, air, aluminum, and other plasmas have been accelerated to high velocities for various types of testing. Included in these tests were hypersonic flow, thermonuclear research, and hypervelocity impact studies. Such plasma velocities were obtained through conical theta- and Z-pinch guns, rail, and coaxial J X B guns.

Marshall Space Flight Center first entered the area of plasma-type hypervelocity particle accelerators through a contract to MB Associates of San Ramon, California. As a result of the initial and subsequent fundings a particle accelerator was developed that produced particle velocities of as much as 15 km/sec from plasmas of 30 km/sec. A system of this type was delivered and placed in operation at Marshall Space Flight Center during this year.

Figures 1 and 2 show the range and instrumentation rack of the original system. Figure 3 shows the capacitor bank. This bank consists of four modules that may be triggered simultaneously through four spark gap switches. A total of 240 kJ is available. These capacitors are dumped into the

gun, which consists of two parallel copper rails shunted by a piece of aluminum foil. The foil is instantly vaporized, and the resulting plasma is accelerated by Lorentz forces of the current discharge through the circuit discharge and through the circuit formed by the rails and plasma. Small glass beads suspended between the rails are drag-accelerated by the plasma to a substantial fraction of the plasma velocity.

After several months of operation in this mode, several improvements became evident. The parallel rails were replaced by a pair of coaxial cylinders as shown in Figure 4. Only a small fraction of the capacitor bank was used initially, with careful attention given to matching the bank to the gun configuration. Velocities were obtained with this configuration that were comparable to those produced by the original device using practically full power. By a careful matching procedure, the bank was gradually increased until plasma velocities exceeding 200 km/sec were measured. Even at these velocities, less than one-fourth the total available energy is being used. Figure 5 shows the range in its present configuration. Figure 6 is a photograph of the plasma emerging from the muzzle taken at an exposure of 5 nsec with the B&W image converter camera.

Having demonstrated our capability for producing extremely high plasma velocities, our research effort is now turning to better plasma diagnostics to determine plasma densities and temperatures, and to using this plasma to accelerate particles.

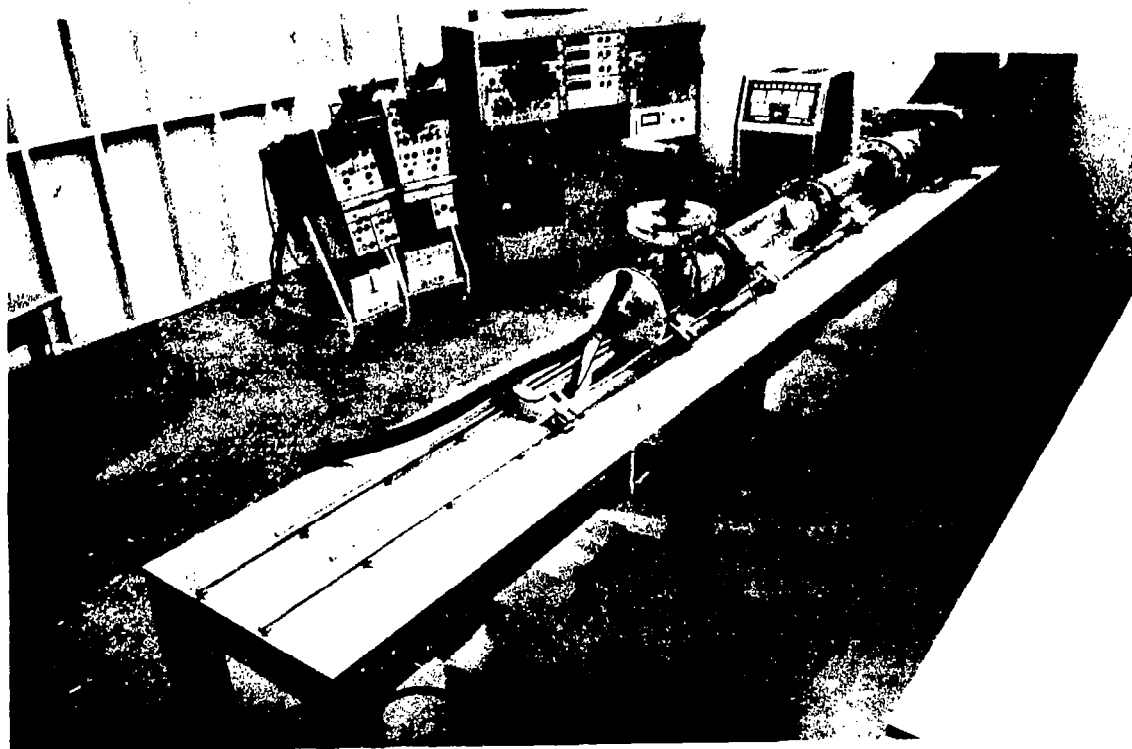


Figure 1. Plasma range showing firing console.

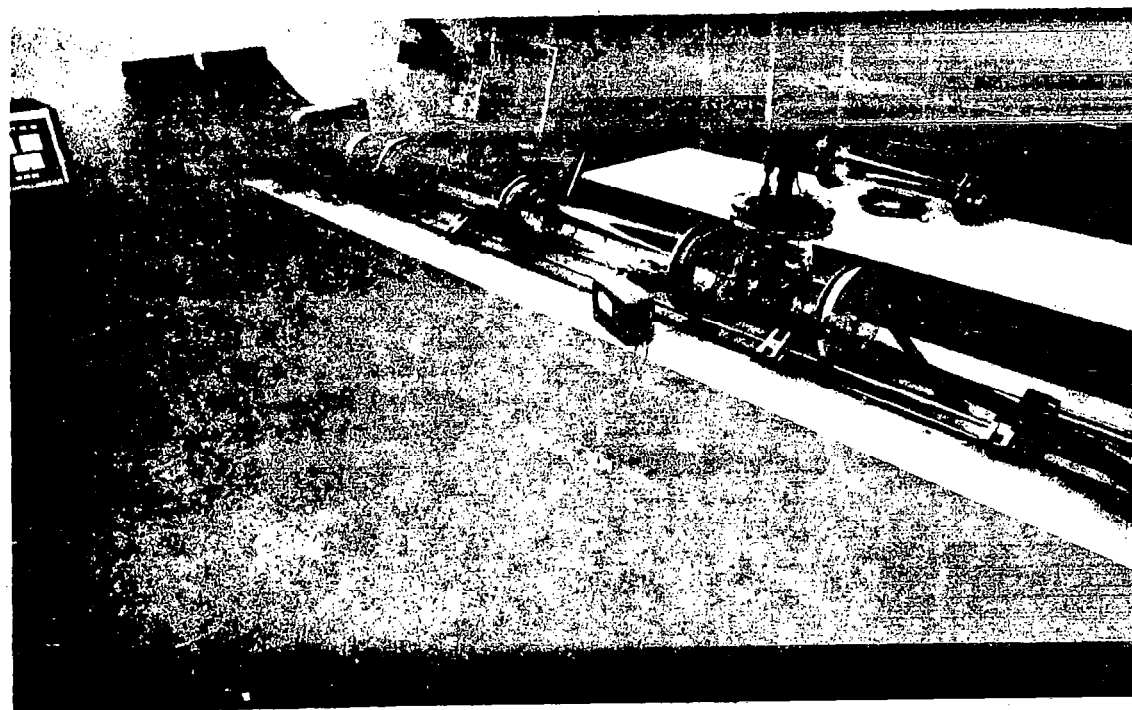


Figure 2. Plasma range from other side.

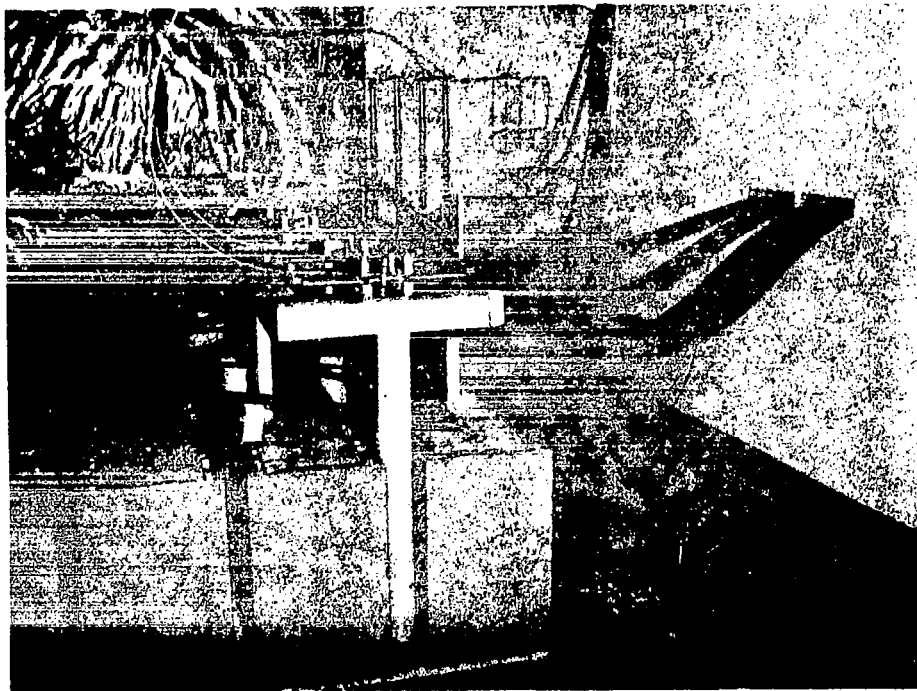


Figure 3. 250 kJ capacitor bank.

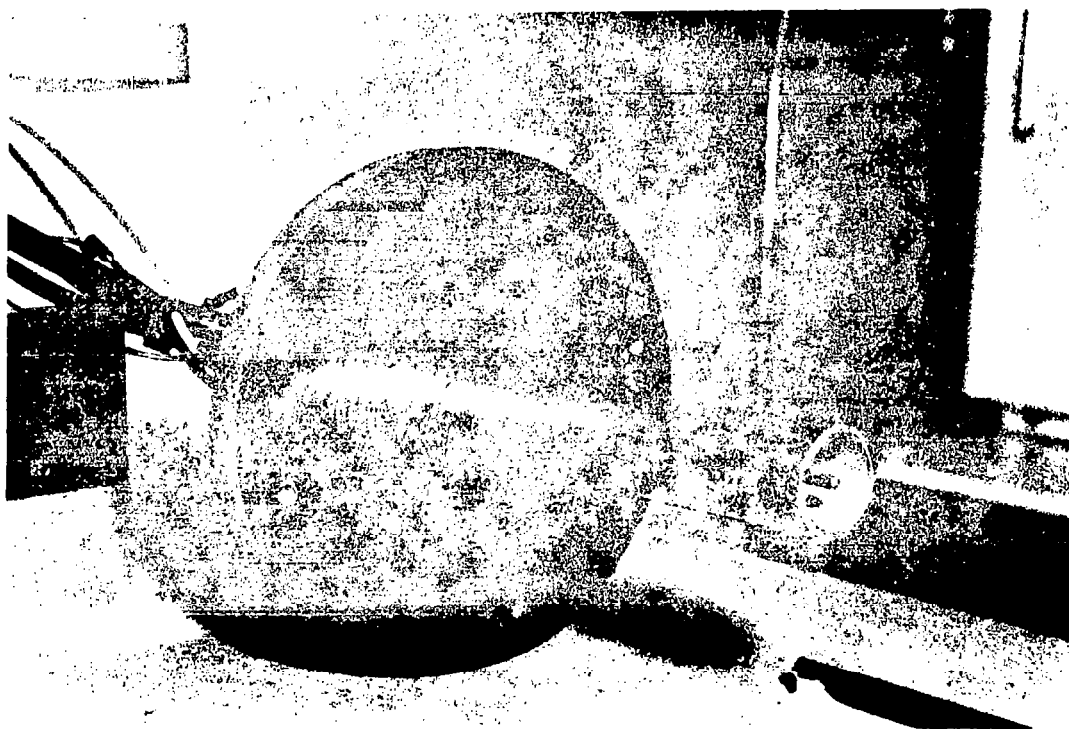


Figure 4. Coaxial gun presently in use.

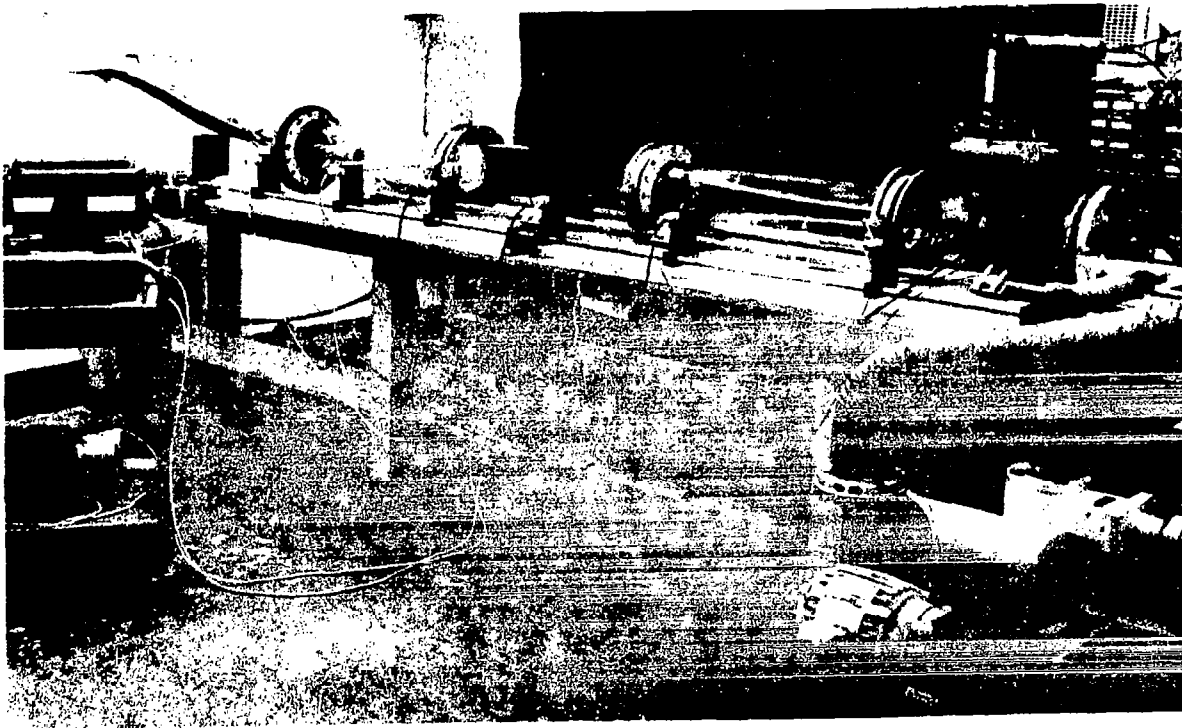


Figure 5. Plasma range with coaxial gun installed.

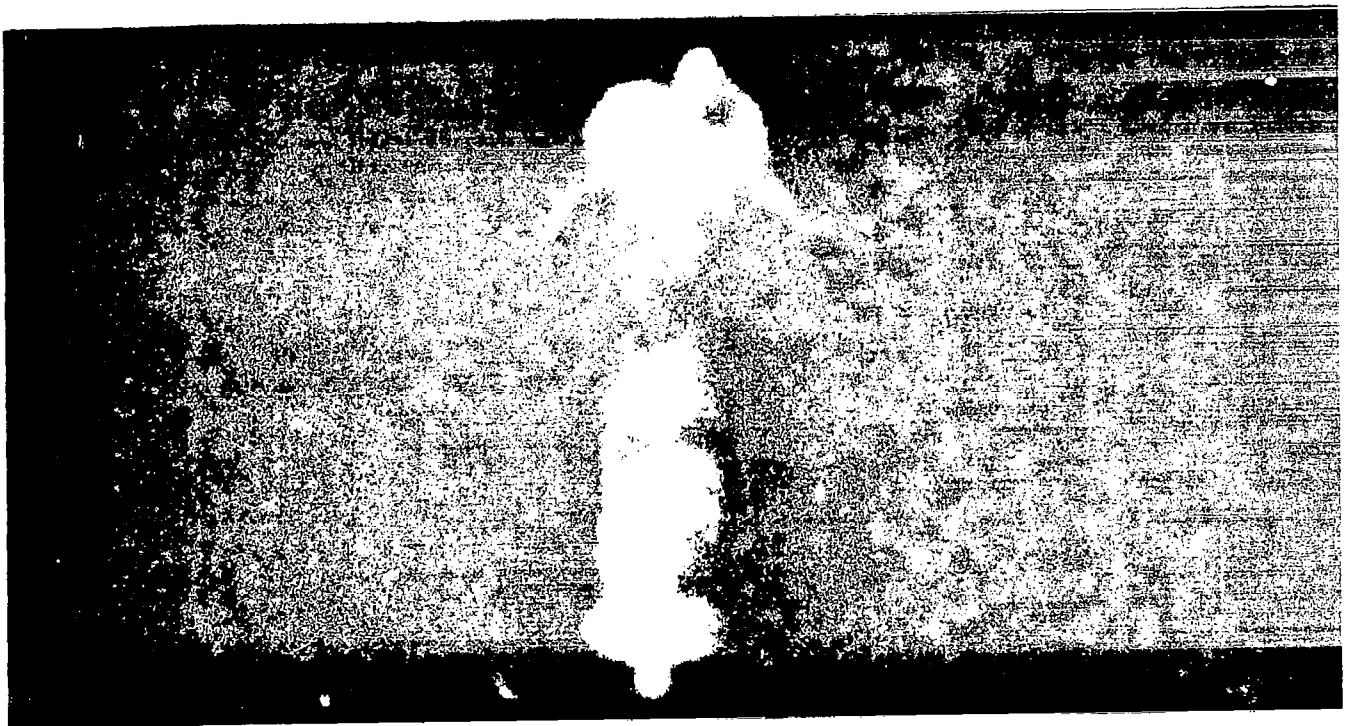


Figure 6. Self-luminous plasma emerging from coaxial gun.

! N70-3550 9

IMPACT CODE DEVELOPMENT

By

R. J. Naumann

Despite the recent improvements in accelerator performance, the prospects for development of a device that can launch fragile, low density meteoroid-like material at 72 km/sec are dim. Therefore, extrapolations of experimental data will probably be relied upon always. Such extrapolations are far more meaningful if they are based on theoretical results.

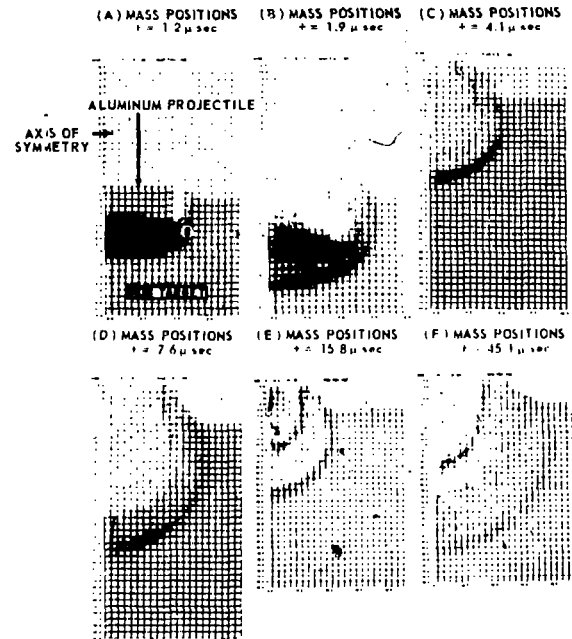
Various computer techniques for treating the problem of hypervelocity impact are available. These have provided the theoretical basis for extrapolating to high velocities and have given a valuable insight into the processes involved in an impact. Bjork pioneered this effort in 1959 utilizing techniques developed by Landshoff and Harlow at Los Alamos. Since that time, various improvements have been made in equations of state and in putting more physics into the code.

Basically, the code solves the inviscid hydrodynamic equations in two dimensions. This requires the simultaneous solution of five nonlinear partial differential equations plus an equation of state in the presence of discontinuous boundary conditions. A set of mass plots for a particular case is shown in Figure 1.

Bjork's earliest work had a disadvantage in the fact that the determination of where the crater would stop growing was based upon subjective judgement. Later, under an MSFC contract, he improved this code to accommodate dissimilar materials and introduced a melting criterion to define crater depth. A series of runs was made of different material combinations at 20 km/sec and at 72 km/sec.

In an attempt to avoid the large computer costs involved in the contract, Brown Engineering Company as a support contractor was given the task of setting up this code for MSFC computers. A case was run for porous aluminum ($\rho = 0.44 \text{ gm/cm}^3$) impacting aluminum at 40 km/sec. The dynamic pressure profiles at various times are shown in Figure 2. Also shown is the residual material strength, which becomes zero at the point where sufficient irreversible work has been done to cause

melting. In accordance with Bjork, this was taken as the crater depth. The results are shown in Figure 3. The point computed by Young at Brown



CASE 8056, ALUMINUM INTO IRON AT 72 KM SEC

Figure 1. Computer studies of impact phenomena represent the material by a series of imaginary mass points. As the impact progresses, the motion of these mass points indicates the material flow. The regions where the mass points cluster to form the darker areas are regions in which the material has been compressed by the strong shock waves generated by the impact. Such shock pressures can be as high as 100 million atmospheres (many times the pressure at the center of the earth). Material behavior at such pressures can be determined from quantum mechanical calculations and has been measured at more modest pressures (1 to 2 million atmospheres) by controlled shock experiments.

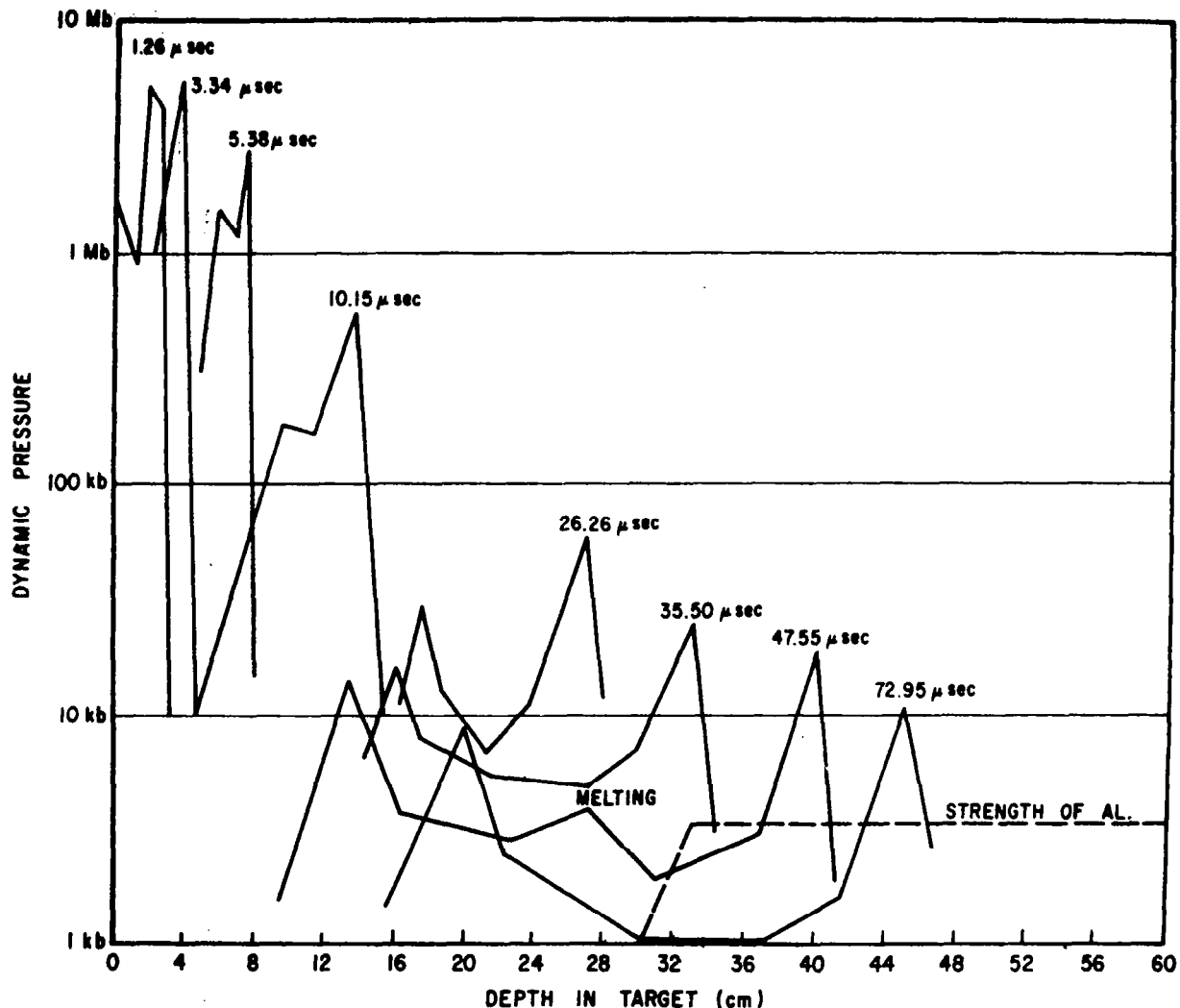


Figure 2. Dynamic pressure profiles.

Engineering Company agrees very favorably with extrapolations between Bjork's 11 km/sec and 72 km/sec result.

These types of codes do not take the strength of material into account in their solution, but as was seen in the preceding argument, the strength was entered in an after-the-fact fashion. Since the melting point was used to define the crater depth, such codes are automatically restricted to cases where strength is ignorable and where the crater depth is determined by melting. These restrictions precluded the check of such codes at available laboratory velocities. A strength code was developed by Bjork that predicted the crater depth of an

aluminum - aluminum impact at 7.35 km/sec. It closely agreed with such a crater produced in the laboratory. Another interesting result from this effort was the prediction of the shock pressure as a function of depth in the target. Figure 4 compares Bjork's results with measured pressures obtained earlier by GMDRL. Note the discrepancy at lower pressures. This is because of the method used at GMDRL to measure the pressure. The technique used was the throw-off-pellet technique developed by Rinehart. In this technique, the pellet traps the momentum imparted as the compression wave engulfs it. By measuring the velocity with which the pellet flies off, the shock pressure can be computed. Figure 5 shows the reason for the discrepancy.

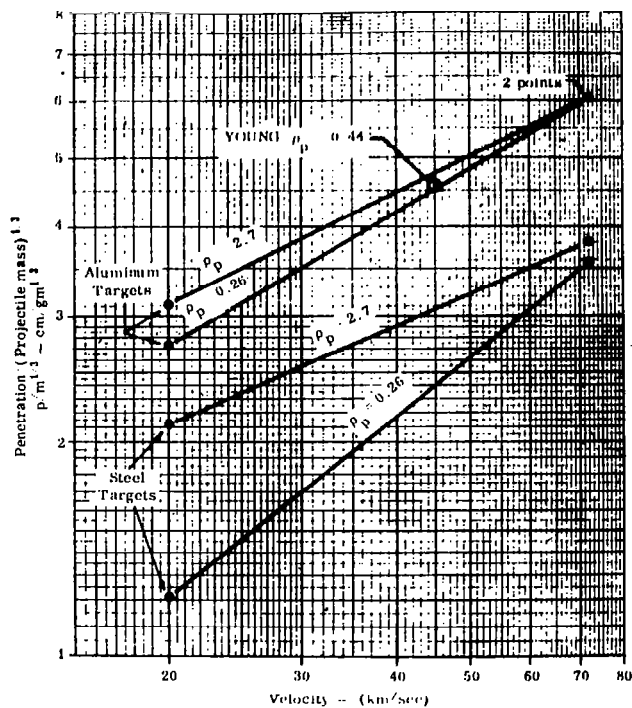
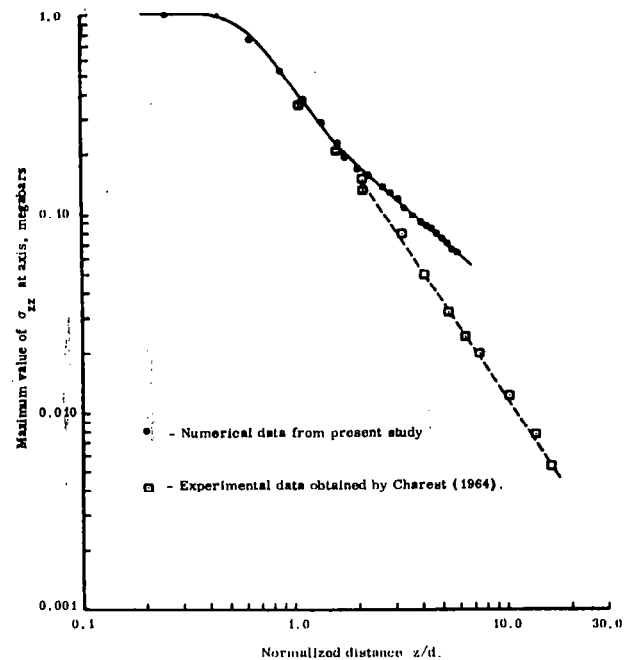


Figure 3. Penetration versus impact velocity.

Characteristic of strength effects is the fact that the structure at lower pressures consists of an elastic precursor wave followed by the plastic wave. Apparently the pellet was trapping the elastic wave, thus flying off with a velocity that was too low.

Another disadvantage of code work is the fact that the code results scale linearly with size, while actual craters do not. A slight tendency for smaller projectiles to crater less effectively has been observed in recent years. Considerable effort has been expended to determine the reason for this departure from size scaling. It was recently shown

Figure 4. Decay of the maximum value of σ_{zz} at the axis with distance into the target.

by Rosenblatt at Shock Hydro that strain rate effects could account for this phenomenon. Unfortunately, strain-rate data are not available for the strain rates involved in hypervelocity impact. When interpolating existing strain-rate data linearly, Rosenblatt obtained so much correction that the projectile actually bounced off the target. A logarithmic interpolation provided approximately the right correction, and Figure 6 shows a scaled large and small crater at two different times. The craters agree favorably with actual impact craters produced by particles of the sizes considered.

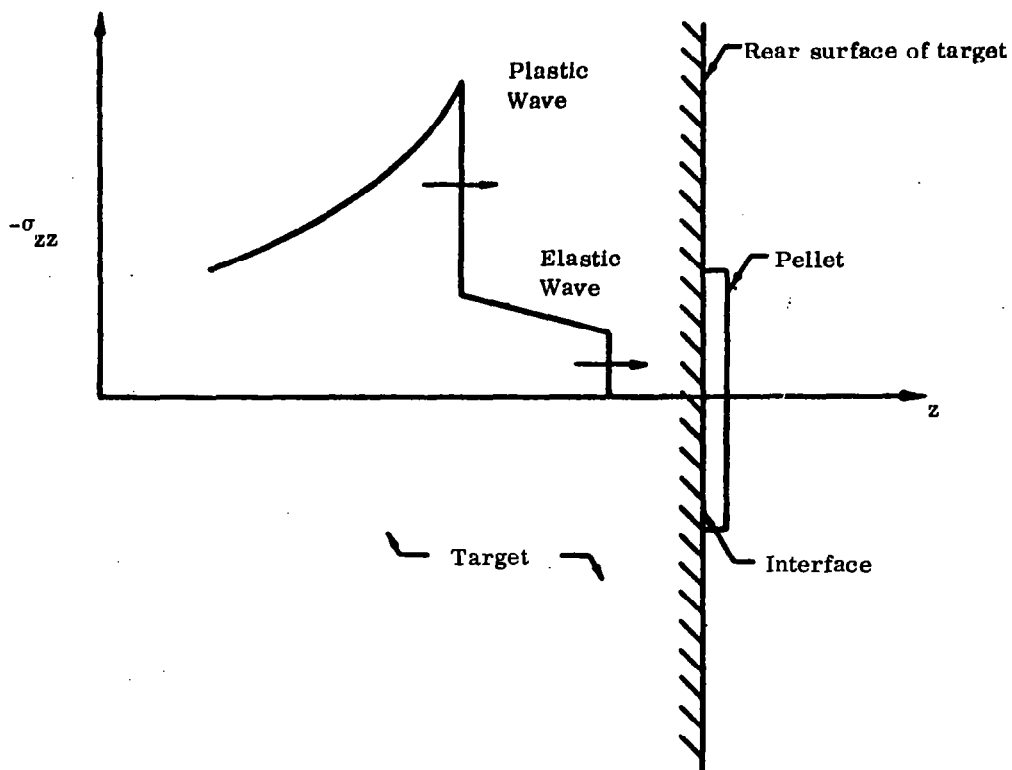


Figure 5. Two-wave shock structure approaching pellet at rear surface of target.

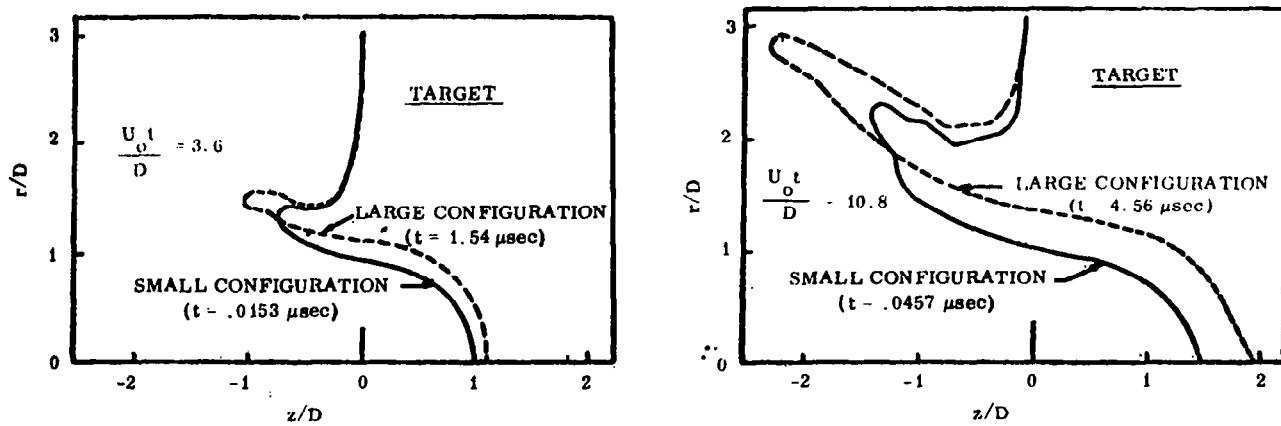


Figure 6. Comparison of crater and splash for different size profiles at scaled times of $U_0 t/D = 3.6$ and 10.8 .

SHOCK PROPAGATION IN SOLIDS IN HYPERVELOCITY IMPACT

By

Tsun-Sen Fu

INTRODUCTION

To protect a space vehicle against meteoroid hazards, it is necessary to understand the meteoroid impact phenomena and the penetration mechanism. The meteoric particles, in spite of usually being small in size, possess high kinetic energies because of their hypervelocity nature (ranging from 11 km/sec to 72 km/sec). The term "hypervelocity impact" is defined generally as the collision of two solid bodies with a relative velocity higher than the elastic wave propagation speed in the material under consideration.

The impact mechanisms are governed by an extremely complex system of nonlinear, partial differential equations with very complicated boundary conditions. Solving this problem analytically is a rather formidable task. Since 1958, several computer programs [1-6] have been developed that permit complete solutions through direct numerical analysis. A survey of this subject reveals that not only is a tremendous amount of computing time required for operating these computer programs, but large errors may develop because of the numerical fluctuations inherent in such solutions. However, the numerical approach is still considered to be the principal approach to obtaining a complete solution of hypervelocity impact.

In addition to the numerical solutions obtained by the computer programs, analytic solutions of hypervelocity impact have been obtained by many authors. An excellent review of such solutions has been given by Rae [7]. So-called analytic treatments of hypervelocity impact usually refer to those approximate solutions that, even though less exact than the numerical methods, are easily obtained and, most important, still display the essential features of the problem. Evidently each approximate method is valid only in a certain regime, since solutions cannot be obtained in a rigorous manner by the available analytic techniques without considerable simplifications.

Blast wave theory [7,8] for instance, gives results in good agreement with direct numerical solutions at a late stage of impact. The blast wave solutions, however, are not applicable to the thin target plate since the thickness of the target is comparable to the projectile dimensions, and the point source assumption is no longer valid. The blast wave solution, however, does reveal the important fact that there exists a close analogy between the shock propagations from explosions and those from hypervelocity impacts.

In the present study, a cylindrical projectile impacting on a target of infinite depth is considered. Immediately after impact, a plane shock is generated on the target surface; the shock area is equal to the circular cross section of the incident cylinder. Attention is then centered on the shock profiles as time elapses. This initial shock condition is considered to be equivalent to a surface explosion of finite area on the target surface. In fact, the surface shock equivalence has also been used by Zeldovich [9], among other Soviet scientists, as the idealized model that describes the initial stage of impacts. He did not, however, actually calculate the shock trajectories as functions of time.

The formulations of the shock profiles in the present study are based on a shock dynamic theory [10 and 11] in fluid mechanics. The two-dimensional method of characteristics is employed to calculate the successive positions of shock waves as a function of time. The equations of state for metals are used in the formulation, and the shock interaction with the free boundary is also considered.

The shortcoming of this theoretical model is that no information on the fluid is given behind the shock wave, except the flow properties deduced from Hugoniot relations. Because that shock wave develops in a semispherical shape in a short time after impact, quasi-similar solutions of blast wave theory [12] are used to approximate the fluid functions in the region behind the shock wave.

The object of this study is to calculate the shock profiles resulting from hypervelocity impact and to use those results in predicting the impact phenomena such as crater formation and spallation fractures. The applications of shock propagations in solid media will be reported later.

A numerical example is given in this report and compared with the existing results of other investigations. The agreement in general is good.

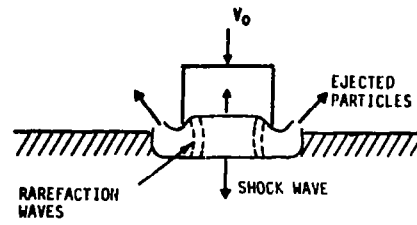
The author wishes to express his appreciation to Mr. Carl Young for his discussions of the problem and to Dr. G. R. Guinn for his guidance and encouragement during the course of this work.

THEORETICAL MODEL OF IMPACT-GENERATED SHOCK PROPAGATION IN SOLID MEDIA

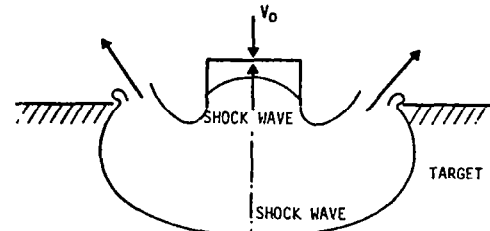
The physical phenomena of a projectile impacting on a target are illustrated schematically in Figure 1, in which a cylindrical projectile traveling at a velocity u_0 is assumed to strike a semi-infinite target. Immediately after the impact (Fig. 1a) there are two strong shock waves moving in opposite directions: one travels forward into the target and the other backward into the projectile. The pressure is so high in the material through which the shock has passed that the material strength is negligible compared with the shock pressure. Therefore the material behind the shock waves is considered to behave essentially as an inviscid, compressible fluid. As the shock wave advanced further into the target material, the plane portion of the shock wave is gradually consumed by the rarefaction waves from the corners (Fig. 1b). The shock front is distorted and attenuated in strength and eventually approaches the shape of a hemisphere.

For extended elapsed time after impact, the crater is formed in the target while the isolated shock wave continues to propagate into the target. Further advancement into the semi-infinite target will cause the shock wave to degenerate into the plastic waves and then into the elastic wave.

Because of the shock geometries, the problem resembles a moving shock configuration of unsteady, supersonic flow. Illustrated in Figure 2 is a normal shock moving along a channel whose wall suddenly enlarged at a certain section. As a result of the



(a) Brief Elapsed Time After Impact



(b) Intermediate Elapsed Time After Impact

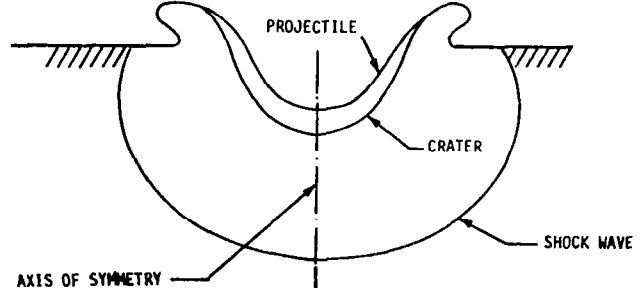


Figure 1. General features of the hypervelocity impact mechanism.

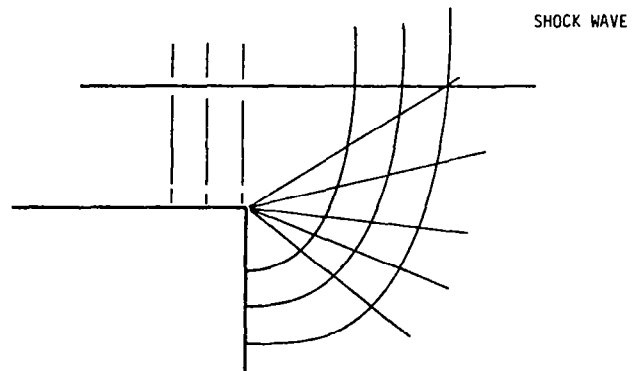


Figure 2. Moving shock front in a suddenly enlarged channel.

enlargement, the shock wave changes its shape as it propagates into an enlarged area with a diminishing

of the plane shock by the rarefaction wave issuing from the corner of the wall. The mathematical formulation of this problem will be given in the next two sections.

Figure 1a also illustrates the manner in which the material particles are splashed upward from the free boundary of the target, and the interaction of the shock waves with the target surface. The interaction between shock waves and the free surface should be considered as the boundary condition in the calculation of shock profiles. (See page 50.)

FORMULATION OF THE CHARACTERISTIC EQUATIONS

The mathematical formulation of the shock profile relationships is based on a shock dynamics theory suggested by Whitham [13] for an originally plane shock with a corner. The two-dimensional computational scheme is essentially the same as that of Skews [10], while the formulation of the axisymmetric case follows a recent paper of Hayes [11]. It should be noted that the formulations of this section only apply to a region away from the free surface of the target. In the neighborhood of the free surface, shock waves and free surface interaction are considered separately and are presented in a later section.

Two-Dimensional Case

In Figure 3, an orthogonal coordinate system (β, t) is constructed to describe the motion of shock waves, where t corresponds to the successive instants of shock wave history and β is called a ray to describe a specific portion of the shock wave in the course of traveling. The basic assumption is that each small portion of the shock, which is bounded by a ray tube, may be treated independently as one-dimensional flow and obeys the shock propagation law. The shock propagation law is a relation between the ray tube area A and the shock velocity U

$$A = A(U) \quad , \quad (1)$$

which will be derived in a later section.

In the physical plane (Fig 4), the arc lengths \overline{PQ} and \overline{PS} are defined as

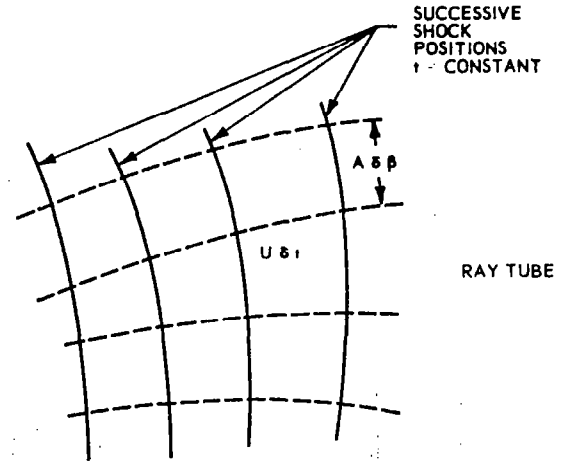


Figure 3. Ray tube coordinates system.

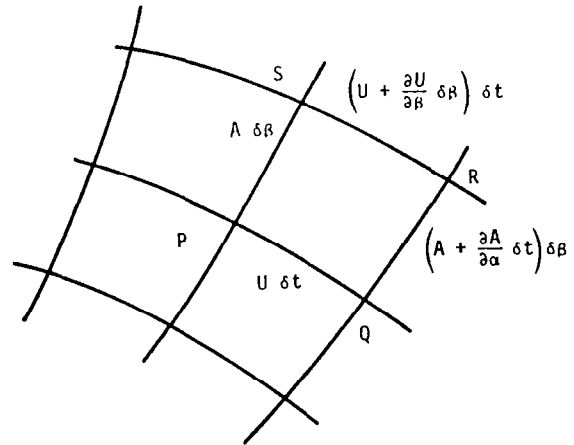


Figure 4. Geometric relation of equations (2) and (3) for the two-dimensional case.

$$\overline{PQ} = U \, dt$$

$$\overline{PS} = A \, d\beta$$

Let $\theta(\beta, t)$ be the angle between the ray and a fixed direction. Then the change of θ from P to S is

$$\delta\theta = \frac{QR - PS}{PQ} = \frac{1}{U} \cdot \frac{\partial A}{\partial t} \cdot \delta\beta \quad ,$$

or

$$\frac{\partial \theta}{\partial \beta} - \frac{1}{U} \cdot \frac{\partial A}{\partial t} = 0 \quad (2.a)$$

Similarly,

$$-\partial \theta = \frac{SR - PQ}{PS} = \frac{1}{A} \cdot \frac{\partial U}{\partial \beta} \delta t \quad (2.b)$$

or,

$$\frac{\partial \theta}{\partial t} + \frac{1}{A} \cdot \frac{\partial U}{\partial \beta} = 0 \quad (3)$$

Notice that the derivations above are obtained for purely geometrical reasons. A combination of equations (2) and (3) indicates the kinematic relation between U and A

$$\frac{\partial}{\partial t} \left(\frac{1}{U} \cdot \frac{\partial A}{\partial t} \right) + \frac{\partial}{\partial \beta} \left(\frac{1}{A} \frac{\partial U}{\partial \beta} \right) = 0 \quad (4)$$

When equation (1) is combined with equation (4), the shock positions are determined for all times. The kinematic relations may be written in terms of U as follows:

$$\frac{\partial \theta}{\partial \beta} - \frac{A'(U)}{U} \cdot \frac{\partial U}{\partial t} = 0 \quad (5)$$

$$\frac{\partial}{\partial t} + \frac{1}{A(U)} \cdot \frac{dU}{d\beta} = 0 \quad (6)$$

or equivalently,

$$\frac{\partial}{\partial t} \left(\frac{A'(U)}{U} \cdot \frac{\partial U}{\partial t} \right) + \frac{\partial}{\partial \beta} \left(\frac{1}{A(U)} \cdot \frac{\partial U}{\partial \beta} \right) = 0 \quad (7)$$

where $A'(U) = \frac{dA(U)}{dU}$

The above equations are analogous to the equations of nonlinear sound waves or two-dimensional steady supersonic flows; hence the existing theories of compressible fluid flows on these topics can be equivalently applied to the present problems.

By the theory of characteristics, equations (5) and (6) yield

$$\left(\frac{\partial}{\partial t} \pm C \frac{\partial}{\partial \beta} \right) \left(\theta \pm \int \frac{dU}{AC} \right) = 0 \quad (8)$$

where C is the equivalent sound speed as follows:

$$C = \left[\frac{-U}{A(U) A'(U)} \right]^{\frac{1}{2}} \quad (9)$$

Let ℓ_+ , ℓ_- be the Riemann invariants of

characteristics C^+ and C^- , respectively. Then equation (8) gives

$$C^+; \theta + \omega(U) = \ell_+ \text{ on } \frac{d\beta}{dt} = C \quad (10)$$

$$C^-; \theta + \omega(U) = \ell_- \text{ on } \frac{d\beta}{dt} = -C \quad (11)$$

and

$$\omega(U) = \int \frac{dU}{AC} \quad (12)$$

Let $m(\alpha, \beta)$ be the angle between a characteristic and a ray (Fig. 5). The characteristic lines have the direction

$$\frac{dy}{dx} = \tan(\theta \pm m) \quad (13)$$

on the physical plane. The positive sign in equation (13) corresponds to left-running characteristics, and the negative sign corresponds to

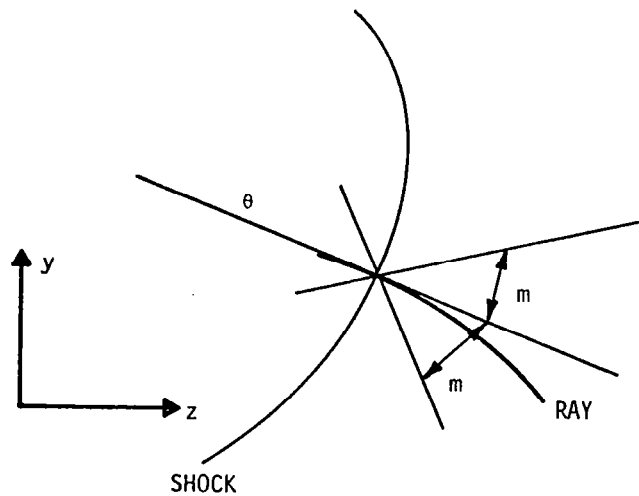


Figure 5. Mach angle in physical plane.

right-running characteristics; m is equivalent to the Mach angle in two-dimensional steady flows.

Figure 6 shows that the increment \overline{PQ} along a left-running characteristic can be related to dt and $d\beta$ in the (β, t) plane as follows:

$$dx = U dt \cos (\theta + m) / (\cos m)$$

$$dy = U dt \sin (\theta + m) / (\cos m)$$

or

$$dx = A d\beta \cos (\theta + m) / (\sin m)$$

$$dy = A d\beta \sin (\theta + m) / (\sin m)$$

and

$$\tan m = \frac{A}{U} \cdot \frac{d\beta}{dt} = \frac{AC}{U} \quad (15)$$

Similar relations can be found for right-running characteristics by simply changing $\theta + m$ to $\theta - m$ in equation (14).

Figure 7 shows that a plane shock, starting at the edge of a solid medium enters a sudden enlargement area at time $t = 0$. For $t > 0$, there are two central fans emitted from the corners, which cause the shock front to expand. The normal shock portion is therefore diminishing in the course of time. Before time t_c (defined in Fig. 7), the physical picture is a simple wave pattern. Therefore U , θ ,

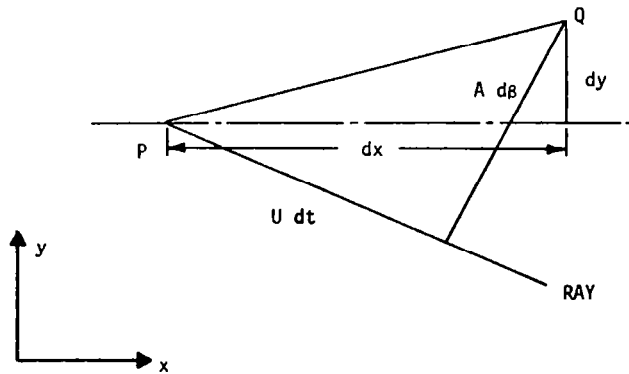


Figure 6. Relation of (x, y) plane and (β, t) plane.

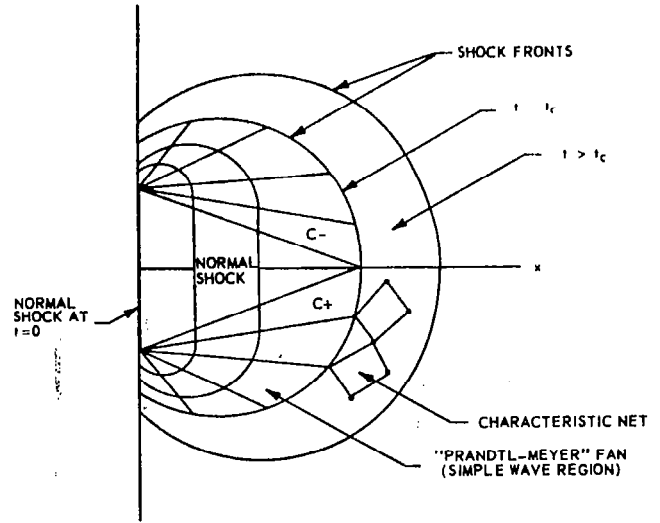


Figure 7. Sketch of shock propagation in solid medium (t_c is the time when the first characteristic line reaches the shock centerline, x -axis,; the normal shock portion vanishes completely for $t \geq t_c$).

and m are invariants along a characteristic line. Direct integration of equation (14) yields

$$\begin{aligned} x/t &= U \cos (\theta + m) / \cos m + x_0 / t, \\ y/t &= U \sin (\theta + m) / \cos m + y_0 / t, \\ x/\beta &= A \cos (\theta + m) / \sin m + x_0 / \beta, \end{aligned} \quad (16)$$

and,

$$y/\beta = A \sin (\theta + m) / \cos m + y_0 / \alpha,$$

where (x_0, y_0) is the initial point. Similarly, changing m to $-m$ in equation (16) gives the integrated equation for right-running characteristics.

When $t > t_c$, the simple wave theory ceases to apply and the shock profiles can be predicted only by constructing the characteristic nets, in the same manner as a two-dimensional nozzle flow field.

The simple wave solution of two-dimensional cases is only hypothetical, since the shock waves generated by the projectile of finite dimensions are

three-dimensional flows. The simplest case for three-dimensional flow is the case of axisymmetry.

In the next subsection, similar treatment shall be given for axisymmetric impact problems. A finite difference numerical scheme is adopted because of the nonexistence of simple wave solutions. To do so, a starting line should be chosen to construct the net of characteristic lines.¹ The solutions on the starting line are the simple wave solutions described in this subsection.

Axisymmetric Cases

As mentioned previously, the characteristic equations for axisymmetric shock propagation can be formulated similar to two-dimensional cases, except that the basic coordinate system (β, t) must be redefined.

To construct the axisymmetric solutions, the basic coordinate system (β, t) is defined such that the distance along a ray between the shock positions given by t and $t + dt$ is $U dt$, and such that $A d\beta/r$ is the distance between the ray β and $\beta + d\beta$; r is the distance from the axis of symmetry and U is the shock velocity (Fig. 8).

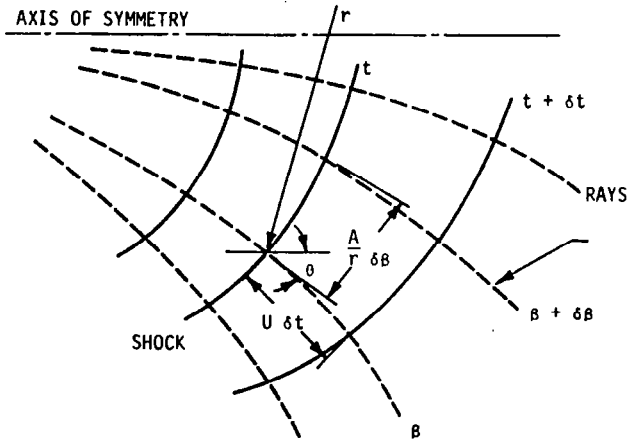


Figure 8. Basic coordinate system of axisymmetric case.

Let $\theta(\beta, t)$ be the angle between the ray and the axis of symmetry. The change of θ from P to S (Fig. 9) is

$$\delta\theta = \frac{RQ - PS}{PQ} = \frac{1}{U} \cdot \frac{\partial}{\partial t} \frac{A}{r} \delta\beta$$

or

$$\frac{\partial\theta}{\partial\beta} - \frac{1}{U r} \frac{\partial A}{\partial t} + \frac{A}{r^2} \sin\theta = 0, \quad (17)$$

where the relation $(U \partial t)/\partial r = \sin\theta$ is used and $\theta = 0$ at the axis of symmetry.

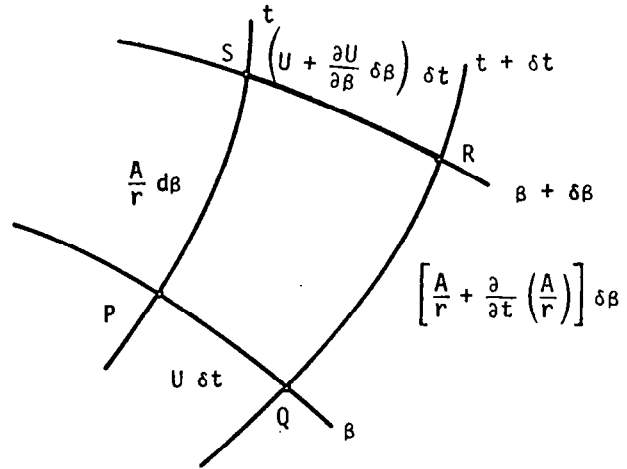


Figure 9. Geometric relation for axisymmetric cases.

A similar treatment for the change of θ from P to Q gives

$$\frac{\partial\theta}{\partial t} + \frac{r}{A} \cdot \frac{\partial U}{\partial\beta} = 0. \quad (18)$$

Let $\delta l = A \delta\beta/r$ be the distance between the rays β and $\beta + \delta\beta$. Equations (17) and (18) then become

$$\frac{\partial\theta}{\partial l} - \frac{1}{A} \cdot \frac{\partial A}{U \partial t} + \frac{\sin\theta}{r} = 0 \quad (19)$$

1. In steady, axisymmetric supersonic flow calculations at the exit of a nozzle, the Prandtl-Meyer expansion fan, which is a simple wave solution, is used to provide such a starting line [14].

and

$$\frac{\partial \theta}{U \partial t} + \frac{\partial U}{U \partial l} = 0 \quad (20)$$

Assume that the shock propagation law, i.e., the shock speed and area relation, is expressed in the form (see page 54).

$$\frac{dA}{A} = -\frac{1}{\mu^2} \cdot \frac{dU}{U}; \mu = \mu(U).$$

Equation (19), then, can be rewritten as

$$\frac{\partial \theta}{\partial \alpha} + \frac{1}{\mu^2} \cdot \frac{\partial U}{U^2 \partial t} + \frac{\sin \theta}{r} = 0 \quad (21)$$

Applying the theory of characteristics in equations (20) and (21) yields

$$\Gamma_{\pm}: \frac{dU}{\mu U} \pm d\theta + \mu \frac{\sin \theta}{r} U dt = 0 \quad (22)$$

along

$$C_{\pm}: \frac{d\ell}{U dt} = \pm \mu, \quad (23)$$

where Γ_{\pm} is the compatibility equation of the physical characteristics C_{\pm} .

For a given initial shock shape, the shock shape at later time can be obtained by constructing a finite difference net in the same manner as that of a steady supersonic jet downstream of the nozzle exit section.

Two boundary conditions are imposed. One is simply that

$$\theta = 0 \quad \text{on} \quad r = 0.$$

The other condition is on the free boundary where the shock wave interacts the free boundary. The interaction will be described in a later section.

HUGONIOT RELATIONS OF SHOCK WAVES IN SOLID MEDIA

When a shock wave moves into a stationary medium, the flow variables across a shock are governed by the following laws:

● Conservation of mass

$$\rho_0 U = \rho (U - u) \quad (24)$$

● Conservation of momentum

$$p - p_0 = \rho_0 U u \quad (25)$$

● Conservation of energy

$$e - e_0 = \frac{1}{2} (p_0 + p) \left(\frac{1}{\rho_0} - \frac{1}{\rho} \right), \quad (26)$$

where U , u , ρ , p , and e are the shock velocity, fluid velocity, density, pressure, and the specific internal energy of the fluid, respectively. The subscript 0 refers to the undisturbed (or stationary) region.

One more relation is needed to solve the flow across a shock; that is, the state equation of the material.

$$e = f(p, \rho) \quad (27)$$

Recently, many studies have been conducted [15-17] on the state equation of solid material. So far, no simple and general equation has been formulated. For the sake of convenience, an equation, which relates the shock velocity and the particle velocity u , is used in this work. In general, there are two forms; one applies to so called c, s material and the other applies to aluminum.

c, s Materials

In Reference 16, McQueen et al. use a linear equation,

$$U = c + s \times \rho u, \quad (28)$$

which relates the velocities U and u for most metals. c is dilatational wave speed and ρ is a constant that is tabulated for 16 materials in their paper. The materials that obey equation (28) are classified as c, s materials.

Substituting equation (28) into equations (24), (25), and (26), the following flow variables are obtained:

$$U = (U - c)/s, \quad (29)$$

$$\rho = \frac{s U}{(s-1) U + c} \rho_0, \quad (30)$$

and

$$\rho = \frac{U (U - c)}{s} \rho_0. \quad (31)$$

The slope of the Rankine-Hugoniot curve in the (P, ρ) plane is given by

$$c_{c-H}^2 = \frac{c^2}{s^2} (2 M_s - 1) [(s-1) M_s + 1]^2, \quad (32)$$

where $M_s = U/c$ is the shock Mach number.

c_{c-H} differs slightly from the adiabatic sound speed as M_s nears 1, but appreciable discrepancy is found for large shock Mach numbers.

The adiabatic sound speed, $a = (\partial p / \partial \rho)_s$, should be derived by an isentropic process that

requires the explicit form of the state equation, equation (27). But for c, s material, the adiabatic sound speed, a , can be obtained approximately in terms of the material constants c and s . The resultant expression is

$$a^2 = \frac{c^2}{s^2} \left[(3s-1)(s-1) M_s^2 - 2(s^2 - 3s + 1) M_s - (2s-1) \right]. \quad (33)$$

A detailed derivation is given in the appendix, and a comparison of a and c_{R-H} is made in

Figure 10.

It is of interest to point out that the c, s material is very similar to an ideal gas. The range of s varies from 1.2 to 1.9 for most metals, which is analogous to the specific heat ratio of gases. It should be stressed, however, that the c, s relation is only an empirical equation. Its accuracy for the shock pressure, greater than 2 mb, is highly questionable.

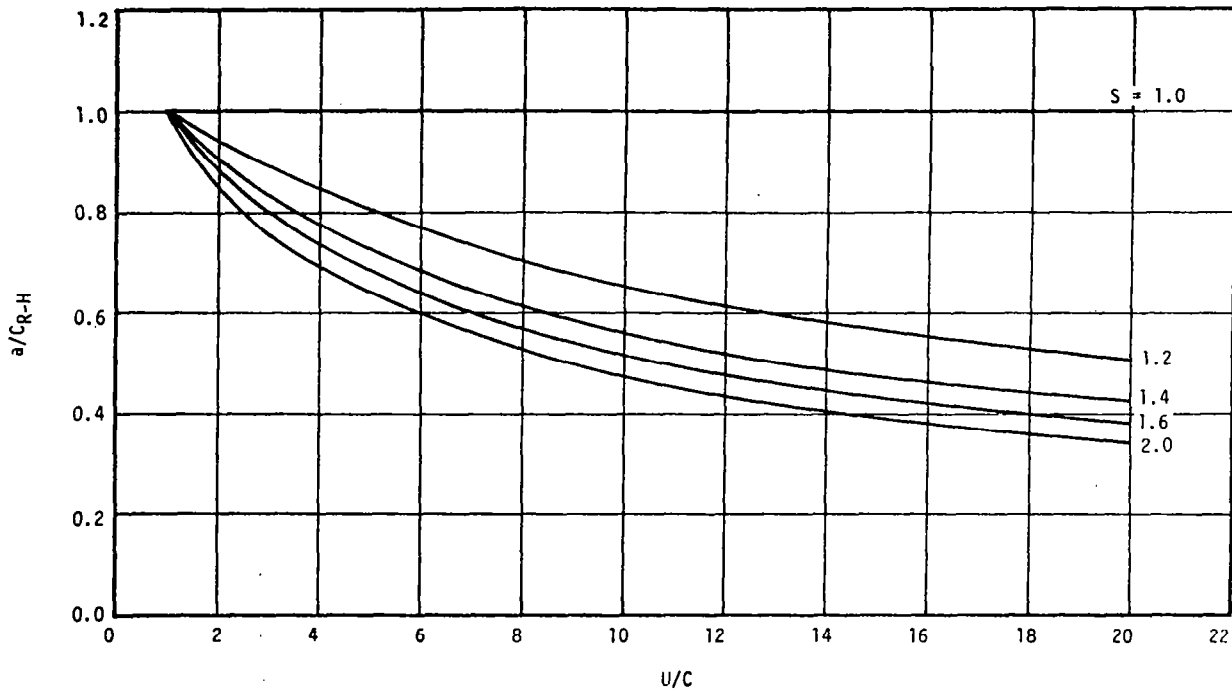


Figure 10. The ratio of adiabatic sound speed and the slope of Rankine-Hugoniot curve as a function of shock Mach number of c, s material.

Aluminum

Aluminum is one of the exceptional metals that do not follow the linear shock relation of equation (28). Instead, the shock relation for aluminum is expressed in a quadratic form as

$$U = a_1 + a_2 u + a_3 u^2 \quad (34)$$

In addition, the adiabatic sound speed a is also a quadratic function of u ; that is,

$$a = b_1 + b_2 u + b_3 u^2 \quad (35)$$

For simplicity, the coefficients a_i and b_i used in this study are obtained by fitting them into the table of Chou et al. [18] (Table 1).

TABLE 1. SHOCK AND ADIABATIC SOUND SPEED CONSTANTS FOR ALUMINUM

	$u \leq 5.0$ (mm/ μ sec)	$u > 5.0$ (mm/ μ sec)
a_1	5.985	5.278
a_2	1.237	1.503
a_3	-0.001	-0.0271
b_1	6.883	5.101
b_2	0.9849	1.518
b_3	-0.0084	-0.048

Chou's table was established by using the Tillotson equation [14] (for $p > 1$ mb) and the experimental data of the Los Alamos Laboratory [16] (for $p \leq 1$ mb).

Again, equation (34), combining equations (24), (25), and (26), provides the shock relations needed in the next section.

SHOCK PROPAGATION LAWS

As mentioned previously, a shock velocity and area relation (equation 1) or shock propagation law, is needed for completing the characteristic solutions. Equation (1) is derived in this section.

Consider a shock wave moving in a channel with varying cross-sectional area. The shock strength will attenuate if the channel area increases downstream; and conversely, the shock wave will be strengthened if the channel area converges. This phenomenon is well-known in blast wave theory. Even if the fluid is assumed frictionless, the shock front velocity decreases very quickly and approaches the velocity of sound at a large distance from the source of explosion. The enlargement of the shock front area results in attenuation of the shock strength, or in the equivalent, a reduction of shock velocity. The shock propagation law relates the change of the shock velocity to the change of the channel area.

The shock propagation law was first obtained by Chester [19] and Chisnell [20] from a linearized approximation of one-dimensional compressible flows. Their results were later rederived by Whitham [21] who applied a simple rule in the non-steady, one-dimensional flow theory. Their result is sometimes called CCW Approximation. In this section a shock propagation law is formulated for solid media.

Whitman's rule can be stated as follows: the flow quantities along a characteristic line must be equal to the flow quantities just behind the shock wave. With this rule and the Hugoniot relation, a differential relation is obtained that describes the motion of a shock wave down a nonuniform area channel. In hypervelocity impact problems, a plane shock is generated initially at the interface between the projectile and the target, and the shock front area suddenly enlarges while it propagates into the target. Then the shock propagation law is applied under the assumption that the whole flow field is composed of a number of one-dimensional rays (see page 43), each one independently obeying this law.

For one-dimensional, unsteady flow in a variable area channel, the governing equations of the fluid flow may be written in the following form:

$$\frac{\partial \rho}{\partial t} + \frac{\partial \rho}{\partial x} + \rho \left(\frac{\partial u}{\partial x} + \frac{u}{A} \cdot \frac{dA}{dx} \right) = 0 \quad (36)$$

$$\frac{\partial u}{\partial t} + u \frac{\partial u}{\partial x} + \frac{a^2}{\rho} \cdot \frac{\partial \rho}{\partial x} = 0 \quad (37)$$

and

$$\frac{\partial e}{\partial t} + u \frac{\partial e}{\partial x} - \frac{P}{\rho^2} \left(\frac{\partial \rho}{\partial t} + u \frac{\partial \rho}{\partial x} \right) = 0 \quad (38)$$

Applying the theory of characteristics to equations (36) and (37) yields

$$\Gamma_{\pm}, \quad d\rho \pm \frac{\rho}{a} du + \frac{\rho u}{A(u+a)} dA = 0 \quad (39)$$

on

$$C_{\pm}, \quad \frac{dx}{dt} = u \pm a,$$

where Γ_{\pm} denotes hodographic characteristics and C_{\pm} denotes physical characteristics.

To apply Whitham's rule, the flow quantities on the outgoing characteristics C_{+} are matched with the flow quantities behind the shock wave. The appropriate branch in equation (39) is

$$\frac{d\rho}{\rho} + \frac{a}{u} \cdot \frac{d\rho}{\rho} + \frac{du}{u} + \frac{du}{a} + \frac{dA}{A} = 0 \quad (40)$$

The terms ρ , a , and u are functions of shock velocity U and the material characteristics. Equation (40) can thus be integrated, and the integrated equation represents the shock propagation law.

For c , s material, equation (40) becomes

$$\frac{dA}{A} = -\mu^2 (M_s) \frac{dU}{U}, \quad (41)$$

where $M_s = U/c$ and

$$\begin{aligned} \frac{1}{\mu^2} &= \frac{1}{[1 + (s-1) M_s]} + \frac{M_s}{M_s - 1} \\ &+ \frac{M_s}{\{[(s-1) M_s + 1] [(3s-1) M_s - (2s-1)]\}^{\frac{1}{2}}} \\ &+ \frac{\{[(s-1) M_s + 1] [(3s-1) M_s - (2s-1)]\}^{\frac{1}{2}}}{(M_s - 1) [1 + (s-1) M_s]} \end{aligned} \quad (42)$$

For the case of strong shock, $M = U s/c \rightarrow \infty$, equation (42) reduces to

$$\mu_{\infty}^2 = \frac{[(s-1)(3s-1)]^{\frac{1}{2}}}{1 + [(s-1)(3s-1)]^{\frac{1}{2}}} \quad (43)$$

For aluminum, the function μ^2 of equation (41) is

$$\begin{aligned} \mu^2 &= \frac{U(u+a)}{u} \frac{1}{U} - \frac{1}{U-u} + \frac{1}{(U-u)(a_2 + 2a_3 u)} \\ &+ \frac{1}{a(a_2 + 2a_3 u)}, \end{aligned} \quad (44)$$

where a and u are functions of U , as shown in equations (34) and (35) of the previous section.

Integration of equation (40) yields, K being an integration,

$$A(U) = K \exp - \int \mu^2 \frac{dU}{U} \quad (45)$$

which is equation (1) on page 43.

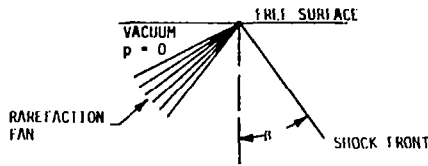
Notice that the integration in equation (45) can be carried out explicitly through a tedious procedure. In actual computations, μ is used instead of $A(U)$. The computational procedures will be discussed in a later section.

SHOCK WAVE INTERACTION WITH FREE BOUNDARY

As stated previously, information about shock-free surface interaction is needed to specify the boundary condition in constructing the characteristic solutions. Figure 11a shows an expansion fan behind the shock, through which the pressure drops from the value immediately behind the shock wave to zero at the tail of the fan. The physical picture is analogous to Prandtl-Meyer expansion around a convex corner except that the expansion fan is three-dimensional and unsteady in nature. The shock front would attenuate and is distorted by the rarefaction waves.

A simplified model has been proposed by Russian scientists [22] to estimate the shock inclination. Recently, Rae [7] applied it to the impact-generated shock propagation, but he chose ideal gases in the formulation. In the present study, Rae's formulation is generalized to solid media.

From Figure 11b, if the shock inclination β is greater than a certain value β^* , called the critical angle, the rarefaction waves cannot reach the shock front. Therefore, if the original shock inclination $\beta > \beta^*$, the shock motion along the free surface will



(a) EXPANSION BEHIND THE SHOCK FRONT

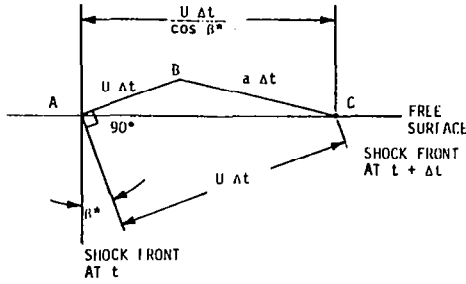
(b) CRITICAL ANGLE β^*

Figure 11. Shock wave and free surface interaction.

not be affected by the free surface interaction. Conversely, if $\beta > \beta^*$, β will change continuously and eventually approaches β^* . The shock will remain undistorted afterward.

The transition phenomenon ($\beta \rightarrow \beta^*$) is rather complex in mathematical analysis, because an unsteady and three-dimensional flow problem is involved. In this work, it is assumed that the transition period is so short in the development of shock profiles that it can be neglected. Then $\beta = \beta^*$ will provide the boundary condition at the free surface. β^* depends on the local shock strength and is derived below.

Referring to Figure 11b, the cosine law gives

$$\overline{BC}^2 = \overline{AB}^2 + \overline{AC}^2 - 2 \overline{AB} \cdot \overline{AC} \cos \beta^*$$

or

$$a^2 = u^2 + U^2 / \cos^2 \beta^* - 2uU$$

and

$$\beta^* = \cos^{-1} \left[\left(\frac{a^2}{U^2} - \frac{2u}{U} + \frac{u^2}{U^2} \right)^{-\frac{1}{2}} \right] \quad (46)$$

Equation (46) indicates the critical shock inclination angle β^* , as a function of U , u , and a . Since a and u can be expressed in terms of U , β^* actually depends on shock velocity U only.

CONSTRUCTION OF NUMERICAL SOLUTIONS FOR SHOCK WAVE PROPAGATIONS

Initial Normal Shock Waves

When a projectile impacts on a target with relative velocity V , two normal shock waves are generated at the interface and move in opposite directions with respect to the interface (Fig. 12a). The normal shock solutions can be obtained easily by applying equations (24), (26), and (28) or (34).

For similar material hypervelocity impacts, the particle velocity equals one-half the impact velocity (Fig. 12b),

$$u_3 = u_2 = V/2 \quad (47)$$

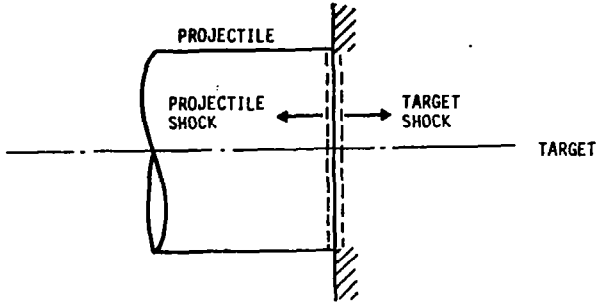
Equation (47) is derived by taking a velocity transformation. If the projectile and the target move in opposite directions with the same speed $V/2$, the fluid particles behind the shock waves should be motionless, because of symmetry, with respect to the laboratory coordinate system.

For nonsimilar material impacts, a contact discontinuity interface exists. The pressure and velocity functions are assumed continuous, however, across the interface; $p_3 = p_2$ and $u_3 = u_2$. From equation (2b)

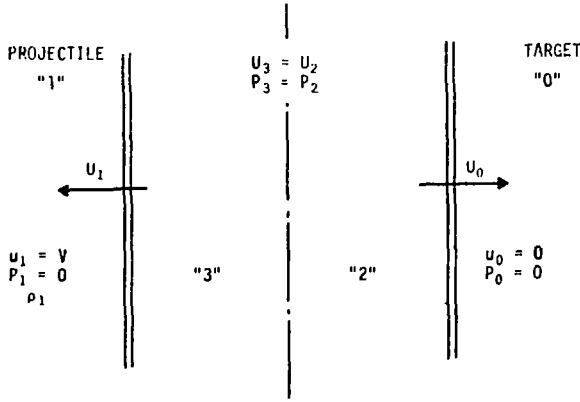
$$p_2 = \rho_0 u_2 U_0 \quad (48)$$

and

$$p_3 = \rho_1 (V - u_3) (V - U_1)$$



(a) NORMAL SHOCKS GENERATED IMMEDIATELY AFTER IMPACT



(b) NORMAL SHOCK MECHANISM

Figure 12. Impact-generated normal shock waves.

With the aid of shock relations, equations (28) or (34), the solutions of U_1 and U_0 are readily found.

Simple Wave Solutions

As shown in Figure 13, U_0 is assumed to be the normal shock velocity calculated in equation (47) or equation (48). Then the Mach angle m_0 can be obtained from equations (15) and (41),

$$m_0 = \tan^{-1} [\mu(U_0)] \quad (49)$$

and

$$\theta_0 = 0$$

Next, choose a shock velocity U_1 , $U_1 < U_0$, and calculate m_0 in equation (49). The shock angle

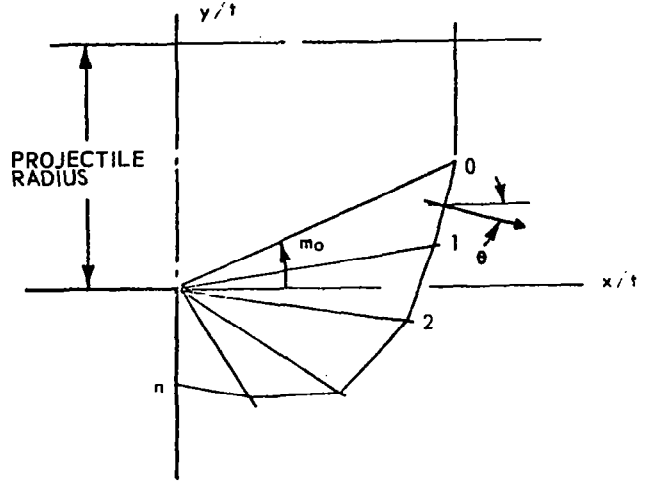


Figure 13. Construction of a simple wave solution.

θ_1 is

$$\theta_1 = \int_{U_0}^{U_1} \frac{dU}{U \mu(U)} \quad (50)$$

The shock position of point 1 is determined by

$$\frac{x_1}{t} = U_1 \cos(\theta_1 + m_1) / \cos m_1$$

and

$$\frac{y_1}{t} = U_1 \sin(\theta_1 + m_1) / \cos m_1 \quad (51)$$

where t is the time after impact.

Repeating the procedure, by choosing a sequence of shock velocities $U_2, U_3, U_n, m_1, \theta_1, x_1/t, y_1/t$ ($i = 2, \dots, n$) are determined in the same manner. The computations continue until $x_i/t = 0$. This completes the construction of a simple-wave solution.

Asymptotic Solution of Two-Dimensional Shock Profiles For Strong Shock

An analytic expression of shock profiles can be obtained for large U in simple wave solutions. c , s material is chosen in the formulation that follows.

The function $\mu(U)$ for a c, s material in the shock propagation law approaches a constant as $U \rightarrow \infty$ (equation 43), and is denoted by μ_∞ . Therefore,

$$\theta = \frac{1}{\mu_\infty} \int_{U_0}^U \frac{dU}{U} = \frac{1}{\mu_\infty} \ln(U/U_0) \quad ,$$

and

$$U = U_0 e^{\mu_\infty \theta} \quad (52)$$

The shock wave locus is in the form

$$\frac{x}{U_0 t} = e^{\mu_\infty \theta} \cos(\theta + m_\infty) / \cos m_\infty \quad ,$$

and

$$\frac{y}{U_0 t} = e^{\mu_\infty \theta} \sin(\theta + m_\infty) / \cos m_\infty \quad , \quad (53)$$

where $m_\infty = \tan^{-1} \mu_\infty$ is also a constant.

Letting $R = (x^2 + y^2)^{1/2}$, equation (53) may be expressed in polar coordinates as

$$R = k e^{\mu_\infty \varphi} \quad , \quad (54)$$

where

$$\varphi = \theta + m_\infty$$

and

$$k = \frac{U_0 t}{\cos m_\infty} e^{-m_\infty} \quad .$$

Equation (54) (Fig. 14) represents a logarithmic spiral curve, and has been derived by Skew [10] for an ideal gas. However, it should be emphasized that equation (52), must be used with caution since the simple linear shock relation of c, s material may not be valid for very strong shocks.

Finite Difference Solutions of the Characteristic Equations

For an axisymmetric impact problem, the simple wave solution only provides the initial condition. Two boundary conditions are used:

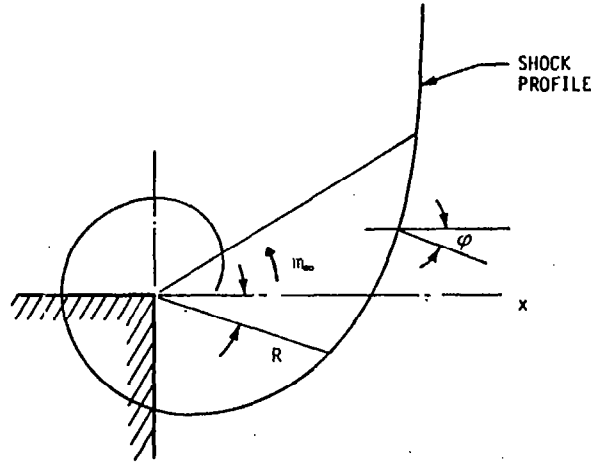


Figure 14. Approximate shock profile for the strong shock situation (U large).

- $\theta = 0$ at the axis of symmetry
- $\theta = -\left(\beta^* + \frac{\pi}{2}\right)$ on the free surface.

The method of characteristics is applied in computing the shock profiles. To do this, the characteristic equations, equations (22) and (23), are first written in finite difference forms, and the solutions can be constructed by the standard technique in the compressible flow theory [14].

The finite difference scheme developed herein differs from the conventional method. The present scheme is designed to construct the shock profiles for successive time intervals. Instead of using two known field points to obtain the third new point, only one point and the time interval Δt are required to determine a new point. The advantage in this numerical scheme is that the successive shock profiles as a function of time can be directly computed without interpolations between the field points.

The computations for this study are programmed on the IBM 1130 digital computer.

AN APPROXIMATION FOR PRESSURE PULSE AT LATE STAGE OF IMPACT

The shortcoming on the present shock propagation model is that no solutions about the flow variables are given behind the shock wave. The flow field of a diffracting shock wave is too

complicated to be obtained analytically. This is the essential reason for the development of direct numerical programs, such as PIC code and Eulerian code. In fact, the flow variables are significant in the description of the impact mechanism.

At the late stage of shock propagation, it is found that the shock front develops rapidly into a sphere-like shape, and the flow variables vary slowly along the shock front. These facts suggest that it is possible to obtain an approximation for the flow field at the large elapsed time.

To find the approximate solutions in the flow field, the equations for three-dimensional, unsteady flow with symmetric axes are written in a spherical coordinate system. These equations are

$$\begin{aligned} \frac{\partial u_r}{\partial t} + u_r \frac{\partial u_r}{\partial r} + \frac{u_\varphi}{r} \cdot \frac{\partial u_r}{\partial \varphi} - \frac{v^2}{r} + \frac{1}{\rho} \frac{\partial p}{\partial r} &= 0, \\ \frac{\partial u_\varphi}{\partial t} + u_r \frac{\partial u_\varphi}{\partial r} + \frac{u_\varphi}{r} \cdot \frac{\partial u_\varphi}{\partial \varphi} + \frac{u_r u_\varphi}{r} + \frac{1}{\rho r} \cdot \frac{\partial p}{\partial \varphi} &= 0, \\ \frac{\partial \rho}{\partial t} + u_r \frac{\partial \rho}{\partial r} + \frac{u_\varphi}{r} \cdot \frac{\partial \rho}{\partial \varphi} + \rho \frac{\partial u_r}{\partial r} + \frac{1}{r} \frac{\partial u_\varphi}{\partial \varphi} + \frac{\partial u_r}{\partial r} \\ + \frac{u_\varphi}{r} \cos \varphi &= 0, \end{aligned} \quad (55)$$

and

$$\begin{aligned} \frac{\partial e}{\partial t} + u_r \cdot \frac{\partial e}{\partial r} + \frac{u_\varphi}{r} \cdot \frac{\partial e}{\partial \varphi} - \frac{p}{\rho^2} \frac{\partial \rho}{\partial t} + u_r \frac{\partial \rho}{\partial r} \\ + \frac{u_\varphi}{r} \cdot \frac{\partial e}{\partial \varphi} &= 0, \end{aligned}$$

where u_r and u_φ represent the velocity components in the r and φ directions, respectively (Fig. 15).

Expanding the variable u_r , u_φ , ρ , and P in Fourier series yields

$$u_r(r, \varphi, t) = u_o(r, t) + \sum_{n=1}^{\infty} u_n(r, t) \cos n\theta, \quad (56)$$

$$u_\theta(r, \varphi, t) = \sum_{n=1}^{\infty} v_n(r, t) \sin n\theta, \text{ etc.}$$

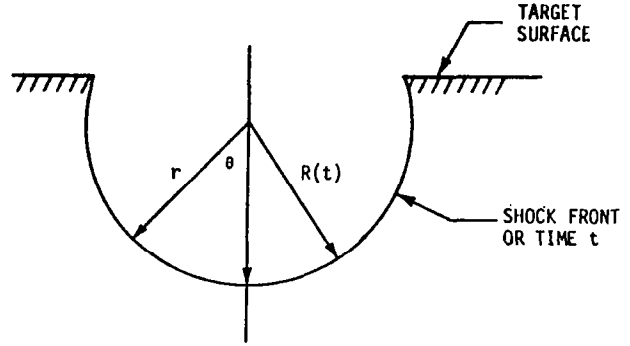


Figure 15. Spherical coordinate system with symmetric axis.

By substituting equation (56) into equation (55), the zero order equations are obtained as follow:

$$\begin{aligned} \frac{\partial \rho}{\partial t} + \rho \frac{\partial u}{\partial r} + u \frac{\partial \rho}{\partial t} + \frac{\partial \rho u}{r} &= 0 \\ \frac{\partial u}{\partial t} + u \frac{\partial u}{\partial r} + \frac{1}{\rho} \cdot \frac{\partial p}{\partial r} &= 0 \\ \frac{\partial e}{\partial t} + u \frac{\partial e}{\partial r} - \frac{p}{\rho} \frac{\partial \rho}{\partial t} + u \frac{\partial \rho}{\partial r} &= 0 \end{aligned} \quad (57)$$

In the above system of equations, $u = u_r$ and the subscript o is dropped.

Equation (57) is identified as a one-dimensional, unsteady flow equation system. A transformation of the dependent and independent variables is introduced as

$$\begin{aligned} u &= U f \\ p &= \rho_o U^2 g, \\ \rho &= \rho_o h, \\ \xi &= \frac{r}{R}, \end{aligned} \quad (58)$$

$$\lambda = \frac{R}{U} \cdot \frac{dU}{dR}$$

and

$$U = \frac{dR}{dt},$$

where R is the shock front position. The first two equations of equation (57) become

$$(f - \xi) \frac{\partial h}{\partial \xi} + h \frac{\partial f}{\partial \xi} + \frac{2fh}{\xi} = -\lambda U \frac{\partial h}{\partial U} \quad (59)$$

$$(f - \xi) \frac{\partial f}{\partial \xi} + \lambda f + \frac{1}{h} \frac{\partial g}{\partial \xi} = -\lambda U \frac{\partial f}{\partial U} \quad (60)$$

Note that f , g , and h are functions of two variables, ξ and $R(t)$. To solve the above system of equations is still a very difficult task. In general, the similarity solutions do not exist because the assumption of a strong condition may not be justified. In fact, when the impact-generated shock wave becomes spherical in shape, the shock strength is usually weak.

Now, two assumptions are imposed as follow:

$$f = f_1 \xi$$

$$\frac{\partial h}{\partial U} = \frac{h}{h_1} \cdot \frac{dh_1}{dU},$$

where f_1 , h_1 are the functions evaluated at the shock front ($\xi = 1$). They are time-dependent functions.

The first assumption is made because the numerical solutions of other studies [8, 23] show that the velocity functions are nearly linear², while the second assumption is based on a quasi-similarity theory [12].

From equations (59) and (60), combined with the assumptions above, g and h are readily obtained as follow:

$$g = A \left(\xi^{m+2} - 1 \right) + g_1 \quad (61)$$

and

$$h = h_1 \xi^m,$$

where $g_1 = g(1, t)$ and A , m are functions of f_1 , g_1 , h_1 , and λ .

In terms of physical quantities, the solutions are

$$u = u_1 r/R,$$

$$\rho = \rho_1 (r/R)^m,$$

$$P = \rho_0 U^2 A \left[\left(\frac{r}{R} \right)^{m+2} - 1 \right],$$

where

$$m = \frac{3u_1/U + \lambda U/\rho_1 \cdot \frac{\rho}{\partial U}}{(u_1 - U)/U}$$

and

$$A = \frac{\rho_1}{\rho_0} \left[\frac{u_1}{U_2} (u_1 - U) + \frac{\lambda u_1}{U} + U \frac{\partial(u_1/U)}{\partial U} \right] / (m+2).$$

The subscript 1 denotes the Hugoniot flow quantities.

NUMERICAL RESULTS AND DISCUSSION

In this section, some numerical results are presented. Based on these results, discussions are given on the theoretical model proposed in this study. Since some of the assumptions imposed in this model are subject to a certain degree of uncertainty, it is necessary to compare the present results carefully with numerical data available from other studies. Because of the complexity inherent in this problem, it is believed that the justification of some of the assumptions is possible only through comparison.

The Starting Point of Shock Curvature

In Whitham's rule, the effect of disturbances behind the shock wave is ignored. The justification of this model is difficult to establish, because the information on the flow field behind the shock wave is still meager.

Point A in Figure 16a represents the location where the shock curvature starts. By the CCW approximation, the following is obtained:

$$\tan m_0 = \mu(U_0) \quad (62)$$

2. The first assumption was also made by Rayzer [24] and Sakura [12], but no basic reasons were given.

But M_0 can also be predicted by the following alternative equation:

$$\tan m_0 = \frac{u}{U} \left[1 - \left(\frac{U-u}{a} \right)^2 \right]^{\frac{1}{2}} \quad (63)$$

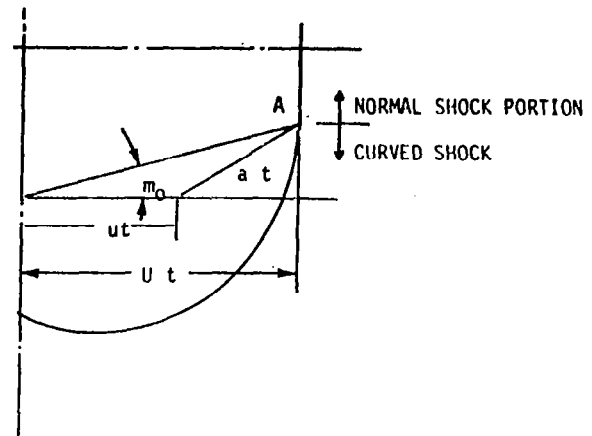
Equation (63) was derived by Skew [25] and also by Heyda [26] to indicate the point at which the normal shock wave is first reached by the rarefaction wave from a turning corner. It must be pointed out that equation (63) is only an approximation because the shock wave is not uniform and the velocity u and sound velocity a depend on the locations.

A comparison of the above two approximations is shown in Figure 16b. For high impact velocities, the discrepancy between these two predictions is small, but a large discrepancy exists in the low velocity region. Skew [25] performed an experiment for shock waves diffracting around a corner. Observation of the shock shape favors the prediction of equation (63). This may imply that the CCW approximation only works for high impact velocities. However, this is not a definite conclusion since the phenomenon of impact-generated shock waves may be different from Skew's experiments.

The Successive Positions of Shock Profiles

A numerical example of aluminum impact on aluminum at a velocity of 20 km/sec is presented in Figure 17 such that the positions of shock profiles are functions of successive time steps. The normal shock portion vanishes very rapidly, and it completely disappears at about $5.5 \mu\text{sec}$. The shock profile develops further into an ellipsoid and eventually approaches a hemispherical shape.

The appearance of hemispherical shock shape inspires the assumption of spherical symmetry made by many investigators (7). This assumption is reasonable only if, after a long period of time, the shock strength has attenuated considerably and degenerated into the speed of sound. Soon after impact, the shock shape is far from spherical in shape and, most important, the flow properties vary along the shock front. The pressure distribution, for instance, has the highest value at the symmetric axis and decreases in value toward the target free surface.



(a)

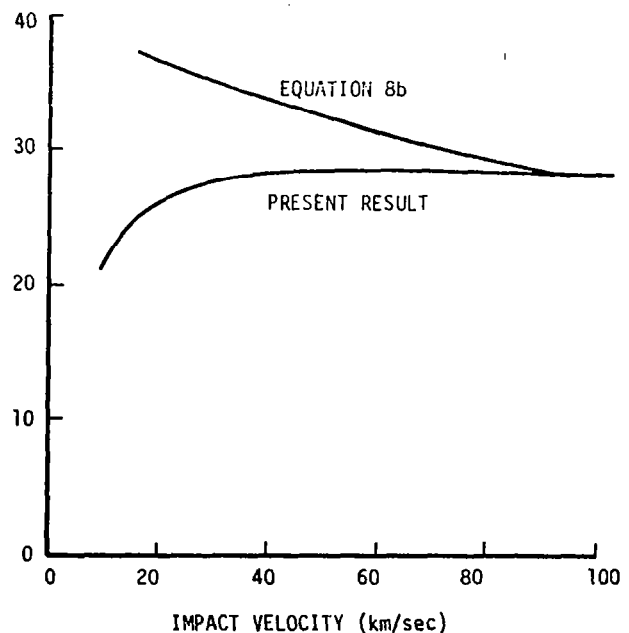


Figure 16. The starting point of shock curvature in aluminum.

Pressure Distributions

A comparison is made with the numerical results obtained by Heyda and Riney [27] concerning the peak pressure along the axis of cylindrical symmetry. Figure 18 shows that for $(z/d) < 1$, the pressure is equal to Hugoniot pressure obtained by the normal shock relation since the plane shock generated at the

interface has not been attenuated by the rarefaction waves from the corner. The pressure then decreases drastically as the shock wave advances into the target. The discrepancy of these two results at the early stage is mainly a result of the numerical diffusion effect inherent in the direct numerical scheme. Errors of about 30 percent occur compared with the exact solutions. However, the agreement in general is good except the late stage in which the present solution is consistently higher than the direct numerical solutions. This is believed to be caused

by the fact that the rarefaction waves reflected from the rear surface of the projectile are not considered. Such rarefaction waves are known to attenuate the target shock strength [18].

The angular distributions of shock pressure are shown in Figure 19 so that the pressure gradients in the φ direction are indeed small for large elapsed time. This phenomenon provides the basis of formulating the quasi-similarity solutions in the previous section.

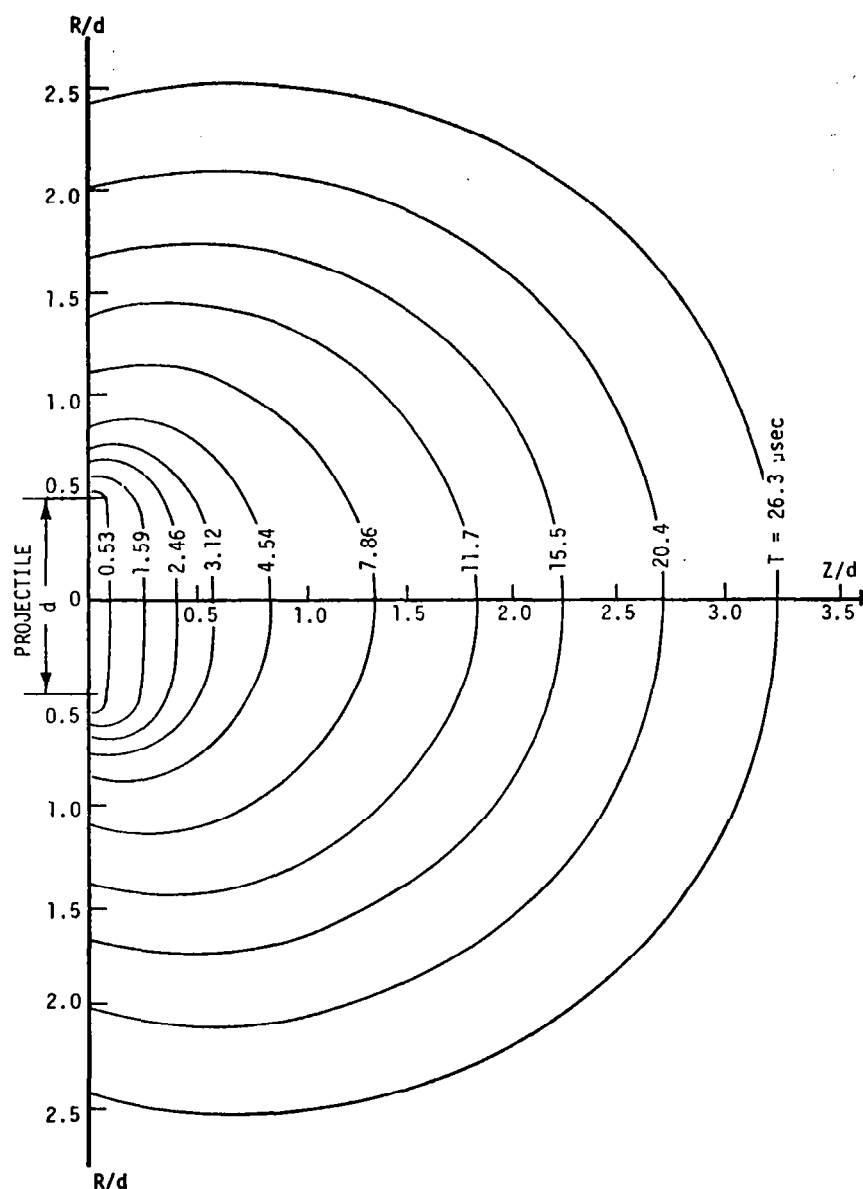


Figure 17. Numerical example of aluminum impact on aluminum at a velocity of 20 km/sec.

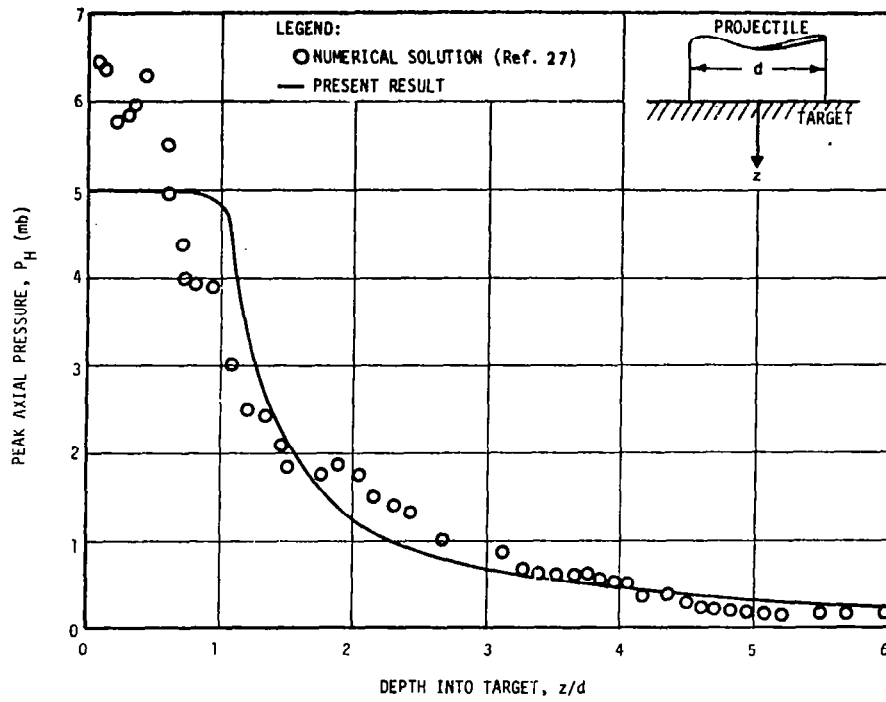


Figure 18. Comparison of peak pressure distribution for an aluminum-on-aluminum impact (impact velocity is 20 km/sec).

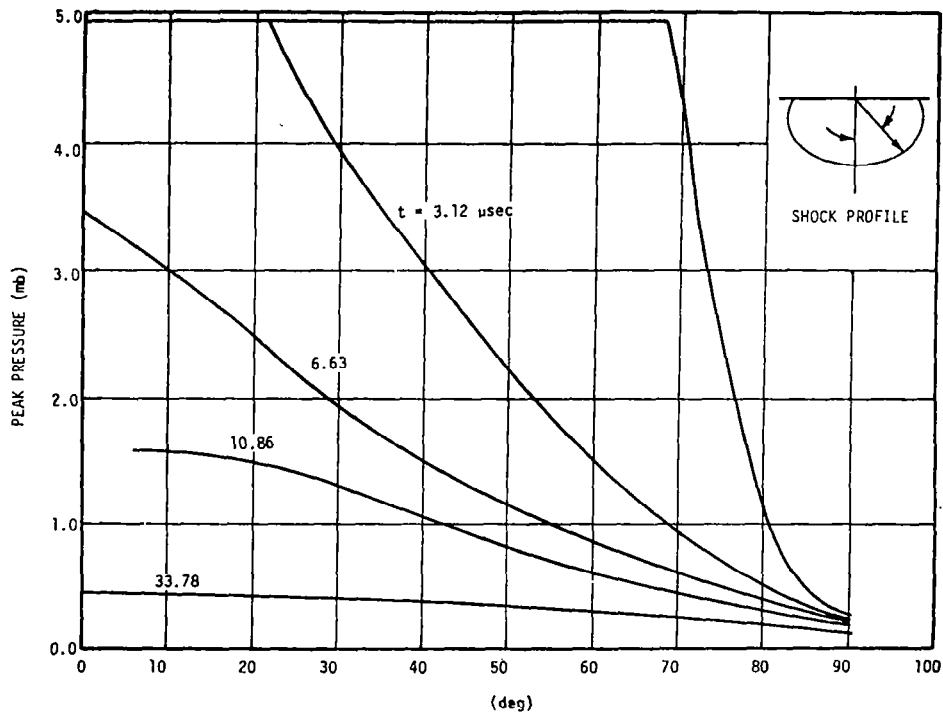


Figure 19. Angular pressure distribution.

APPENDIX: SOUND SPEED OF c, s MATERIAL BEHIND THE SHOCK

The Mie-Grüneisen equation of state is

$$p - p_0 = \rho \Gamma(\rho) (e - e_0), \quad (A-1)$$

where the subscript 0 denotes the initial state and $\Gamma(\rho)$, the Grüneisen ratio, is a function only of density. Differentiating equation (A-1) with respect to e at constant ρ , the following expression for $\Gamma(\rho)$ in terms of thermodynamic quantities is obtained:

$$\Gamma = \frac{1}{\rho} \left(\frac{\partial p}{\partial e} \right)_\rho \equiv \frac{1}{\rho C_v} \left(\frac{\partial p}{\partial T} \right)_\rho. \quad (A-2)$$

According to Reference 7, $\Gamma \approx 2s - 1$ at normal density, or pressure $p = 0$. But for higher pressure, a constant value of Γ was proposed by Rao [7], who matched the Mie-Grüneisen equation of state with the Rankine-Hugoniot relation of c , s material at very high shock strength. It is

$$\Gamma = 2(s - 1). \quad (A-3)$$

It should be pointed out here that the range of validity of this expression of Γ is uncertain since there is no way to justify it by means of the available experimental data of metals. In spite of this, equation (A-3) is used in this work for the sake of convenience.

Now, a thermodynamic relation can be derived to yield the adiabatic sound speed a as a function of dilatational wave speed c and the material parameter s . The derivation presented here is based on Reference 28. To do this, the Rankine-Hugoniot equation is differentiated first as follows:

$$de = \frac{1}{2} \left[\left(\frac{1}{\rho_0} - \frac{1}{\rho} \right) dp - (p + p_0) d\left(\frac{1}{\rho}\right) \right]. \quad (A-4)$$

Combined with the second law of thermodynamics, equation (A-4) becomes

$$T ds = de + pd\left(\frac{1}{\rho}\right) = \frac{1}{2} \left[\left(\frac{1}{\rho_0} - \frac{1}{\rho} \right) dp - (p + p_0) d\left(\frac{1}{\rho}\right) \right] + p d\left(\frac{1}{\rho}\right). \quad (A-5)$$

A general expression of the equation of state may be written

$$p = p(\rho, S);$$

hence,

$$dp = \left(\frac{\partial p}{\partial \rho} \right)_S d\rho + \left(\frac{\partial p}{\partial S} \right)_\rho dS, \quad (A-6)$$

where $\left(\frac{\partial p}{\partial \rho} \right)_S = a$ is the adiabatic sound speed, and

$$\left(\frac{\partial p}{\partial S} \right)_\rho \equiv \left(\frac{\partial p}{\partial T} \right)_\rho \left(\frac{\partial T}{\partial S} \right)_\rho = \frac{T}{C_v} \left(\frac{\partial p}{\partial T} \right)_\rho \quad (A-7)$$

Substituting equation (A-3) into equation (A-7) yields

$$\left(\frac{\partial p}{\partial S} \right)_\rho = \rho T \Gamma. \quad (A-8)$$

Then equation (A-6) can be written as

$$dp = a^2 d\rho + \rho \Gamma T dS. \quad (A-9)$$

Eliminating the term $T dS$ from equations (A-5) and (A-9) gives a relation between the adiabatic sound speed, a^2 , and the slope of the Rankine-Hugoniot curve in (p, ρ) plane, c^2_{R-H} , which is

$$c^2_{R-H} \equiv \frac{dp}{d\rho} = \frac{a^2 - (p - p_0)/2\rho}{1 - \rho \left(\frac{1}{\rho_0} \right) - \left(\frac{1}{\rho} \right)/2}$$

or

$$a^2 = c^2_{R-H} \left[1 - \frac{\Gamma}{2} \left(\frac{\rho}{\rho_0} - 1 \right) \right] + \frac{\Gamma}{2} \left(\frac{\rho}{\rho_0 C_v} \right) \left(\frac{\rho_0}{\rho} \right) c^2. \quad (A-10)$$

The shock relations of c , s materials can be expressed as follows:

$$U = c + sU,$$

$$\frac{\rho_1}{\rho_0} = \frac{sM}{1 + (s-1)M}, \quad (A-11)$$

$$\frac{\rho_1}{\rho_0 c^2} = \frac{M(M-1)}{s},$$

and

$$c_{R-H}^2 = \frac{dp}{d\rho} = \frac{dP/c/M}{d\rho/c/M}$$

$$= \frac{c^2}{s^2} (2M-1) [1 + (s-1)M]^2,$$

where $M = U/c$.

Substituting equation (A-11) in equation (A-10) yields

$$a = \frac{c}{s} [(3s-1)(s-1)M^2 - (2s^2-6s+2)M - (2s-1)]^{\frac{1}{2}} \quad (A-12)$$

and

$$\frac{a}{c_{R-H}} = \left[\frac{(3s-1)M - (2s-1)}{(2M-1) \cdot 1 + (s-1)M} \right]^{\frac{1}{2}} \quad (A-13)$$

The ratio of a/c_{R-H} depends upon s and M only.

REFERENCES

1. Bjork, R. L.: Effect of a Meteoroid Impact on Steel and Aluminum in Space. The Rand Corporation, P-1662, December 1958.
2. Walsh, J. M.; and Tillotson, J. H.: Hydrodynamics of Hypervelocity Impact. General Dynamics, General Atomic Division GA-3827, 1961.
3. Riney, T. D.: Depth of Penetration of Hypervelocity Projectiles. AIAA Journal, vol. 3, 1965, pp. 52-60.
4. Johnson, W. E.: OIL-A Continuous Two-Dimensional Eulerian Hydrodynamic Code. General Dynamics Corporation, General Atomic Division, GAMD-5580, Revised January 1965.
5. Young, C. T. K.; and Cronkrite, H. L.: A Particle-in-Cell Program for the Calculation of the Phenomena of Hypervelocity Impacts. Brown Engineering Company, Inc., Technical Note AST-282, 1968.
6. Kreyenhagen, K. N.; Wagner, M. H.; and Bjork, R. L.: Ballistic Limit Determination in Impacts on Multi-Material Laminated Targets. AIAA Journal, Paper no. 69-356, 1968.
7. Rae, N. J.: Analytic Studies of Impact-Generated Shock Propagation - Survey and New Results. Cornell Aeronautical Laboratory, Report no. AL-2456-A-1, June 1968.
8. Bach, G. G.; and Lee, J. H.: Shock Propagation in Solid Media. AIAA Journal, Paper no. 67-141, 1967.
9. Zeldovich, Y. B.: Motion of a Gas Due to a Pressure of Short Duration (Shock). Akustichsky Zhurnal, vol. 2, 1956, Translation in Soviet Physics-Acoustics, vol. 2, 1956.
10. Skews, B. W.: Profiles of Diffracting Shock Waves: An Analysis Based on Whitham's Theory. University of Wetwatersrand, 1966.
11. Hayes, W. D.: The Propagation Upward of the Shock Wave from A Strong Explosion in the Atmosphere. Journal of Fluid Mechanics, vol. 32, part 2, 1968, pp. 317-331.
12. Sakura, A.: The Blast Wave Theory in Basic Development in Fluid Mechanics. Ed. by H. Holt, Academic Press, New York, N. Y., 1965.
13. Whitham, G. B.: A New Approach to Problems of Shock Dynamics, Part I - Two-Dimensional Problems. Journal of Fluid Mechanics, vol. 2, 1957, pp. 145-171.

REFERENCES (Concluded)

14. Shapiro, A. H.: The Dynamics of Thermodynamics of Compressible Fluid Flow. Volumes I and II, Ronald Press Company, New York, N. Y., 1953.
15. Tillotson, J. H.: Metallic Equations of State for Hypervelocity Impact. General Atomic, GA-3246, July 1962.
16. McQueen, R. G.; and March, S. P.: Equation of State for Nineteen Metallic Elements From Shock-Wave Measurements to Two Megabars. Journal of Applied Physics, vol. 31, no. 7, July 1960.
17. Rice, M. H.; McQueen, R. G.; and Walsh, J. M.: Compression of Solid by Strong Shock Waves. Sietz and Turnbull Series, vol. 6, Solid State Physics, Academic Press, 1958.
18. Chou, P. C.; and Allison, F. E.: Strong Plane Shock Produced by Hypervelocity Impact and Late-Stage Equivalence. Journal of Applied Physics, vol. 37, 1966, pp. 853-860.
19. Chester, W.: The Quasi-Cylindrical Shock Tube. Phil. Mag., vol. 7, no. 45, 1954, pp. 1293-1301.
20. Chisnell, R. F.: The Normal Motion of a Shock Wave Through a Non-Uniform One-Dimensional Medium. Proc. Roy. Soc., A-232, 1955, pp. 350-370.
21. Whitham, G. B.: On the Propagation of Shock Wave Through Regions of Non-Uniform Area on Flow. Journal of Fluid Mechanics, vol. 4, 1958, pp. 337-360.
22. Collin, R.; and Holt, M.: Intense Explosions at the Ocean Surface. Physics of Fluid, vol. 11, 1968, pp. 701-713.
23. Walsh, J. M.; Johnson, W. E.; Dienes, J. K.; Tillotson, J. H.; and Yates, D. R.: Summary Report on the Theory of Hypervelocity Impact. The Fluid Dynamic Aspect of Space Flight, Gordon and Breach Science Publishers, 1964.
24. Rayzer, Yu, P.: Motion of a Gas under the Influence of a Point-Impact Shock on its Surface (an Explosion on a Surface). Zhurnal Prikladnoi Mekhanki i Tekhnichiski Fiziki, no. 1, 1963, pp. 57-66. Translation by M. J. Nowak, Available at General Atomic Division, General Dynamics Corp., Report no. GA-TR-5081, May 1964.
25. Skews, B. W.: The Shape of a Diffracting Shock Wave. Journal of Fluid Mechanics, vol. 29, 1967, pp. 297-304.
26. Heyda, J. F.; and Riney, T. D.: Penetration of Structures by Hypervelocity Projectiles. General Electric Company, Space Sciences Laboratory, Report no. R64SD3, February 1964.
27. Riney, T. D.; and Heyda, J. F.: Theoretical Prediction of Crater Size for Hypervelocity Impact by Reduced-Density Particles. General Electric Company, Final Report under Contract NADA 3-5812.
28. Duvall, G. E.: Concepts of Shock Wave Propagation. Bulletin of the Seismological Society of America, vol. 52, no. 4, October 1962, pp. 869-893.

N70-35511

ONE-DIMENSIONAL MODEL FOR INVESTIGATION OF CHANGES IN CONDUCTIVITY OF DIELECTRICS UNDER SHOCK CONDITIONS

By

E. E. Klingman

ABSTRACT

A one-dimensional model is used to investigate changes in conductivity of dielectrics under extreme shock conditions. The dielectric is forced into metallic conduction states by varying the energy band structure as a function of lattice parameter. The most striking feature of the treatment is its generality, deriving from the fact that materials in which repulsive forces predominate can be described in much the same way. This is in contrast to the various bonds that must be considered when attractive forces are most important. Although the model is qualitatively successful, it is concluded that a nonlinear treatment is necessary to obtain quantitative results.

INTRODUCTION

The Pegasus Meteoroid Detection Satellites use large surface area capacitors as detection devices. A meteoroid-hit upon one of the capacitors results in a current pulse that furnishes information to the telemetry system. The mechanism producing the pulse may be one of the following:

- Penetration and physical shorting of capacitors
- Plasma generation
- Dielectric shocked into conduction

When this study was begun, the possibility of the last mechanism was uncertain. The object of the study was to investigate the possibility of dielectrics being shocked into conduction and, if possible, to relate the pulse duration to meteor velocity.

Experimental data [1, 2] were found that established beyond doubt the possibility of forcing insulators into conduction states. The application of sufficiently high pressures to a variety of insulators resulted in conductivities that approximated those of metals. The study then centered on finding a suitable model for calculations. This model would then be used to investigate velocity effects.

MODEL FOR CALCULATIONS

The situation, even in the best of crystal structures, is formidable from the viewpoint of realistic calculations. It was quickly decided that any attempt to analyze the actual dielectric, Mylar, would soon bog down in complexity. In view of the time available for this study, a one-dimensional model was chosen with the hope of obtaining qualitative information that could be correlated with data from the satellites, and experiments already performed on the ground. Although symmetry plays a vital role in crystal calculations, the added complexity was of questionable value because of the unknown effects on the symmetry of the high temperature and pressures involved during collision.

The differences in conductivity of metals and insulators vary over an extremely large range (on the order of 10^{42}). This variation can only be accounted for in terms of the structures of energy bands. The simplest model resulting in band structure is the Kronig-Penny model [3], but this model was found inadequate for pressure calculations. Since pressures of 1 Mb compress condensed systems by a factor of 2 [1], the parameter to be varied with increasing pressure is the lattice constant α . The increase in temperature is taken into account through an approximation that will be explained later.

Conditions are such in the case of extreme shock that considerations normally of importance must be evaluated. Of critical importance in crystal calculations at normal pressures and temperatures is the type of crystal involved; i.e., ionic, molecular, covalent, metallic. The type of crystal is determined by the nature of the attractive forces causing the atom to crystallize. In shocked materials, however, energy exceeds the attractive energy, and the repulsive potential between the atoms predominantly determines the properties of the system. Empirical results from shock data indicate that at milder conditions than expected, it is permissible to neglect the details of binding of a substance [4]. This could have been predicted from the success of the Fermi-Dirac model which ignores band structure and statistically groups atoms about the nucleus. When shock and heat energies approach the chemical binding energies, this model becomes applicable since at that point all materials become close-packed and metallic.

At this point a digression may be in order concerning the difference in metals and insulators from an energy band standpoint.

Bands arise from the fact that no two particles obeying Fermi statistics can be in the same quantum state in a given system. Consider, for example, three atoms in their ground or lowest energy state. Quantum mechanics predicts for each isolated atom a set of energy states that are identical to those of any similar isolated atom. The situation changes when these isolated atoms are brought together to form a system. As the wave functions overlap and interact, the states are shifted to avoid violating the Pauli exclusion principle. The group of states that were identical for similar isolated atoms now form a band. This is shown in Figure 1 for six atoms.

In a crystal with very large numbers (10^{23}) of atoms, the levels are so closely spaced inside a band that the band can be considered continuous for all practical purposes.

A crystal composed of N atoms is presented in Figure 2. The particular atom chosen has two electrons in the first energy state and one electron in the second state. The lowest energy band will have N states, each of which will be occupied by two electrons with opposite spins. The opposite spins prevent electrons with the same energy from having identical quantum numbers, thereby violating the Pauli exclusion principle. The $2N$ electrons fill the first band to capacity. The next band, with only N

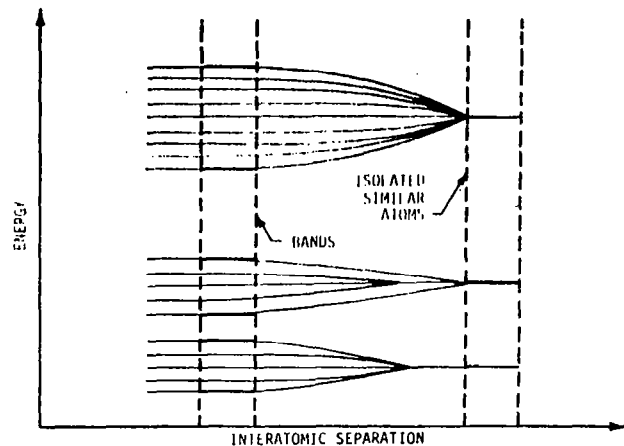


Figure 1. Formation of bands.

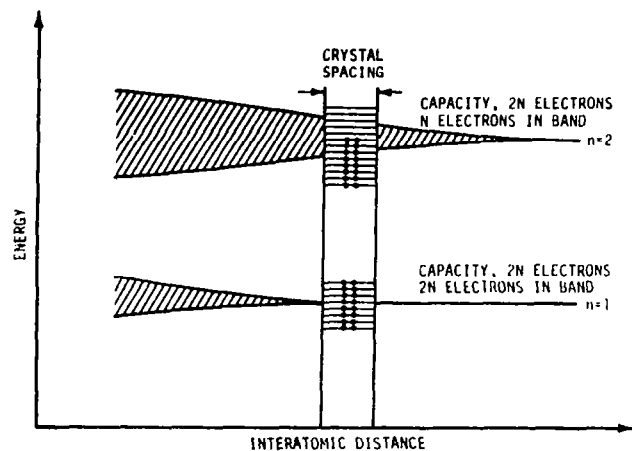


Figure 2. Energy bands for crystal with N atoms of $1s^2 2s^1$ configuration.

electrons and $2N$ available states, will be only half-filled. Electrons in this band can gain thermal energy and make transitions to higher states in the same band. If an electric field is applied to the crystal, conduction is possible in the half-filled band. No conduction is possible in the filled band.

If the atom chosen had been one with either two or zero electrons in the second energy state, then the $n = 2$ band would be either full or empty, respectively. In either case conduction would be impossible. Consider the case in which the $n = 2$ band is empty. If the forbidden gap was made small enough, some of the atoms in the $n = 1$ band might gain enough energy to jump into the empty band. The filled band is called the valence band, and the empty band is called the conduction band. When the gap is

small enough, some conduction occurs. By decreasing still further the gap between valence and conduction bands, the conductivity is increased. Finally, when the bands overlap (zero forbidden gap), the situation is again metallic as in the case when the band was half-filled. Figure 3 shows the four general cases.

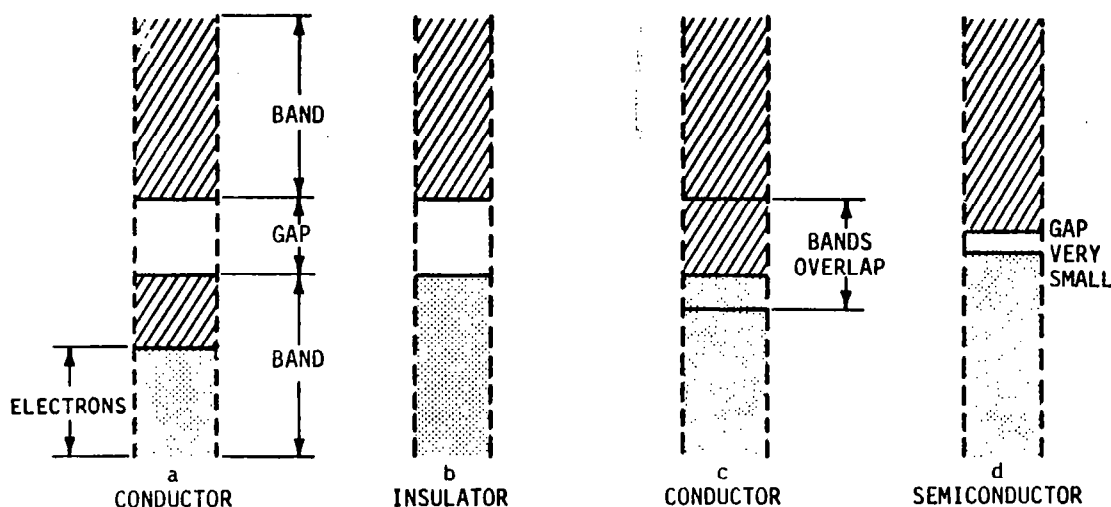


Figure 3. Four general types of band structure.

Any model chosen for calculations on conductivity should yield a band structure varying as a function of the parameters involved. This requirement rules out the Fermi-Dirac method, and as mentioned earlier, the Kronig-Penny Model is not convenient when lattice spacing is the parameter of interest. To retain the band structure, a periodic lattice must be used, and a sinusoidal potential with appropriate assumptions is chosen as the model for calculations. Because of the fact that symmetry is to be neglected and a general crystal will be used rather than an exact model of Mylar, a one-dimensional chain of atoms will be used for calculations. Such a model should qualitatively agree with a real crystal if the approximations made are reasonable.

Figure 4 is shown to emphasize that unlike a single atom (Fig. 3a), there are no free energies extending over all positive energy states. The free electrons in a crystal still have forbidden energy regions. This is perhaps best understood by remembering the wave nature of the electrons propagating through the periodic structure of the

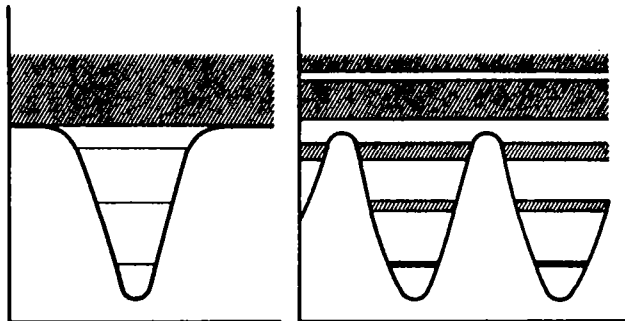


Figure 4. An illustration of the difference in discrete and continuous energies of single "atom" and continuous energy bands and forbidden energies of periodic potential.

The first potential chosen was the simplest one that would result in a lattice periodic in x with a as the period; i.e.,

$$V(x) = V_0(x) \cos \frac{2\pi x}{a} \quad (1)$$

Since the primary interest is in the effect of changes in α , it is desirable that the average value of energy change as a function of α . Otherwise, no change in the average energy of the energy bands will result. This is seen by averaging the potential over one cycle.

$$\langle V(\alpha) \rangle_{\text{avg}} = \frac{\int_0^\alpha V_0(\alpha) \cos \frac{2\pi x}{\alpha} dx}{\int_0^\alpha dx} = 0 \quad (2)$$

The result is seen to be independent of α . The situation remains unchanged for any multiplicative factor not a function of position, x . In order to obtain a potential whose average value depends on the parameter α , an additive term must be used. The new potential may be represented by

$$V(\alpha) = V_1(\alpha) + V_0(\alpha) \cos \frac{2\pi x}{\alpha} \quad (3)$$

with average value

$$\langle V(\alpha) \rangle_{\text{avg}} = \frac{\int_0^\alpha V_1(\alpha) dx}{\int_0^\alpha dx} = V_1(\alpha) \quad (4)$$

To find a general potential applicable to a wide variety of materials, an approximation must be made. For the present it is assumed that each atom in the crystal has one conduction electron. For alkali and monovalent metals, there is direct experimental evidence of this. The conduction electrons form a gas different from an ideal gas because of interactions with the lattice and with each other. These conduction electrons will be considered as relatively free electrons to the extent that the core can be considered as a separate entity with $Z-1$ electrons and Z protons in the nucleus. Gauss's theorem states that a spherical charge distribution as seen from outside the sphere can be considered to be concentrated at the center. This results in a charge $+Ze + (Z-1)(-e) = +e$ at the center of each atom. The model chosen to determine $V_1(\alpha)$ will consist of one atom surrounded by two singly charged positive ions (Fig. 5). The free electrons from the ions will be considered as uniformly smeared throughout the crystal. The method of treating electrons as moving freely through a periodic field has been criticized because it neglects collisions between electrons. The answer to this criticism is that a

metal, like any other solid, must be treated in quantum mechanics as a gigantic molecule subject to the exclusion principle as well as to other quantum mechanical laws.

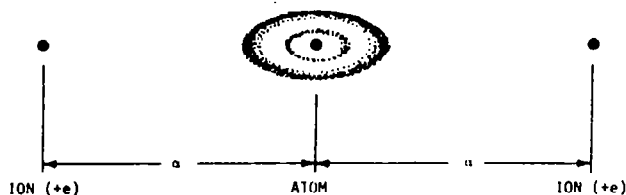


Figure 5. Model chosen to determine $V_1(\alpha)$.

The next step is to determine the potential energy resulting from this configuration. For continuous charge distribution the potential energy is described by [6]

$$V = \frac{1}{2} \iint \frac{\rho(\vec{x}) \rho(\vec{x}')}{|\vec{x} - \vec{x}'|} d^3x d^3x' \quad (5)$$

where ρ represents charge density. These densities are found by use of the quantum mechanical wave functions. If an atom is in state n , then $|\psi_n(\vec{r})|^2 d\tau$ is the probability that the valence electron is in the volume element $d\tau$ at the point (\vec{r}) . An equivalent statement is that $-e |\psi_n(\vec{r})|^2$ is the average charge density resulting from the valence electron at the point (\vec{r}) [7].

The actual wave functions for atoms have a number of nodes near the nucleus. For many problems, including this one, these nodes are unimportant and can be omitted with no loss of generality. Slater [8] has shown that the radial wave functions are given in the above approximation by

$$R_n(\vec{r}) = r^n e^{-k_n r} \quad ,$$

where

$$k_n = (Z-s)/n,$$

Z = atomic number,

s = Slater's Atomic Shielding Constant,

and

n = principal quantum number.

The complete wave function is a product of the radial wave function, the angular wave function, and a normalizing factor, $N_n(r)$, where ℓ and m are angular momentum quantum numbers. Spin is neglected.

$$\psi_n(\vec{r}) = N_n(r) R_n(\vec{r}) Y_\ell^m(\hat{r}) \quad (6)$$

The energy between the atom and one ion is first calculated. The situation is shown in Figure 6.

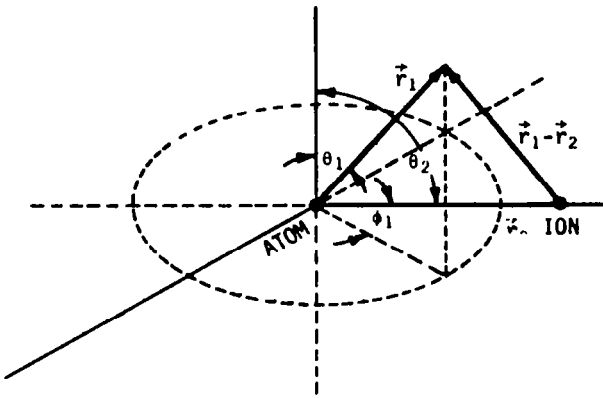


Figure 6. Coordinate system for ion-atom pairs.

For the coordinate system shown in Figure 6, the wave function for the ion is given by

$$\begin{aligned} \psi_I(\vec{r}_2) \\ = \frac{(4\pi)^{\frac{1}{2}}}{\alpha} \delta(\cos \theta_2) \delta(\phi_2) \delta(r_2 - \alpha) Y_0^0(\hat{r}_2) \quad (7) \end{aligned}$$

where $1/\alpha$ is the normalizing factor obtained from

$$\int_{\text{all space}} \psi_I^*(\vec{r}_2) \psi_I(\vec{r}_2) r_2^2 dr_2 d\Omega_2 = \alpha^2 \quad (8)$$

To obtain the normalizing factor for the atomic wave function, the same integral is evaluated as follows:

$$\begin{aligned} \int_{\text{all space}} \psi_n^*(\vec{r}_1) \psi_n(\vec{r}_1) d\vec{r}_1 \\ = \int_0^{2n} r_1^{2n} \exp(-2k_n r_1) r_1^2 dr_1 \int_{\Omega_1} Y_\ell^{*m}(\hat{r}_1) Y_\ell^m(\hat{r}_1) d\Omega_1 \quad (9) \end{aligned}$$

The angular integral is equal to $\delta_{\ell,\ell} \delta_{m,m}$ or unity and the radial integral evaluated at the limits gives the value

$$\int_{\text{all space}} \psi_n^*(\vec{r}_1) \psi_n(\vec{r}_1) d\vec{r}_1 = \frac{(2n+2)!}{(2k_n)^{2n+3}} = \frac{1}{N_n^2} \quad (10)$$

Thus the normalized atomic wave function is

$$\begin{aligned} \psi_n(\vec{r}_1) \\ = (2k_n)^{n+1} \left\{ \frac{2k_n}{[2(n+1)]!} \right\}^{\frac{1}{2}} r_1^n \exp(-k_n r_1) Y_\ell^m(\hat{r}_1) \quad (11) \end{aligned}$$

The values of k_n vary with Z and with the electron under consideration. A complete treatment of the atomic shielding coefficients is given by Slater [8]. Values predicted from these coefficients generally agree with experimental values within 10 percent, which is close enough for most qualitative predictions.

The wave functions derived satisfy the charge condition

$$\int_{\text{all space}} \rho d\tau = \pm e \quad \int \psi^* \psi d\tau = \pm e \quad (12)$$

The interaction term $1/|\vec{r}_2 - \vec{r}_1|$ can be expanded in spherical harmonics as follows [9]

$$\frac{1}{|\vec{r}_2 - \vec{r}_1|} = \sum_{\lambda=0}^{\infty} \sum_{m=-\lambda}^{+\lambda} \frac{4\pi}{2\lambda+1} \frac{r_<^\lambda}{r_>^{\lambda+1}} Y_\lambda^{*m}(\hat{r}_1) Y_\lambda^m(\hat{r}_2) \quad (13)$$

where $r_<(r_>)$ is the lesser (greater) of r_1 and r_2 . Equation (5) becomes

$$V = -\frac{e^2}{2} \int \frac{\psi_n^*(\vec{r}_1) \psi_n(\vec{r}_1) \psi_1^*(\vec{r}_2) \psi_1(\vec{r}_2)}{|\vec{r}_1 - \vec{r}_2|} d\vec{r}_1 d\vec{r}_2 \quad (14)$$

$$V = -\frac{e^2}{2} \sum_{\lambda=0}^{\infty} \sum_{m=-\lambda}^{\lambda} \left(\frac{4\pi}{\alpha} \right)^{\frac{\lambda}{2}} \left(\frac{1}{2\lambda+1} \right) \frac{(2k)^{3\lambda+2}}{(2n+2)!} \\ \times \int_0^{\infty} r_1^2 dr_1 \int_0^{\infty} r_2^2 dr_2 \delta(r_2 - r_1) r_1^{2n} \exp(-2k_n r_1) \frac{r_1^{\lambda}}{r_1^{\lambda+1}} \\ \times \int_{\Omega_1} \int_{\Omega_2} Y_{\lambda}^m(\hat{r}_2) \delta(\cos \theta_2) \delta(\phi_2) Y_{\lambda}^m(\hat{r}_1) Y_{\lambda}^{m_{\lambda}}(\hat{r}_1) Y_{\lambda}^{m_{\lambda}}(\hat{r}_1) Y_{\lambda}^{m_{\lambda}}(\hat{r}_1) d\Omega_1 d\Omega_2 \quad (15)$$

The upper limit on the integration in the atomic wave function space was chosen to be the lattice parameter α . This is obviously a maximum. Later this may be decreased to some optimum value. The angular integral after integration over Ω_2 becomes

$$\text{Angular Integral} \\ = \left[\frac{1}{4\pi} Y_{\lambda}^{m_{\lambda}}(\cos \theta_2 = 0, \phi_2 = 0) \right] \\ \times \left[\int_{\Omega_1} Y_{\lambda}^{m_{\lambda}}(\hat{r}_1) Y_{\ell}^m(\hat{r}_1) Y_{\ell}^m(\hat{r}_1) d\Omega_1 \right] \quad (16)$$

Expressing the Ω_1 integral in terms of Clebsch-Jordan coefficients, the complete angular integral becomes

$$\text{Angular Integral} \\ = \left\{ \frac{1}{4\pi} Y_{\lambda}^{m_{\lambda}}(\cos \theta_2 = 0, \phi_2 = 0) \frac{2\ell+1}{[4\pi(2\lambda+1)]^{\frac{1}{2}}} \right\} \\ \times C(\ell, \ell, \lambda; m, m, m_{\lambda}) C(\ell, \ell, \lambda; 000) \quad (17)$$

In order not to consider Clebsch-Jordan coefficients for which $Y_{\lambda}^{m_{\lambda}}$ vanishes, Table 1 was set up for values up to $n=3$. From Table 1 it is seen that only Y_0^0 , Y_2^0 and Y_2^2 contribute to the angular integral for values of n up to $n=3$. To evaluate the Clebsch-Jordan coefficients, a specific value of n is chosen. Choose first $n=1$. Obviously $\ell=0$ and $m=0$, and the Clebsch-Jordan coefficient is $C(00\lambda; 00m_{\lambda}) C(00\lambda; 000)$ from which $\lambda=0$, $m_{\lambda}=0$, and the term considered is unity. For $n=2$, the same situation applies because as is seen from Table 1, the values for $\lambda=1$ are multiplied by a zero term. For $n=3$, the same holds

for $\lambda=0$ and $\lambda=1$. For $\lambda=2$, another possibility presents itself. However, for the moment, the model will be restricted to 8 angular momentum states ($1=0$). The general expression is

$$V = -\frac{e^2}{2} \sum_{\lambda=0}^{\infty} \sum_{m=-\lambda}^{\lambda} \frac{(4\pi)^{\frac{\lambda}{2}}}{(2n+2)!} \frac{2\ell+1}{(2\lambda+1)^{3/2}} \frac{1}{\alpha^{\lambda+1}} \left\{ \frac{-\exp(2k_n \alpha)}{(2k_n)^{\lambda}} \left[(2k_n \alpha)^{2n+2+\lambda} \right. \right. \\ \left. \left. + \dots + (2n+\lambda+2)! \right] - \frac{(2n+\lambda+2)!}{(2k_n)^{\lambda}} \right\} \\ \times C(\ell, \ell, \lambda; m m m_{\lambda}) C(\ell, \ell, \lambda; 000) Y_{\lambda}^{m_{\lambda}}(\cos \theta_2 = 0, \phi_2 = 0) \quad (18)$$

A sample term in which $n=2$, $\ell=0$, $m=0$, $\lambda=0$, and $m_{\lambda}=0$ is as follows

$$V_{n=2} = -\frac{e^2}{\alpha} \left\{ \frac{1}{2} - \frac{\exp(-2k_n \alpha)}{2(720)} \left[(2k_n \alpha)^6 + 6(2k_n \alpha)^5 + \dots + 720 \right] \right\} \quad (19)$$

The curves for $n=1, 2$, and 3 are shown in Figure 7. In interpreting the curves, it must be remembered that for extremely small values of α , the above model does not even approximately describe the situation. However, for the values of the lattice parameter that are of physical interest in this problem, it is hoped that the behavior is realistic. Since the situation is such that this energy opposes the binding energy of the electron, the sign is reversed when it is added in the equation. Except

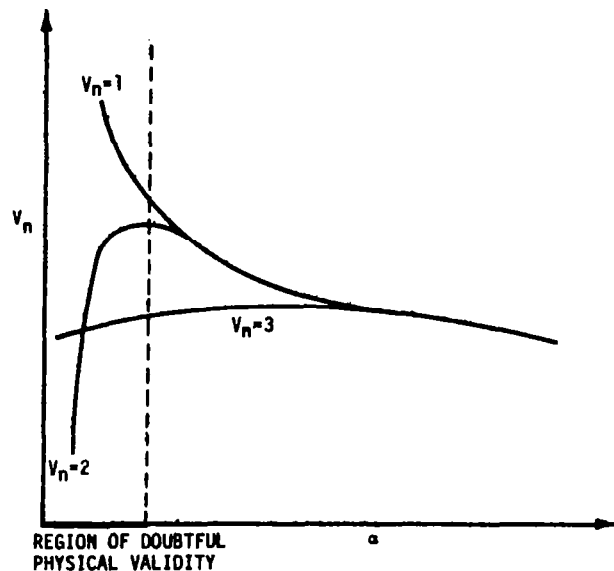


Figure 7. Additive energy as a function of lattice parameter.

TABLE 1. CLEBSCH-JORDAN COEFFICIENTS

F	λ	m_λ	\sum_{m_λ}	$Y_\lambda^{m_\lambda}\left(\frac{\pi}{2}, 0\right)$	$\sum_{m_\lambda} Y_\lambda^{m_\lambda}\left(\frac{\pi}{2}, 0\right)$
	0	0	1	$\frac{1}{(4\pi)^{\frac{1}{2}}}$	$\frac{1}{(4\pi)^{\frac{1}{2}}}$
	1	0	1	0	0
	1	± 1	0	$\mp \left(\frac{3}{8\pi}\right)^{\frac{1}{2}}$	0
	2	0	1	$-\frac{1}{2} \left(\frac{5}{4\pi}\right)^{\frac{1}{2}}$	$-\frac{1}{2} \left(\frac{5}{4\pi}\right)^{\frac{1}{2}}$
	2	± 1	0	0	0
	2	2	2	$\frac{1}{4} \left(\frac{15}{2\pi}\right)^{\frac{1}{2}}$	$\frac{1}{2} \left(\frac{15}{2\pi}\right)^{\frac{1}{2}}$

for extremely small (nonphysical) values of the lattice parameter, this model gives exactly the behavior that would tend to force the $n=2$ band and the $n=3$ band into conduction. The next step is to calculate the bands. This is done in the next section.

In quantum mechanical problems the energy is generally described by Schrödinger's equation,

$$\frac{\hbar^2}{2m} \nabla^2 \psi + V \psi = E \psi \quad (20)$$

Here V is the potential and E is the energy associated with the particle described by the wave function ψ . The classic case is, of course, the Coulomb field of the hydrogen atom. As mentioned earlier, however, the crystal under consideration can be regarded as a gigantic molecule to which the laws of quantum mechanics must apply. The change in Schrödinger's equation must occur in the potential V representing the periodic field of the crystal. For simplicity and for reasons already discussed, this will be considered one-dimensional. Thus

$$V = V_1(\alpha) + V_0(\alpha) \cos \frac{2\pi x}{\alpha} \quad (21)$$

The exact form of $V_0(\alpha)$ will be discussed later. Now Schrödinger's equation assumes the form

$$-\frac{\hbar^2}{2m} \nabla_x^2 \psi + \left[-V_1(\alpha) + V_0(\alpha) \cos \frac{2\pi x}{\alpha} \right] \psi = E \psi \quad (22)$$

This can be recognized as the Mathieu equation, which has been treated quite often in the literature [10]. The standard form of the Mathieu equation is as follows:

$$\frac{d^2 \psi}{dz^2} + \left(a - 2q \cos 2z \right) \psi = 0 \quad (23)$$

Letting $\pi x / \alpha = z$, equation (22) becomes

$$\frac{d^2 \psi}{dz^2} + \left[\frac{2m\alpha^2 [E - V_1(\alpha)]}{(\pi\hbar)^2} - \frac{2m\alpha^2 V_0(\alpha)}{(\pi\hbar)^2} \cos 2z \right] \psi = 0$$

This is in the standard form of the Mathieu equation when

$$a = \frac{2m\alpha^2 [E - V_1(\alpha)]}{(\pi\hbar)^2}, \quad q = \frac{m\alpha^2 V_0(\alpha)}{(\pi\hbar)^2} \quad (24)$$

The solutions to this eigenvalue equation yield the Mathieu functions of even and odd order and the characteristic or eigenvalues a . The Mathieu functions are of little interest in this problem. The eigenvalues a , however, yield the energy eigenvalues E for the electrons in the periodic potential. The equation at first glance appears rather simple, but the appearance is deceiving. Power series solutions yield eigenvalues in the form of infinite continued fractions. Various approximations are valid at the origin and in asymptotic regions. A polynomial in q was used for q very small until it was found that the expression was not valid over the range of q required by the physical problem. Rather than attempting to use different approximations in different regions, matching them where they overlapped, it was decided to make use of standard tables compiled by the National Bureau of Standards [11]. Although the tables are for a slightly different standard form of the Mathieu equation, they are easily convertible to the form of equation (23).

For purposes of calculation, the one-dimensional crystal is considered infinite in extent. Thus, boundary value aspects are avoided. One would naturally suppose that eigenvalue solutions for a periodic potential neglecting boundary conditions would be independent of position x . This is the case, and it results that the n th eigenvalue a_n is solely a function of q (which is in turn independent of x) from equation (24).

$$E_n = \frac{(\pi\kappa)^2}{2m\alpha^2} a_n + V_1(\alpha) = V_1(\alpha) + C(\alpha) a_n [q(\alpha)] \quad (25)$$

$$q(\alpha) = \frac{m\alpha^2}{(\pi\kappa)^2} V_0(\alpha)$$

As is readily seen from equation (25), much of the problem hinges upon the choice of $V_0(\alpha)$. Slater [12] has chosen an α^2 dependence for V_0 . This is shown in Figure 8 when it is seen that the barrier height varies as α^2 . This representation makes use of parabolic potentials that are quite often used as approximations in physics. At low pressures this is probably a good approximation; however, at high pressures (small α) this seems not to fit the case. Rather than a parabolic well, the actual case is that the potential goes toward minus infinity at each nucleus. The potential for a single nucleus is shown in Figure 9 [7]. By superimposing potentials of the kind shown in Figure 9, a new dependence on α arises. This is illustrated in Figure 10.

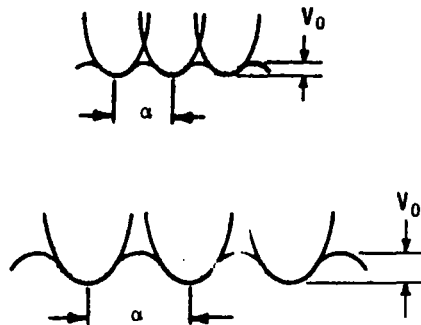


Figure 8. Slater representation of crystal potential.

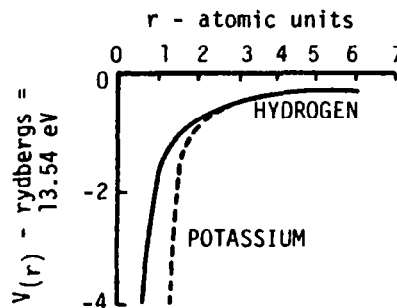


Figure 9. Potential energy of electron in hydrogen and alkali atoms.

It is shown from Figure 10 (and other combinations) that to a first approximation

$$|\alpha| |V_0| = \text{constant} \approx 35 \quad ; \quad (26)$$

therefore

$$V_0(\alpha) \approx \frac{35}{\alpha}$$

This will be the potential used for the change in potential resulting from a change in lattice parameter.

There is another factor entering into the change of potential with lattice parameter. This is the factor of ionization. As more and more energy is imparted to each atom (as signified by a decrease in α and a corresponding rise in temperature), the atoms lose their most energetic electrons and become ionized. The ultimate case is, of course, a plasma, but intermediate cases need to be taken into consideration. Ionization in this case must be treated statistically because of the complexity of the situation. The first factor introduced to take into account the ionization is the simplest possible factor

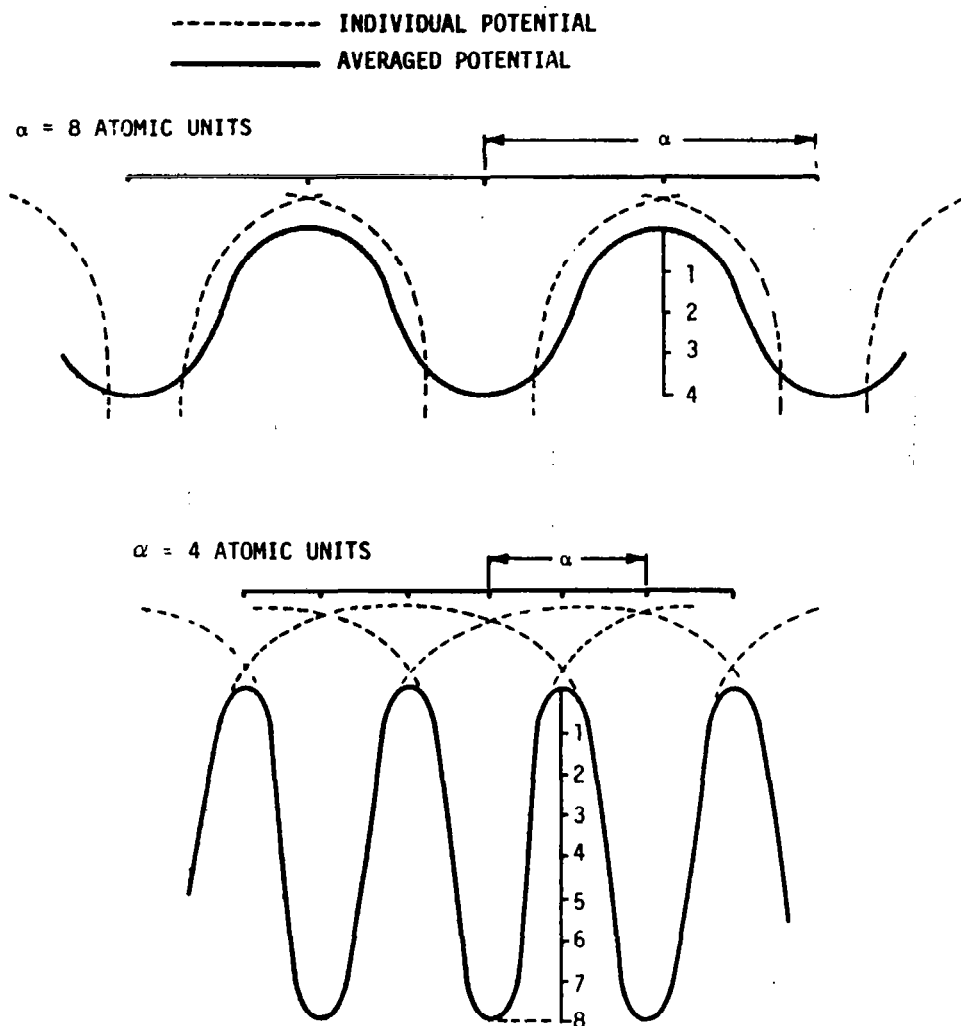


Figure 10. Variation of potential as a function of lattice parameter.

that will produce the correct action. An optimum value of the lattice parameter is chosen to be α_0 , and the ratio of α_0 to the lattice parameter is used as a measure of ionization. The ratio is cubed for more reasonable results.

$$\text{Ionization factor} = \left(\frac{\alpha_0}{\alpha} \right)^3 \quad (27)$$

For example, let sulphur have $\alpha_0 = 5.0$ angstroms. Thus for $\alpha = 5.0$ the ionization factor is unity. For $\alpha \approx 2.0$ angstroms, the ionization factor is approximately 16.0. For very small values of α , the ionization factor obviously becomes too great. It has already been mentioned, however, that at these

values the additive potential is also inaccurate. Conduction occurs before these values are reached, so the model need not be accurate to the same degree for very small lattice parameters. One further desirable feature of the above ionization factor is that at large values of the lattice parameter, the factor contributes a sort of shielding that is expected in such a circumstance. As the atoms separate, they gradually lose even their singly ionized character so that they would be better described as a Van der Waal's gas. This situation does not arise in the problem under consideration, but it is helpful to know that the ionization factor chosen works not only in a specific area, but also over a range of α 's. At this stage then, it is seen that the potential V_0 is described by

$$V_0(\alpha) \cong \frac{35}{\alpha} \left(\frac{\alpha_0}{\alpha} \right)^3 \quad (28)$$

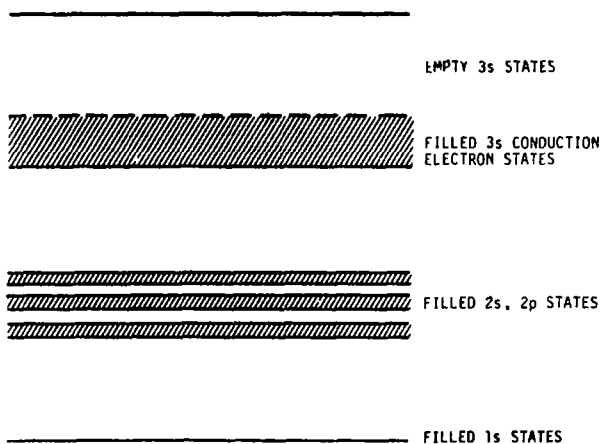
or

$$q \cong \frac{35 m \alpha_0^3}{(\pi \hbar)^2 \alpha^2} \quad (29)$$

As can be seen in Figure 9, the width of the bands is related to the principal quantum number n . (It should be realized that this quantum number, although referring to levels resulting from a central potential, has meaning when thought of in terms of the limiting states in the limit in which the crystal expands into isolated atoms.) The widths are obtained in the model by using ionization factors similar to equation (27) with n -dependent exponents (and, of course, radii). Thus,

$$n\text{-band ionization factor} = \left(\frac{\alpha}{\alpha_n} \right)^{f(n)} \quad (30)$$

At present the exponent $f(n)$ is determined empirically, although a theoretical basis is being considered (Fig. 11). A further approximation is made for the energy bands as expressed in equation (24). The parameter α is set equal to α_0 .

Figure 11. Illustrating n -dependence of bandwidth.

$$E_n = \frac{(\pi \hbar)^2}{2m\alpha_0^2} a_n^2 - V_1(\alpha) \quad (31)$$

This does not affect the point where energy bands intersect. It does slightly affect the shape of the curves in these regions. The approximation is

being studied in order to give a better explanation or a better approximation. Using for the above approximations $f(1) = 10$, $f(2) = 6$, $f(3) = 2$, $\alpha_1 = 1.6$, $\alpha_2 = 2.2$, $\alpha_3 = 5.0$, and $\alpha_0 = 5.0$, the energy band diagram is shown in Figure 12. The band structure changes with lattice parameter so that the solid goes into conduction for small enough parameters (high pressures). Using the scheme of Figure 3, the information in Figure 12 can be presented in a form comparable to snapshots of the energy bands for a given value of the lattice parameter. This is shown in Figure 13.

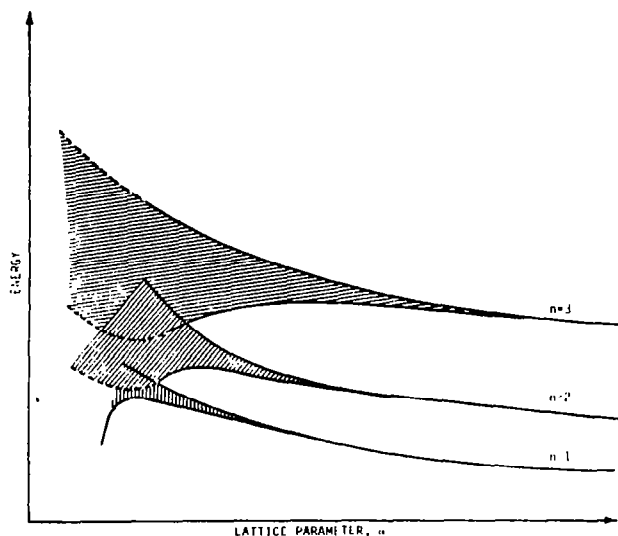


Figure 12. Energy band structure for model used.

The choice of ionization factor used in the previous calculations was made on the basis of simplicity and convenience while possessing a reasonably accurate dependence on lattice parameter. An attempt will be made here to better this first approximation. A caloric equation of state similar to that of water will be used. Water, which is the most important medium with approximately separable energy has an equation of state somewhat resembling a perfect gas [13]

$$p = A \left(\frac{\rho}{\rho_0} \right)^\gamma - B \quad (32)$$

where A , B , and γ are practically independent of entropy. This fact assures that by neglecting entropy changes, no great error will be introduced into the ionization factor. For reference purposes

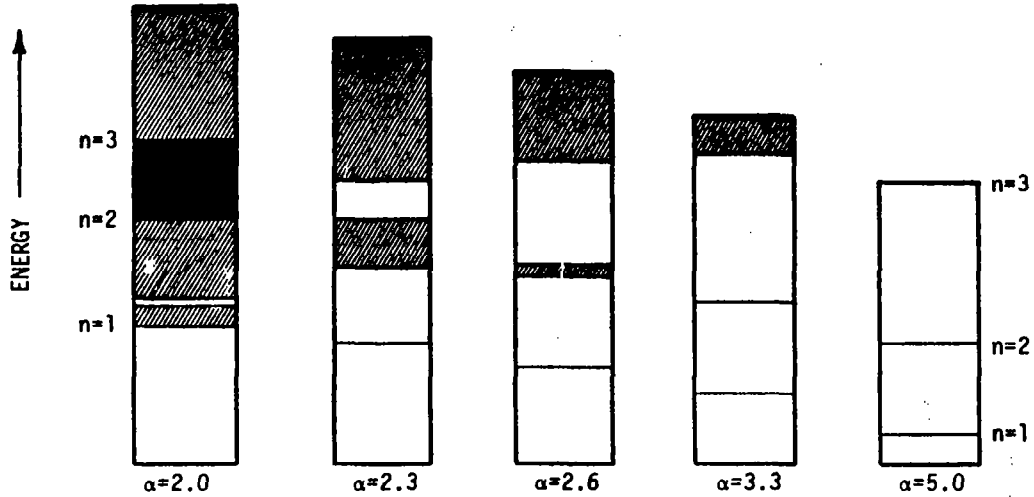


Figure 13. Alternate method of depicting energy gaps resulting from model.

ρ_0 = density of H_2O at $0^\circ C$,

A = 3001 atm ,

B = 3000 atm ,

and

$\gamma = 7$.

A change of variable from density to lattice parameter yields

$$p(\alpha) = A \left(\frac{\alpha_0}{\alpha} \right)^{3\gamma} - B \quad (33)$$

At constant entropy, the work done by pressure, p , on volume, V , is pV ; therefore,

$$\frac{dW}{d\alpha} = \frac{pdV}{d\alpha} + \frac{Vdp}{d\alpha} \quad (34)$$

The atomic volume is set equal to

$$V = \frac{4}{3} \pi \left(\frac{\alpha}{2} \right)^3 ,$$

$$\frac{dV}{d\alpha} = 2 \pi \left(\frac{\alpha}{2} \right)^2 = \frac{\pi}{2} \alpha^2 \quad (35)$$

and

$$\frac{dp}{d\alpha} = -3\gamma \frac{A}{\alpha} \left(\frac{\alpha_0}{\alpha} \right)^{3\gamma} \quad (36)$$

The change in energy as a function of lattice parameter becomes

$$dW = (A - \gamma) \left(\frac{\alpha_0}{\alpha} \right)^{3\gamma} \frac{\pi}{2} \alpha^2 d\alpha - B \frac{\pi}{2} \alpha^2 d\alpha$$

or

$$dW = \left[A - \gamma - B \left(\frac{\alpha_0}{\alpha} \right)^{3\gamma} \right] \frac{\pi}{2} \alpha^2 \left(\frac{\alpha_0}{\alpha} \right)^{3\gamma} d\alpha \quad (37)$$

However, it will be noted that to obtain one atmosphere of pressure under normal conditions ($V = V_0$), it is necessary that $A = B + 1$. If the change of notation $A = P_0$ is made, then the equation of state becomes

$$p = P_0 \left[\left(\frac{\alpha_0}{\alpha} \right)^{3\gamma} - 1 \right] + \left(\frac{\alpha_0}{\alpha} \right)^{3\gamma} \quad (38)$$

$$dp = 3\gamma (P_0 + 1) \left(\frac{\alpha_0}{\alpha} \right)^{3\gamma} \frac{d\alpha}{\alpha} \quad (39)$$

The expression for the energy change becomes

$$dW = \frac{\pi}{2} P_0 \left[-\alpha^2 \left(\frac{\alpha_0}{\alpha} \right)^{3\gamma} \right. \\ \left. + \alpha^2 - \frac{\alpha^2}{P_0} \left(\frac{\alpha_0}{\alpha} \right)^{3\gamma} + \gamma \left(\frac{\alpha_0}{\alpha} \right)^{3\gamma} \alpha^2 \right. \\ \left. + \frac{\gamma \alpha^2}{P_0} \left(\frac{\alpha_0}{\alpha} \right)^{3\gamma} \right] d\alpha ,$$

where the fact that $d\alpha$ is negative has been taken into account. This equation can be rewritten

$$dW = P_0 \frac{\pi}{2} \left(\frac{\alpha_0}{\alpha} \right)^{3\gamma} \alpha^2 \left[(\gamma - 1) \left(1 + \frac{1}{P_0} \right) + \left(\frac{\alpha}{\alpha_0} \right)^{3\gamma} \right] d\alpha \quad (40)$$

It will be a good approximation to consider $1/P_0 \approx 0$ and use

$$dW = P_0 \left(\frac{\pi}{2} \right) \left(\frac{\alpha_0}{\alpha} \right)^{3\gamma} \alpha^2 \left[(\gamma - 1) + \left(\frac{\alpha}{\alpha_0} \right)^{3\gamma} \right] d\alpha \quad (41)$$

as the energy to be used in further calculations. Having found this energy change as a function of lattice parameter, it is reasonable to assume that as the energy change is greater, the probability is higher that an atom will be ionized. The simplest type of dependence given by assuming that the probability of energy input W ionizing the n th band electron is

$$P_n = \frac{|W|}{|E_n|} = \frac{|W|}{\left| \frac{E_0}{n^2} \right|} = n^2 W_0 \quad (42)$$

where

$$W_0 = \frac{|W|}{|E_0|}$$

and

$$W = \int_{\alpha_0}^{\alpha} dW(\alpha) \quad (43)$$

It can be seen that the probability P_n of ionizing the n th band electron has the form

$$P_n(\alpha) = + n^2 E_0^{-1} \int_{\alpha_0}^{\alpha} f(\alpha') d\alpha' \quad (44)$$

or specifically

$$(45)$$

This probability can easily be integrated to obtain

$$P_n(\alpha) = n^2 E_0^{-1} \frac{\pi}{2} P_0 \int_{\alpha_0}^{\alpha} \left[(\gamma - 1) + \left(\frac{\alpha'}{\alpha_0} \right)^{3\gamma} \right] \left(\frac{\alpha_0}{\alpha'} \right)^{3\gamma} \alpha'^2 d\alpha'$$

$$P_n(\alpha) = n^2 E_0^{-1} P_0 \frac{\pi}{2} \left[(\gamma - 1) \alpha_0^{3\gamma} \left(\frac{\alpha^{3-3\gamma} - \alpha_0^{3-3\gamma}}{3-3\gamma} \right) + \left(\frac{\alpha^3 - \alpha_0^3}{3} \right) \right]$$

and, rearranging terms,

$$P_n(\alpha) = n^2 E_0^{-1} \frac{\pi}{6} P_0 \alpha^3 \left[1 - \left(\frac{\alpha_0}{\alpha} \right)^{3\gamma} \right] \quad (46)$$

This quantity is negative; however, by taking the absolute value of W it is seen that a reversal of sign occurs such that

$$P_n(\alpha) = n^2 E_0^{-1} \frac{\pi}{6} P_0 \alpha^3 \left[\left(\frac{\alpha_0}{\alpha} \right)^{3\gamma} - 1 \right] \quad (47)$$

This function yields zero probability of ionization for zero change in lattice parameter (no compression) and increasing probability as the material is compressed. The probability is chosen to be maximum when the input energy is equal to the ionization potential of the n th band electron. The corresponding value of α is found by solving

$$W(\alpha) = E_n$$

or

$$\alpha_0^{3\gamma} = \alpha^{3\gamma} \left(1 + \frac{k}{\alpha^3} \right) \quad (48)$$

where

$$k = \frac{E_0}{n^2} \frac{6}{P_0 \pi}$$

which must be solved by graphing or iteration for each particular initial value α_0 . The value of α

found by the above procedure is the lower limit beyond which the probability becomes meaningless [$P_n(\alpha) > 1$]. The expression $P_n(\alpha)$ should replace the ionization factor $(\alpha_n/\alpha) F(n)$ given in

equation (30). Results of calculations with this ionization factor are not given because of a shortage of time and the lack of a plotting machine. It is to be expected that some modification of this factor may be necessary to prevent the ionization potential from disappearing when $\alpha = \alpha_0$. However, such a

vanishing factor is more appropriate to a dielectric at $\alpha = \alpha_0$ than a metal. It should be mentioned

that while it is conceptually useful to regard each

band as deriving from a particular atomic state (in the sense of the tight binding method), it is only rigorously true if the energy band is narrow and separated from neighboring bands by large energy gaps. If several bands overlap, they must all be regarded as deriving from the same group of atomic states. This adiabatic device to label crystalline bands in terms of bound atomic levels obviously fails for all higher bands that arise from the continuum. In three dimensions the order of the levels in energy can change as the lattice parameter is varied. The device may then fail even for low-lying bands [5]. Nevertheless, the use of this concept to derive an ionization factor is more satisfying intuitively than simply choosing one which yields the proper results.

Before entirely dismissing the results of the first ionization factor, equation (30), it should be noted that one of the empirical features required for correct results has a basis in theory. The device of using discrete initial values α_n for the various bands

can be justified by the following arguments. As mentioned in the description of how energy bands arise, the interaction of electrons initially in the same state results in each of the initial states being slightly displaced so that the final configuration consists of two (or more) new states. The phrase "interaction of electrons initially in the same state" assumes an importance not immediately obvious. Consider two atoms separated by a distance small enough that the outer orbits overlap and also the outer orbits partially overlap the inner orbits as in Figure 14b. The electrons in the outer orbits and those in the inner orbit are not "initially in the same state." Therefore, although there is an interaction shifting the energy levels, the levels do not necessarily spread out to form a band. Only when the separation of atoms is such that the inner levels overlap ($\alpha < 2 \times r_{\text{inner level}}$) do these levels spread into a band. This is the justification for the use of the α_n and a possible need for similar provision in $P_n(\alpha)$ such that $P_n(\alpha) \rightarrow P_n(\alpha_n)$.

The problem was also considered in general thermodynamic terms in an attempt to impose limitations upon the usefulness of the model. The treatment follows Seitz and Turnbull [14] and will not be reproduced in this review. The results can be summarized by stating that the change in energy is found to be proportional to the change in volume; i.e.,

$$\Delta E = p_{\text{av}} \Delta V \quad (49)$$

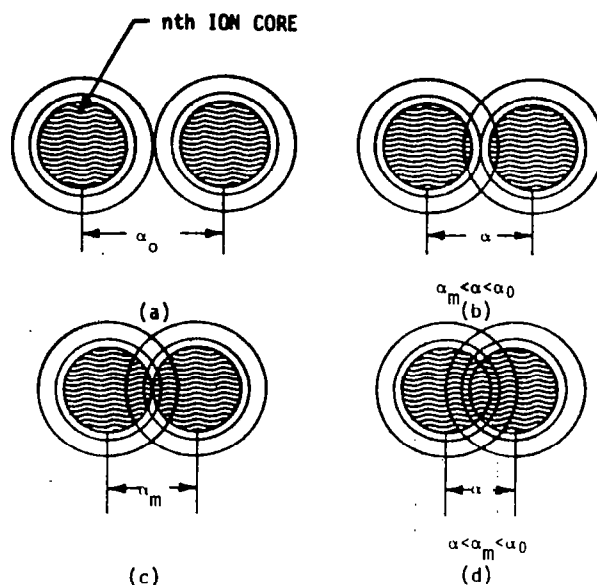


Figure 14. Different possibilities of overlapping wave functions.

This relation can be used to obtain an order of magnitude approximation to the energy changes involved for specific pressures. When the equipartition theorem is used, it follows that about one-half of this energy should contribute to the potential energy. The volume can be expressed in terms of the lattice parameter α (assuming an atomic radius of $\alpha/2$) as

$$V_0 = \frac{4}{3} \pi \left(\frac{\alpha}{2} \right)^3 \approx \frac{\alpha^3}{2} \quad (50)$$

For a pressure of 2 Mb, the lattice parameter is halved; therefore

$$V_1 = \frac{1}{2} \left(\frac{\alpha^3}{8} \right)$$

and

$$\Delta V = V_1 - V_0 \approx \frac{7}{16} \alpha^3$$

The potential energy change is seen to be

$$\Delta E_{\text{pot}} = \frac{1}{2} \Delta E = \frac{1}{2} P_{\text{av}} \Delta V \approx \frac{1}{2} \text{ Mb} \frac{7 \alpha^3}{16} \quad (51)$$

or approximately

$$\Delta E_{\text{pot}} \approx 1 \text{ Mb} \times \frac{\text{atomic volume}}{16} \quad (52)$$

The pressure in megabars can be converted to energy per atomic volume, and the result is found to be

$$1 \text{ Mb} \approx 0.8 \frac{\text{eV}}{\text{atomic volume}}, \quad (53)$$

which yields a change in potential energy,

$$\Delta E_{\text{pot}} \approx \frac{0.8 \text{ eV}}{16} \approx 0.05 \text{ eV} \quad (54)$$

Thus it would appear that at the pressures present in the material, there would be insufficient change in potential energies to affect the conduction bands even assuming all of the energy went into this direction.

One way in which the required energies may be achieved is to use the super-position properties of interfering waves. It is quickly seen that even the added pressures do not yield sufficient energy changes to affect conditions appreciably. This does not,

however, mean that the pressures cannot bring about substantial increases in conductivity. It means only that a simple, linear treatment of the shock waves is insufficient. Interaction and reflection of nonlinear waves lead to enormous increases in pressures as has been verified experimentally. Such nonlinear interactions could very easily result in conduction band energy changes. They also make likely the appearance of hot spots wherein the required energies are available. The study of nonlinear processes seems necessary to gain much more information about conduction brought on by high pressures.

CONCLUSIONS

Qualitatively, the model results in conduction with increasing pressure expressed by means of decreasing lattice parameter. The thermodynamic analysis indicates, however, that a linear treatment of the problem is not capable of determining quantitative behavior with acceptable accuracies. If carried several steps further by a statistical mechanical treatment, the relaxation times for the conducting dielectric could be computed. This information may be sufficient to determine meteor impact velocity from empirical data.

REFERENCES

1. Paul, W.; and Warschauer, M., eds.: Solids Under Pressure. Chapter 13, Physics Experiment With Strong Pressure Pulses, Alder, B. J., McGraw-Hill Book Co., 1963.
2. Paul, W.; and Warschauer, M., eds.: Solids Under Pressure. Chapter 10, The Electronic Structure of Solids Under Pressure, Drickamer, H. G., McGraw-Hill Book Co., 1963.
3. Kronig, R. de L.; and Penny, W. G.: Quantum Mechanics of Electrons in Crystal Lattices. Proc. Roy. Soc. A, 130, 1931, p. 499.
4. Rosenberg, R. L.; and Alder, B. J.: Shocks Up to Infinite Pressures. Conference on Metallurgy at High Pressure, UCRL-7307-T.
5. Wannier, G. H.: Elements of Solid State Theory. Cambridge University Press, 1959, p. 139.
6. Jackson, John D.: Classical Electrodynamics. John Wiley & Sons, New York, 1963.
7. Mott, N. F.; and Jones, H.: The Theory of Properties of Metals and Alloys. Dover Publications, Inc., New York, 1936.
8. Slater, J. C.: Quantum Theory of Matter. Appendix 13, McGraw-Hill Book Co., New York, 1951, p. 475.
9. Rose, M. E.: Elementary Theory of Angular Momentum. John Wiley & Sons, 1963.

REFERENCES (Concluded)

10. McLachlan, N. W.: Theory and Application of Mathieu Functions. Dover Publications, Inc., New York, 1947.
11. National Bureau of Standards, Tables Relating to Mathieu Functions.
12. Slater, J. C.: A Soluble Problem in Energy Bands. Phys. Rev., vol. 87A, 1952, p. 807.
13. Courant, R.; and Friedrichs, K. O.: Supersonic Flow and Shock Waves. Interscience Publishers, Inc., New York, 1948.
14. Seitz, F.; and Turnbull, D., eds.: Solid State Physics. vol. 6, Compression of Solids by Strong Shock Waves, Rice, M. H.; McQueen, R. G.; and Walsh, J. M., Academic Press Inc., 1958.

HIGH TEMPERATURE EQUATION OF STATE FOR ALUMINUM¹

By

R. J. Naumann

SUMMARY

An equation of state is developed that is capable of describing metallic elements in both solid and liquid phase from ambient temperature and pressures to states of extreme temperature and pressure. A novel technique for treating the atomic vibrational contributions is introduced by assuming each atom vibrates independently in a \tan^2 potential. The Schroedinger equation can be solved exactly for this potential function, and the quantum mechanical partition function is computed directly. In this manner a continuous, thermodynamically consistent description of metals is obtained which reduces to an Einstein solid at moderate temperatures and to an ideal gas in the limits of high temperatures and/or large volumes.

Detailed numerical computations are carried out for aluminum. All the constants required to configure the model are obtainable from elementary thermodynamic data at ambient conditions. Excellent agreement is obtained with experimental shock compression data on solid and porous samples at pressures to 5 Mb and temperatures to 25 000°K.

INTRODUCTION

Substantial progress has been made in recent years in understanding the behavior of metals at extreme temperatures and pressures. Shock compression techniques have achieved pressure measurements to approximately 10 Mb and temperatures of tens of thousands degrees [1]. At the lower pressures, the Debye or Einstein model for energy and the Mie-Gruneisen equation for pressure is adequate and zero-degree isotherms were extracted from shock measurements by using these relations to subtract out

the thermal contributions. It was found that a Morse potential predicted the zero-degree isotherms to a fair degree of accuracy [2], which confirmed an earlier suggestion by Slater [3].

As experimental pressures and temperatures increased, various inadequacies in the theory became evident. Electronic contributions were introduced. For compressible metals, anharmonic terms became significant. These were treated by Al'tshuler et al. using the free volume theory of Lennard-Jones and Devonshire [4]. Pastine [5] used the perturbation method of Liebfried and Ludwig [6] to correct for anharmonic effects.

For the high-temperature states reached by shocking porous samples, it was found that the behavior became more ideal gas-like. Kormer [7] proposes a set of empirical interpolation equations to transform solid-like behavior of energy, pressure, and heat capacity to the ideal gas relations. Urlin [8] proposed an empirical free energy function to account for phase transitions. All of these empirical relations require adjustable constants which are evaluated from experimental high-pressure data. Furthermore, there is no guarantee of thermodynamic consistency between them².

An equation of state for metals is developed in this work that is capable of describing the liquid-dense vapor phase as well as the solid phase from ambient conditions to temperatures and pressures exceeding the present experimental range. Rather than use interpolation equations to transform the behavior of a solid to that of a gas at high temperatures or at low densities, the approach will be to start with empirical interatomic potential functions and develop the entire equation of state using quantum statistical mechanics. The only empirical constants required are obtainable from elementary thermodynamic quantities such as

1. This report was based on work submitted in partial fulfillment of the requirements for the degree of Doctor of Philosophy in the Department of Physics in the Graduate School of the University of Alabama.
2. Kormer's pressure, energy, and heat capacity were chosen in such a manner to be consistent among themselves.

heat of vaporization, compressibility, entropy, etc. In this manner the behavior of a metal throughout the entire high-pressure, high-temperature regime can be predicted from its properties at ambient conditions. Since all the thermodynamic properties are derived from the partial function, thermodynamic consistency is guaranteed. This allows a complete thermodynamic description, so that phase transitions are described naturally from Gibbs energy considerations.

FORMULATION

It will be assumed that the Helmholtz energy can be expressed as the sum of three independent contributions: the lattice term, F_k , the ionic vibration term, F_v , and the free electronic term, F_e . Since all thermodynamic functions are derivable from the Helmholtz energy, it immediately follows that they all can be expressed as sums of these three contributions. The fact that there are interactions between the free electrons and the lattice will be accounted for by introducing an effective electron mass.

Lattice Terms

Since the Morse potential has been found to be a reasonable empirical representation for the lattice energy of a metallic solid, the Helmholtz energy for the zero-degree lattice is written

$$F_k = L_o \left(e^{2b(1-\xi)} - 2e^{b(1-\xi)} \right), \quad (1)$$

where L_o is the zero-degree heat of vaporization, or total binding energy, $\xi = (V/V_o)^{1/3}$, and b is an empirical constant determined from the compressibility. From the relation $F = E - TS$, the internal energy, E_k , of the zero-degree lattice is identical to F_k . The zero-degree isotherm is found from the

relation

$$P = - (\partial F_k / \partial V)_T$$

and is

$$P_k = \frac{2L_o b}{3V_o \xi^2} \left(e^{2b(1-\xi)} - e^{b(1-\xi)} \right) \quad (2)$$

Vibrational Terms

At moderate temperatures, the ionic vibrational contributions may be computed from the assumption that the ions behave as harmonic oscillators. This assumption leads to the Einstein model, in which it is assumed that all atoms vibrate independently at the same frequency, or to the Debye model which considers a distribution of normal mode frequencies. At very high temperatures, the vibrational amplitudes are such that nonlinear restoring forces must be considered. This is accounted for by assuming each atom vibrates independently³ in a potential well given by

$$\Phi(x) = \frac{2a^2 m \omega_E^2}{\pi^2} \tan^2 \left(\frac{\pi x}{2a} \right) \quad (3)$$

When the displacement x is small compared to the atomic spacing a , the potential reduces to

$$\Phi(x) = \frac{m \omega_E^2}{2} x^2, \quad (4)$$

where ω_E is the Einstein frequency. For a harmonic oscillator, $\omega^2 = K/m$, therefore, equation (4) has the form $1/2 Kx^2$ where K is the spring constant corresponding to the Einstein frequency.

At larger displacements, $x \approx \pm a$, the potential approaches infinity which describes a hard sphere collision between point masses. This roughly corresponds to nuclear collisions between neighboring atoms whose position expectation values are $\pm a$.

The choice of the \tan^2 functional representation was made because it behaves as desired in the limits

3. The assumption of independent vibration is justified because even at moderate temperatures the Einstein and Debye models give almost identical results.

and also because it allows a closed-form-eigenvalue solution to the Schrodinger equation. The energy eigenvalues are⁴

$$\epsilon_n = (n^2 + n) \epsilon_0 + n \left(\hbar^2 \omega^2 / 8 m a^2 + \epsilon_0^2 \right)^{1/2}, \quad (5)$$

$$n = 0, 1, 2, \dots$$

where ϵ_0 is the degeneracy energy $\pi^2 \hbar^2 / (8 m a^2)$.

The vibrational partition function Z for N atoms, each with three degrees of freedom, is

$$\ln Z = 3N \ln \sum_{n=0}^{\infty} e^{-\epsilon_n / kT} \quad (6)$$

where k is the Boltzmann constant.

The various thermodynamic functions are obtained from the partition function in the usual manner.

$$F_v = -kT \ln Z = -3NkT \ln \sum_{n=0}^{\infty} e^{-\epsilon_n / kT}, \quad (7)$$

$$E_v = kT^2 \frac{\partial \ln Z}{\partial T} = 3N \langle \epsilon_n \rangle, \quad (8)$$

$$C_{vv} = \left(\frac{\partial E_v}{\partial T} \right)_V = \frac{3N}{kT^2} \left[\langle \epsilon_n^2 \rangle - \langle \epsilon_n \rangle^2 \right], \quad (9)$$

and

$$P_v = -kT \frac{\partial \ln Z}{\partial V} = 3N \langle P_n \rangle, \quad (10)$$

where

$$P_n = - \frac{\partial \epsilon_n}{\partial V}. \quad (11)$$

Differentiating equation (5), the P_n contribution becomes

$$P_n = (n^2 + n) \frac{2}{3} \frac{\epsilon_0}{V} + \frac{n}{V} \left[\frac{\gamma \hbar^2 \omega^2 + \frac{2}{3} \epsilon_0^2}{(\hbar^2 \omega^2 + \epsilon_0^2)^{1/2}} \right], \quad (12)$$

where γ is the Gruneisen ratio, $-(\partial \ln \omega / \partial \ln V)$. Formulation of γ for solids has received extensive treatment in the literature.

The brackets $\langle \rangle$ denote the ensemble average; eg.,

$$\langle x \rangle = \frac{\sum_{n=0}^{\infty} x_n e^{-\epsilon_n / kT}}{\sum_{n=0}^{\infty} e^{-\epsilon_n / kT}}. \quad (13)$$

At solid densities, $\hbar \omega \gg \epsilon_0$ and the Boltzmann factor reduces to $\exp [-(n^2 \epsilon_0 + n \hbar \omega) / kT]$. Unless $kT \gg \hbar \omega$, the Boltzmann factor will become negligibly small at low enough values of n to prevent the $n^2 \epsilon_0$ term from contributing significantly. In this case, the Helmholtz energy reduces to

$$F_v = -3NkT^2 \ln \sum_{n=0}^{\infty} e^{-n \hbar \omega / kT} = 3NkT \ln \left(1 - e^{-\hbar \omega / kT} \right), \quad (14)$$

which is the well-known result from the Einstein model.

The Liquid Potential Function

The zero-degree potential energy in the liquid phase is represented by

$$F_k = \begin{cases} L_1 e^{2b(1-\xi)} - \frac{BV_0}{V} & ; \quad \xi \geq \xi_1 \\ L_0 \left(e^{2b(1-\xi/\xi_1)} - 2e^{b(1-\xi/\xi_1)} \right) + E_m & ; \quad \xi \leq \xi_1 \end{cases} \quad (15)$$

where L_1 , B , E_m , and ξ_1 are empirical constants peculiar to the liquid phase, and L_0 and b are the same as in the solid potential, equation (1). This particular form was chosen for the following reasons.

4. See problem 12 in D. ter Haar, Problems in Quantum Mechanics, Academic Press, New York, 1960. Actually, there should be a $1/2$ added to n in both terms corresponding to the ground state. However, the ground state energy is included in the zero-degree lattice terms; therefore, it is suppressed in the vibrational terms.

For $\xi \geq \xi_1$ the repulsive term is the same as in the Morse potential, but the attractive term is the form resulting from van der Waals forces. This potential function cannot be extended to small ξ because eventually the attractive term will override the repulsive term. To avoid this, the form given for $\xi \leq \xi_1$ was chosen. This is identical to the Morse curve for the solid except that E_m and ξ_1 have been introduced to account for the heat of fusion and different compressibility of the liquid phase.

The pressure is again given by $P_k = -(\partial F_k / \partial V)_T$ and is

$$P_k = \begin{cases} \frac{2bL_1}{3\xi_1^2 V_0} e^{2b(1-\xi)} - \frac{BV_0}{V^2} & ; \xi \geq \xi_1 \\ \frac{2bL_0}{3\xi_1^2 V_0} \left[e^{2b(1-\xi/\xi_1)} - e^{b(1-\xi/\xi_1)} \right] & ; \xi \leq \xi_1 \end{cases} \quad (16)$$

Of the four additional constants introduced in this potential, two are required to match the F_k and P_k at $\xi = \xi_1$. The remaining two are chosen to produce the observed energy and pressure at the melting point⁵. Figure 1 compares the liquid potential with the Morse potential for aluminum.

The Liquid Vibrational Component

The Lennard-Jones Devonshire model of liquid and dense vapors treats each atom as though it were moving in a cage of its nearest neighbors which are considered fixed. Since the number of nearest neighbors is usually 12, a high degree of symmetry exists, and a spherically symmetric potential may be assumed. Following these concepts, the same form of potential function as assumed for the solid, equation (3), is used to describe the behavior of an atom in such a cage.

The partition function will be somewhat different from equation (6), however, because of particle indistinguishability. In the solid phase, particles are, in a sense, distinguishable because of their

definite position in the lattice. In a liquid, particles can exchange positions and thereby lose their distinguishability. The partition function must be adjusted accordingly for "proper Boltzmann counting." Since each atom occupies a cell with volume $(2a)^3$, a volume containing N atoms spaced at average distance, a , can have $N/8$ cells. There are $(N/8)^N$ ways of arranging N particles among $N/8$ cells, of which $N!$ are redundant because of particle indistinguishability. The partition function becomes

$$Z = \frac{(N/8)^N}{N!} 3N \sum_{n=0}^{\infty} e^{-\epsilon_n/kT} \quad (17)$$

The Helmholtz energy becomes, using Stirling's approximation,

$$F_v = NkT (\ln 8 - 1) - 3NkT \ln \sum_{n=0}^{\infty} e^{-\epsilon_n/kT} \quad (18)$$

The energy eigenvalues, ϵ_n , are given by

equation (5); the internal energy and heat capacity are given by equations (8) and (9), respectively, and the pressure is given by equations (10) and (12), except that the Einstein frequency and the Gruneisen ratio will have different values for the liquid.

It is interesting to examine the behavior of the liquid in the limit of large volumes where $K\omega \rightarrow 0$. In this limit, the atom moves freely within its "cage." Encounters with the wall correspond to elastic point collisions characteristic to an ideal gas. Since $kT \gg \epsilon_0$, the summations may be replaced with integrations and

$$\sum_{n=0}^{\infty} e^{-\frac{(n^2 + 2n)\epsilon_0}{kT}} \rightarrow \left(\frac{\pi kT}{4\epsilon_0} \right)^{1/2} \quad (19)$$

The Helmholtz energy becomes

$$F_v = -NkT - \frac{2}{3} NkT \ln \left[\frac{mkT}{2\pi h^2} \left(\frac{V}{N} \right)^{2/3} \right] \quad (20)$$

5. The parameter, ξ_1 , is the value of ξ corresponding to minimum potential in the liquid phase. It will generally be more than unity because the distribution of the atoms in liquid metals is random instead of the more efficient close packing usually associated with crystal lattices. This choice of functional dependence was made to assure $P_k(\xi_1) = 0$ and to make the F_k and P_k approach the same values as the solid phase at small ξ .

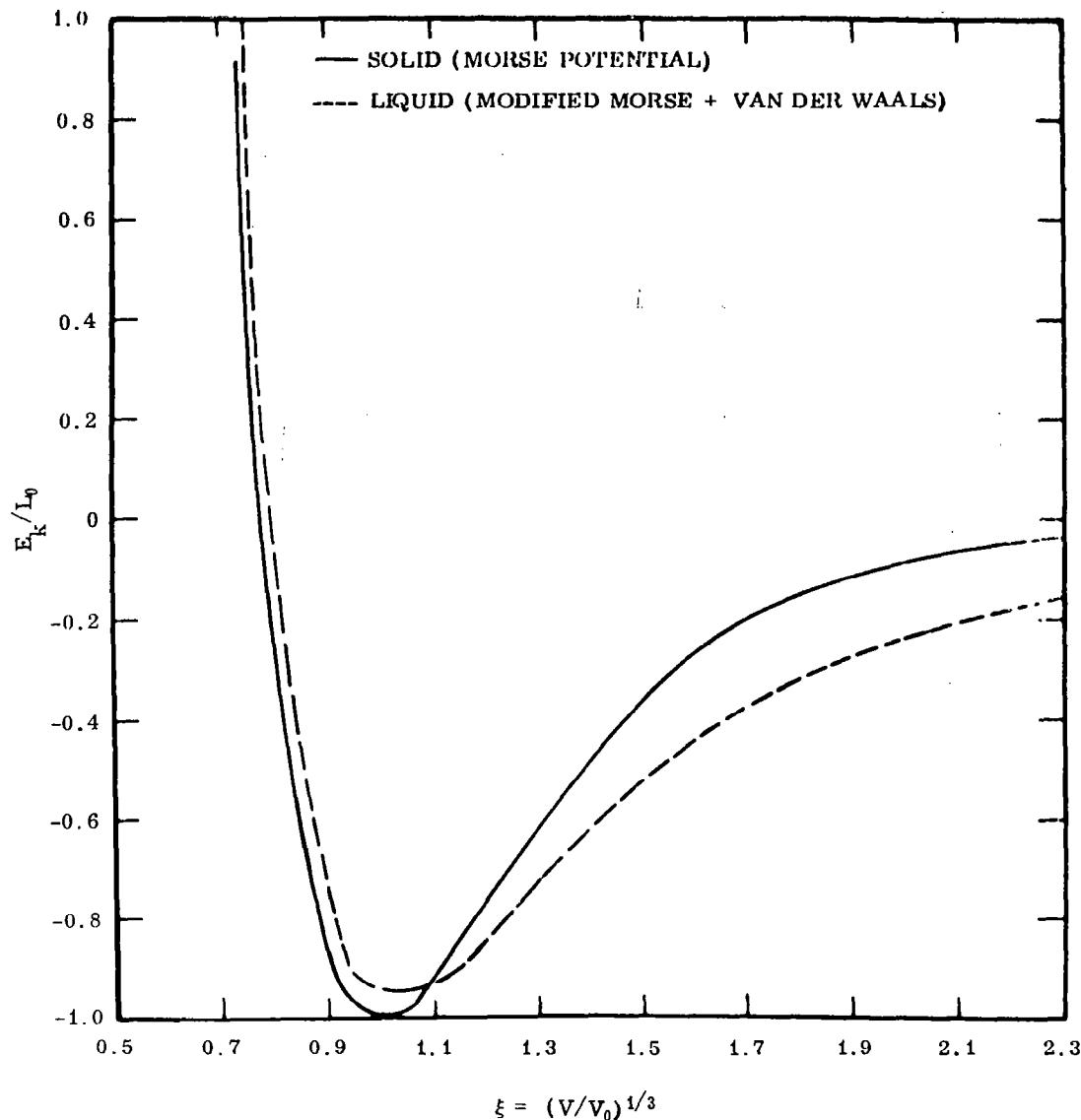


Figure 1. Comparison of solid and liquid potentials. (The liquid potential approaches the solid at high compressions, differs by approximately the heat of fusion at $V = V_0$, and exhibits a van der Waals behavior at large volumes.)

Similarly, the other equations reduce to the ideal gas relations, $E_v = \frac{2}{3} NkT$, $P_v = \frac{NkT}{V}$, and

$C_{vv} = \frac{3}{2} Nk$. Using the result of equation (20), the relations $S = (E-F)/T$, and the fact that $E_k = F_k$, the entropy in this limit becomes

$$S = \frac{5}{2} Nk + \frac{3}{2} Nk \ln \left[\frac{mkT}{2\pi h^2} \left(\frac{V}{N} \right)^{2/3} \right], \quad (21)$$

which is the well-known Sakur-Tetrode equation for the entropy of an ideal gas.

At liquid densities, $\hbar\omega \gg \epsilon_0$ and the treatment of the vibrational component of liquids at moderate temperature reduces to the Einstein model. However, the Einstein frequency and the Gruneisen ratio will be different in the case of a liquid.

A crude estimate of the vibrational frequency can be made by considering an atom at the origin with an atom at $\pm a$. The change in potential resulting from a displacement x is

$$\Phi(x) = \Phi(a+x) + \Phi(a-x) - 2\Phi(a) \quad (22)$$

Using only the repulsive term in the Morse Potential,

$$\Phi(r) = \Phi_0 e^{\frac{2b(1-r/a_0)}{a_0}},$$

$$\Phi(x) = 2 \Phi_0 e^{2b(1-\xi)} \left[\cosh\left(\frac{2bx}{a_0}\right) - 1 \right] \quad (23)$$

For small displacements,

$$\Phi(x) \approx 2 \Phi_0 e^{2b(1-\xi)} \frac{4b^2 x^2}{a_0^2} \quad (24)$$

This has the form of a harmonic oscillator potential with a frequency

$$\omega^2 = \frac{4 \Phi_0 b^2}{m a_0^2} e^{2b(1-\xi)} \quad (25)$$

from which $\gamma = \frac{1}{3} b \xi$. The ω as a function of volume can be found from equation (25) and the value of ω_0 at $\xi = 1$. This can be obtained from entropy measurements. In the limit of the Einstein model, the entropy becomes

$$S = 3 N k \left(\frac{K\omega/kT}{e^{K\omega/kT} - 1} \right) - 3 N k \ln (1 - e^{-K\omega/kT}) - N k (\ln 8 - 1) \quad (26)$$

Given S and T , the above expression can be solved for ω .

Figures 2 and 3 show how the vibrational component of heat capacity approaches ideal gas-like behavior in the limit of high temperatures or low densities.

Electronic Contributions

The electronic terms are obtained by treating the free electrons as an ideal Fermi gas. From the

grand partition function, one obtains [9]

$$\frac{N}{V} = g \int_0^\infty \frac{\epsilon^{1/2} d\epsilon}{e^{(\epsilon-\mu)/kT}} \quad (27)$$

and

$$E = g \int_0^\infty \frac{\epsilon^{3/2} d\epsilon}{e^{(\epsilon-\mu)/kT}} \quad (28)$$

where

$$g = \frac{2^{7/2} \pi m^{3/2}}{h^3}$$

The chemical potential μ must be found for a given volume and temperature by a numerical iterative solution of equation (27), then equation (28) may be integrated to find E . The pressure is obtained from the identity, $PV = \frac{2}{3} E$, which holds for Fermi as well as Bose gases. Since, by definition, the chemical potential is the Gibbs energy per atom, $G = N\mu$. Using the identity $G = F + PV$, the electronic contribution to the Helmholtz energy may be found.

For temperatures that are small compared to the Fermi temperature, the integral in equation (27) may be approximated

$$\mu = \epsilon_F - \frac{\pi^2 k^2 T^2}{12 \epsilon_F} + \dots \quad (29)$$

and equation (28) becomes

$$E = \frac{3}{5} N \epsilon_F + \frac{\pi^2}{4} \frac{N k^2 T^2}{\epsilon_F} \quad (30)$$

where the Fermi energy ϵ_F is

$$\epsilon_F = \frac{h^2}{8m} \left(\frac{3}{\pi} \frac{N}{V} \right)^{2/3} \quad (31)$$

The first terms in equations (29) and (30) are the zero-degree degeneracy energy. This is already contained in the lattice terms and will therefore be suppressed. The electronic contribution to the Helmholtz energy is

$$F_e = - \frac{\pi^2 N k^2 T^2}{\epsilon_F}$$

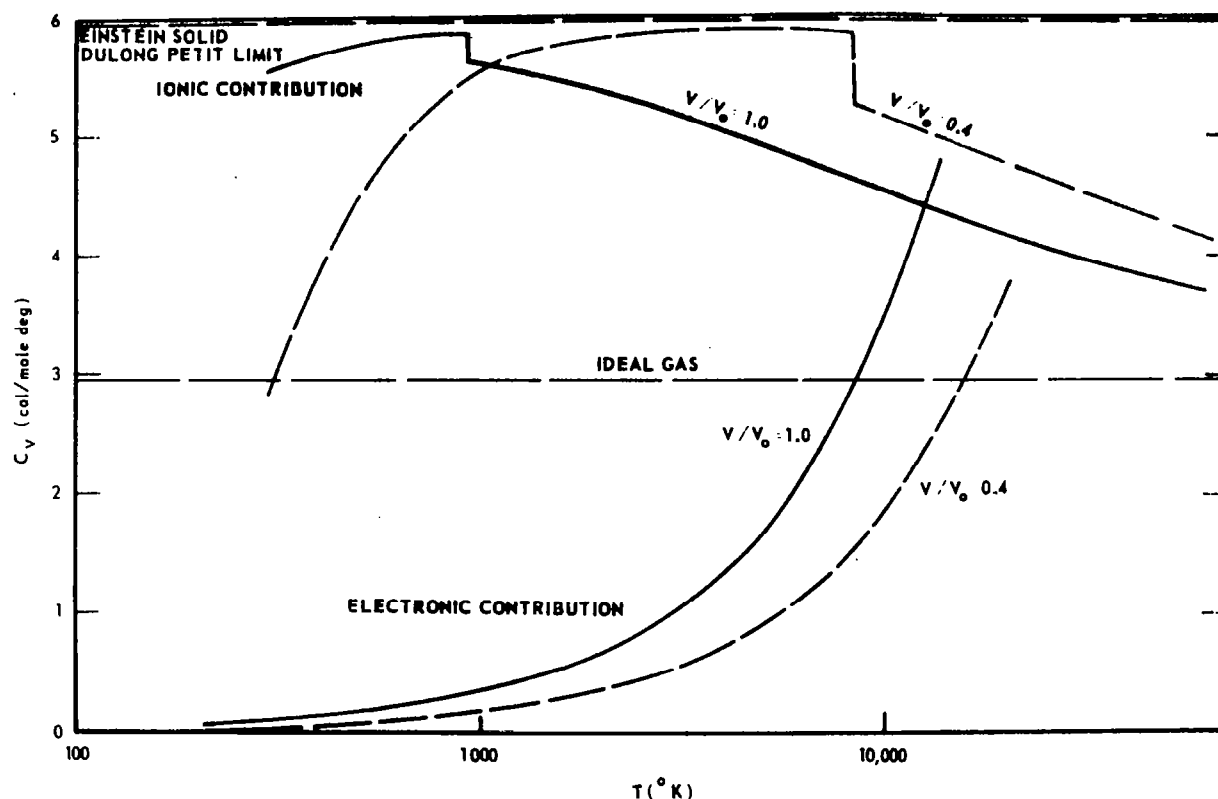


Figure 2. Behavior of heat capacity for solids and liquids in the high temperature regime. (Breaks in the curves represent phase changes.)

The Fermi energy is computed from the observed electronic heat capacity coefficient which can be measured at low temperatures. The C_{ve} is obtained by differentiating equation (30), giving

$$C_{ve} = \left(\frac{\partial E_e}{\partial T} \right)_V = \frac{\pi^2 N k^2 T}{2 \epsilon_F} \quad (32)$$

At very low temperatures, the electronic terms dominate the heat capacity, which is experimentally observed to depend linearly on T . The value of ϵ_F obtained in this manner will be somewhat different from the value obtained from equation (31) if the free electron mass is used for m . This difference arises from the interaction of the electrons with the lattice. The effective electron mass is defined as that mass which makes equation (31) agree with the Fermi energy obtained from the experimental heat capacity.

COMPUTATIONAL RESULTS

Specification of Constants

The equation of state developed in the preceding section was applied to aluminum. The various constants required are obtained in the following manner.

The zero-degree heat of vaporization L_0 is found from tables [10] to be 86 400 kcal/mole. The volume at 0°K is obtained by extrapolation of thermal expansion data and is taken to be 2.736 gm/cm³. From compressibility data, b is found to be 3.241.

The Slater relation [11],

$$\gamma = -\frac{2}{3} - \frac{1}{2} \frac{VP_k''/P_k'}{P_k'}, \text{ where primes denote}$$

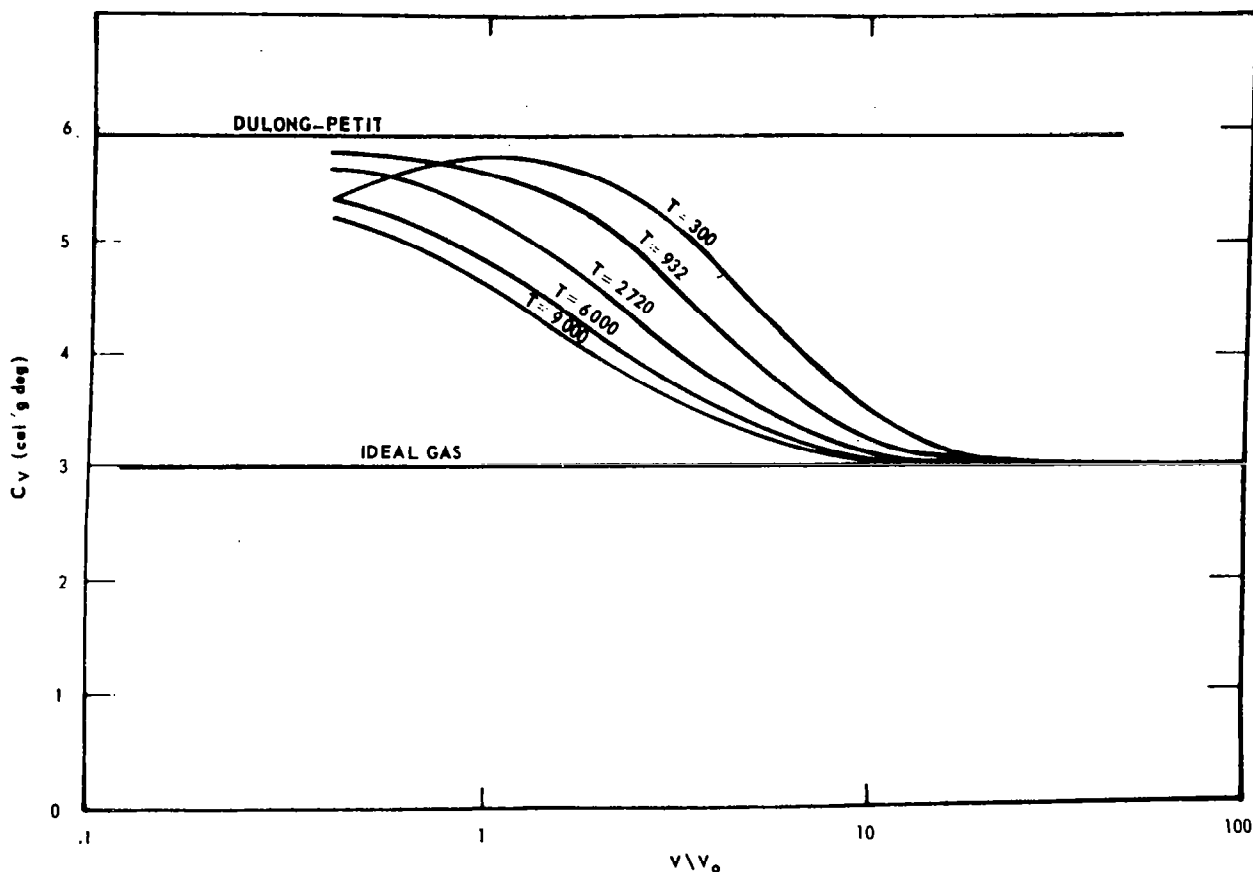


Figure 3. Transition of heat capacity from liquid to gaseous behavior. (The curves indicate the behavior of the vibrational component of the liquid phase only, and ignore the liquid-gas coexistence region.)

differentiation with respect to V , gives γ to within a few percent of the experimental value at normal density. Because of this agreement the Slater relation was used for the calculation for solid aluminum despite the objection that it assumes a volume independent Poisson ratio. In the development of the Slater relation, the result

$$\omega_E^2 = \omega_o^2 \left(\frac{V}{V_o} \right)^{4/3} \frac{P'_k(V)}{P'_k(V_o)}$$

is obtained. Given ω_o , the Einstein frequency at V_o , the ω_E at any other V can be found. The quantity ω_o is found by comparing the entropy of an ideal solid in the Einstein approximation to the measured value at low temperature and using the Slater relation to correct to V_o . For solid

aluminum, the Einstein temperature, $\theta = \hbar\omega/k$ was found to be 269.38°K. For the liquid phase, the entropy in equation (26) is used to find the liquid Einstein temperature which is corrected to V_o using equation (25). For liquid aluminum, the Einstein temperature was found to be 117.935°K.

The electronic terms for aluminum are obtained by considering all three valence electrons as free and by taking the effective mass to be 1.6 times the normal electron mass. This brings the calculated electronic heat capacity, equation (32), into agreement with the measured value [12].

The constants L_1 , B , E_m , ξ_1 in the liquid potential are found in the following manner. At the melting volume ratio ξ_m and temperature T_m , the

energy is $E_k(\xi_m) + E_v(\xi_m, T_m) + E_e(\xi_m, T_m)$ which must equal to the energy of the zero-degree crystal L_0 plus the heat to melt, which is known experimentally. All quantities required to compute

$E_v(\xi_m, T_m)$ and $E_o(\xi_m, T_m)$ have been specified; thus, $E_k(\xi_m)$ is known. Similarly,

$$P_k(\xi_m) + P_v(\xi_m, T_m) + P_o(\xi_m, T_m) = P_{atm};$$

therefore, $P_k(\xi_m)$ is known. Using equations (15)

and (16) for $\xi \geq \xi_1$, simultaneous equations containing L_1 and B are obtained. Their solution for aluminum yields $L_1 = 72\,531$ cal/mole, and $B = 146\,397$ cal/mole. The quantity ξ_1 is found by requiring the two expressions for P_k , equation (16),

to be equal at $\xi = \xi_1$. For aluminum, it was found that $\xi_1 = 1.0265$. Finally, the requirement that both expressions for E_k , equation (18), agree at

$\xi = \xi_1$ is used to obtain $E_m = 2654$ cal/mole.

The Fusion Curve and Equation of State Surfaces

Having specified the various constants for aluminum, computations were carried out for both the solid and liquid phase for various values of ξ and T . Isotherms of a Gibbs energy versus pressure plot are shown in Figure 4. Since the phase that produces the lowest Gibbs energy at a given temperature and pressure is the stable phase, the intersections of the solid-liquid isotherms represent points on the fusion curve (Fig. 5). Using the fusion curve, isotherms are constructed on a P - V surface (Fig. 6), an E - V surface (Fig. 7), and an S - V surface (Fig. 8). Isoenergy lines on a P - V surface are shown in Figure 9.

Comparison with Experimental Results

To compare the equation of state developed in this paper with data obtained from shock compression experiments, the Hugoniot requirement,

$$E - E_o = \frac{1}{2} P(V_{oo} - V) \quad (33)$$

is solved simultaneously with the equation of state. In experiments with porous samples, the volume

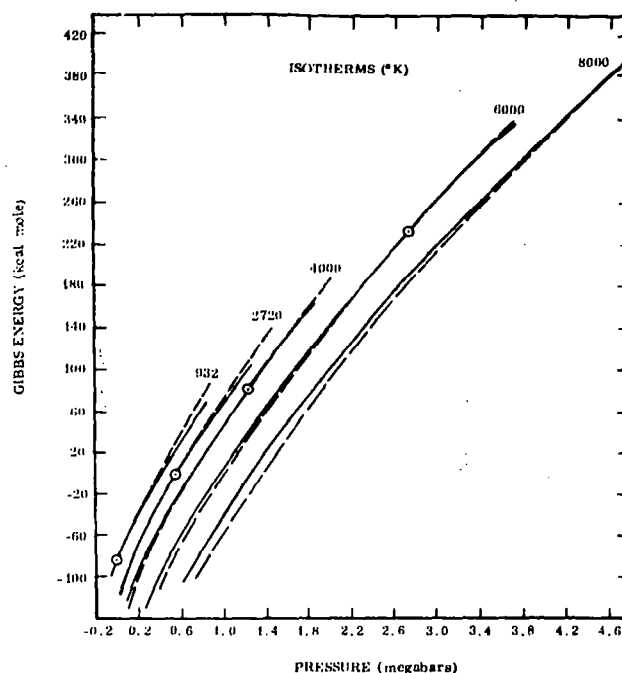


Figure 4. Gibbs energy isotherms. (Circles represent the intersection of the liquid and solid isotherms and determine the melting pressure for that particular temperature.)

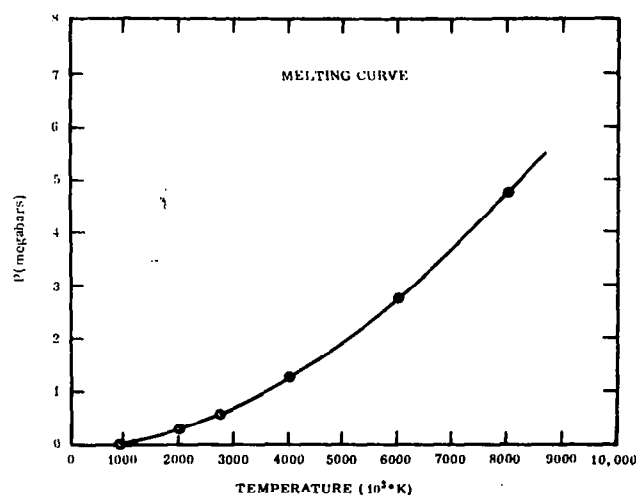


Figure 5. Melting curve deduced from Gibbs energy plot.

V_{oo} represents the actual specific volume of the sample, which may be several times the volume of a

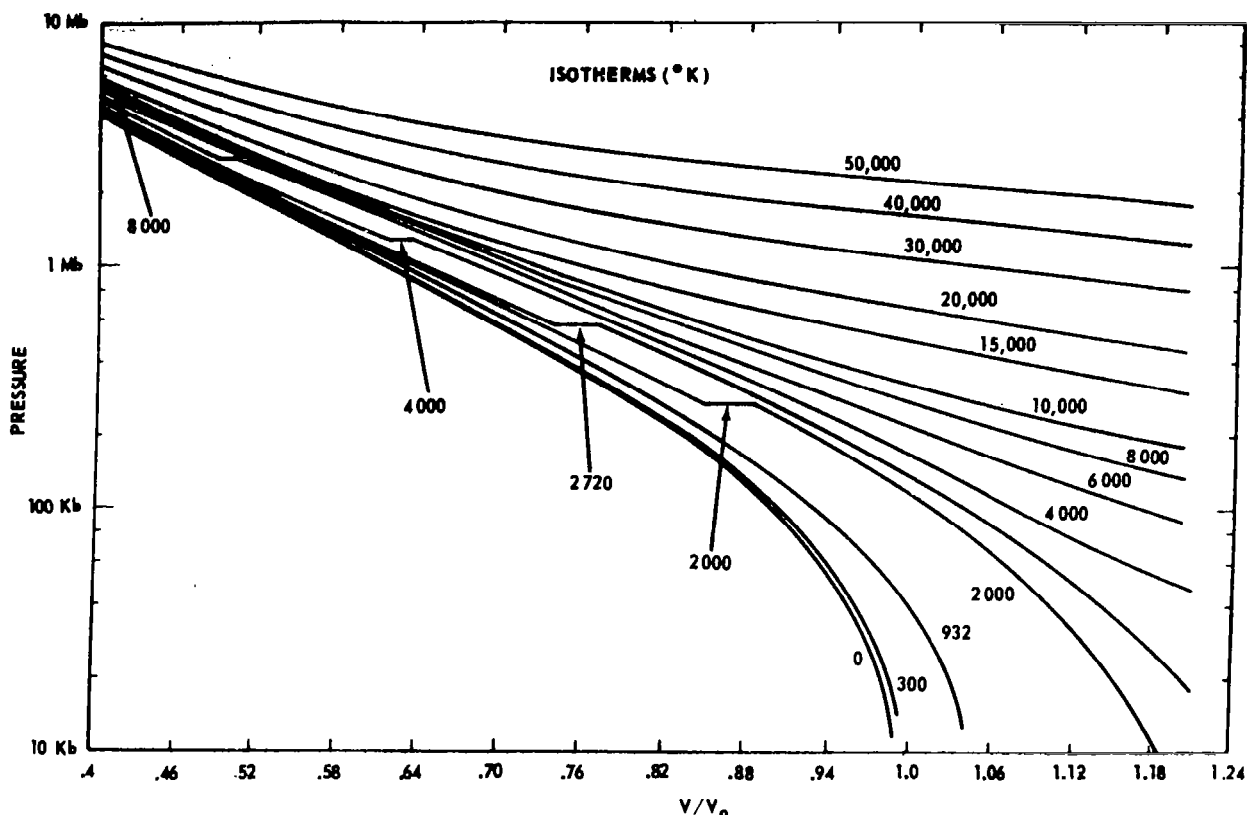


Figure 6. Pressure isotherms. (Breaks in the isotherms represent transition from solid to liquid phase.)

normal crystal. The states that can be reached by shocking a crystal with initial specific volume ratio V_{00} must lie along the intersection of equation (33) and the equation of state surface in P - V - E space (Fig. 9). By varying the porosity of the sample, any state can, in principle, be reached by shock compression.

In performing shock compression experiments, the observables are the shock velocity D and the material velocity u . These are related to the thermodynamical quantities E , P , and V through the Hugoniot relations

$$V_{00}(D-u) = VD \quad (\text{conservation of mass}) \quad (34)$$

$$PV_{00} = Du \quad (\text{conservation of momentum}) \quad (35)$$

These relations are used to relate the observables u and D to the Hugoniot states found by solving equation (33) with the equation of state. Figure 10

compares the predicted results for various porosities with measured results summarized in Table 1. Very good agreement is obtained considering that the equation of state constants are determined solely from ambient properties and contain no constants adjusted to fit the high-pressure data. The highest pressure datum point falls somewhat above the predicted curve for liquid aluminum, but is below the curve for solid aluminum. The fusion curve clearly indicates that melting should have occurred at this state, but the fact that the material was shock compressed may have prevented the phase transition to become complete in the short time involved, and the discrepancy could be that the aluminum is behaving as a super-heated solid. On the other hand, the inaccuracies in the model, particularly in the assumption of a Morse potential configured from the ambient compressibility, could easily account for such a discrepancy at pressures of 5 Mb.

The reproduction of states on the Hugoniot for normal crystal density is not a particularly crucial test for an equation of state. The lattice terms are

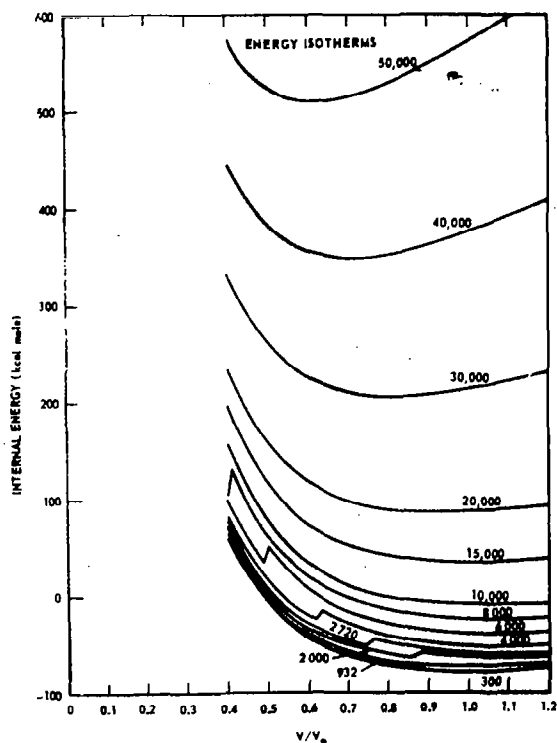


Figure 7. Energy isotherms. (Breaks in the isotherms represent transitions from solid to liquid phase.)

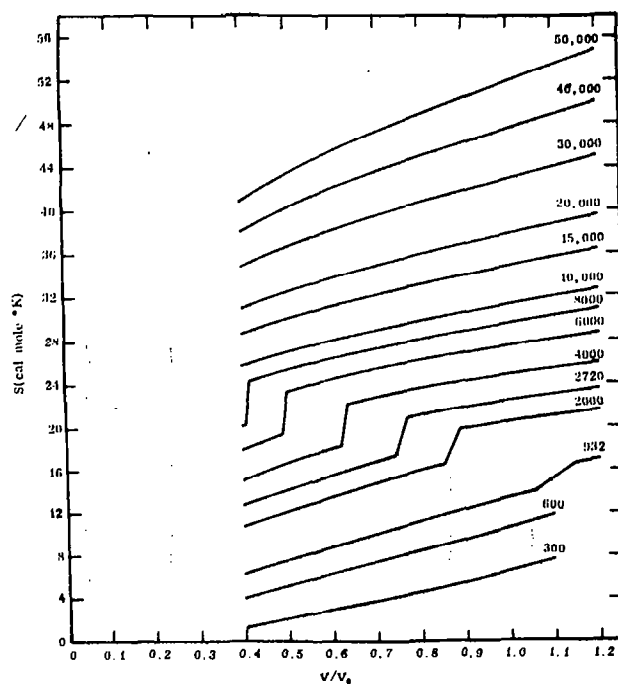


Figure 8. Isotherms on S-V plot. (Breaks in the isotherms represent transitions from solid to liquid phase.)

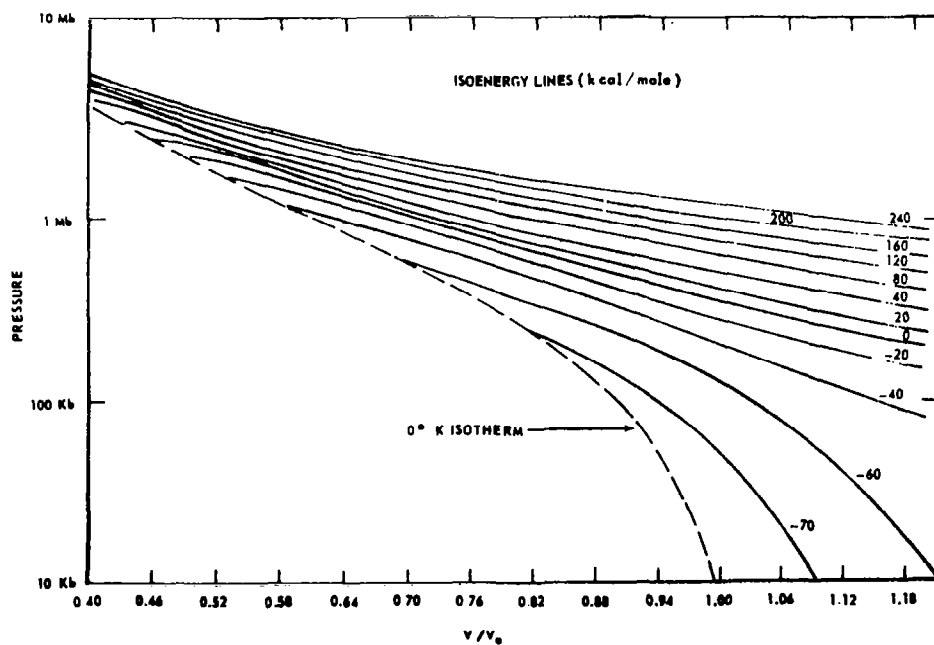


Figure 9. Isoenergy lines. (When lines of constant internal energy are plotted rather than lines of constant temperature, the phase transitions are not apparent.)

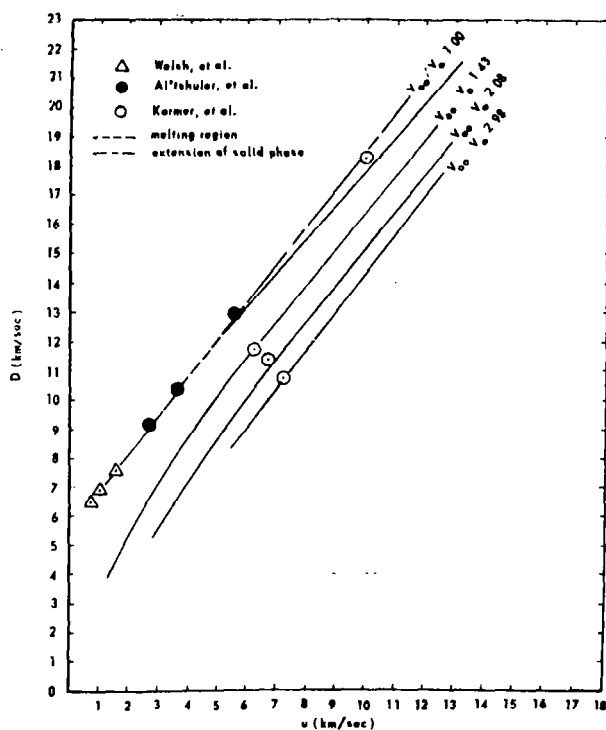


Figure 10. D-u plots comparing computed results with experimental data points. (The short dashed region on the $V_{oo}/V_o = 1$ curve represents the transition region from solid to liquid phase. The long dashed curve represents a superheated solid.)

the major contributors at all but the highest compressions, and the fact that the restoring forces "stiffen up" at high compressions extends the validity of the assumption that the atoms vibrate as harmonic oscillators to high temperatures. Therefore, the Einstein or Debye Model together with the Mie-Gruneisen equation and a properly adjusted zero-degree isotherm will give a good representation of the normal Hugoniot to several megabars. Addition of electronic terms will extend such a model even further. However, such models fail for the lower compression, higher temperature states obtained by shock compressing porous samples. The equation of state developed in this work successfully predicts these states, as shown in Figure 10.

It is useful for shock compression work to plot various thermodynamic coordinates against material velocity u as a means of expressing the thermodynamic state attained in a shock process. The material velocity is particularly useful because it can

be easily related to the relative velocity of the impacting samples. Figure 11 is a plot of pressure for different porosities versus u , and experimental points are shown for comparison.

Figure 12 is a plot of temperature in the shocked region as a function of u . The various datum points are illustrated not as a comparison, since measurement of temperatures were not made, but as an indication of the range of temperatures accessible to this technique. The fact that higher temperatures are produced by increasing the porosity is dramatically illustrated by comparing the temperature for the 1.43, 2.08, and 2.98 points and 1.00 point at 5.62 km/sec. These states were created by the same impact velocity. The fact that there is a discontinuity

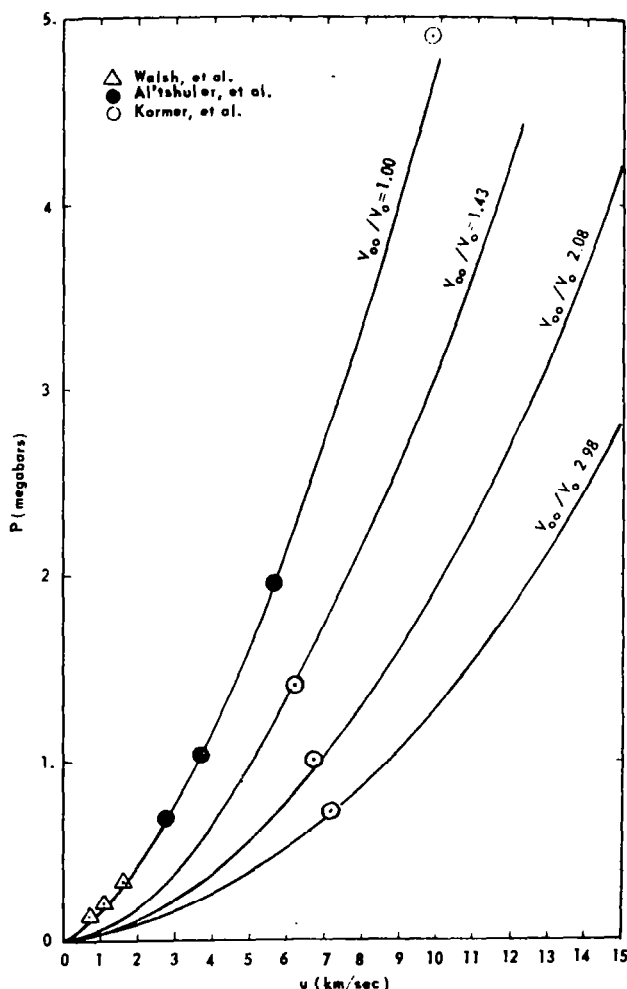


Figure 11. P-u plots comparing computed results with experimental data points. (No abrupt change is apparent that would indicate a phase transition.)

TABLE 1. SUMMARY OF HUGONIOT DATA FOR ALUMINUM

GROUP I ^a				
D (km/sec)	u_f (km/sec)	P(kb)	V/V_o	
7.531	3.230	335.8	0.7874	
6.927	2.319	222.7	0.8333	
6.500	1.700	153.5	0.8696	
GROUP II ^b				
D (km/sec)	u (km/sec)	P(kb)	V_o/V	
9.13	2.80	693	1.442	
10.39	3.70	1042	1.553	
12.94	5.62	1971	1.767	
GROUP III ^c				
V_{oo}/V_{300}	D (km/sec)	P(Mb)	V_o/V	u^d
1.00	$18.31 \pm .16$	4.93	2.185	9.93
1.43	$11.74 \pm .10$	1.391	1.498	6.25
2.08	$11.42 \pm .09$	1.003	1.176	6.74
2.98	$10.75 \pm .08$	0.702	1.015	7.18

^aThese are representative points of those listed by J. M. Walsh, M. H. Rice, R. G. McQueen, and F. L. Yarger, Phys. Rev.: 108, 196 (1957) The Material velocity u is taken to be 1/2 the measured free surface velocity, u_f .

^bL. V. Al'tshuler, S. B. Kormer, A. A. Bakanova, and R. F. Trunin; Soviet Physics — JETP, 11, 573 (1962)

^cS. B. Kormer, A. I. Funtikov, V. D. Urtin, and A. N. Kiksnikova, Soviet Physics — JETP, 15, 477 (1962)

^dThe quantity u was not stated in the paper. It was recovered by the relation $u = [1 - (V/V_o) (V_{300}/V_{oo})] D$.

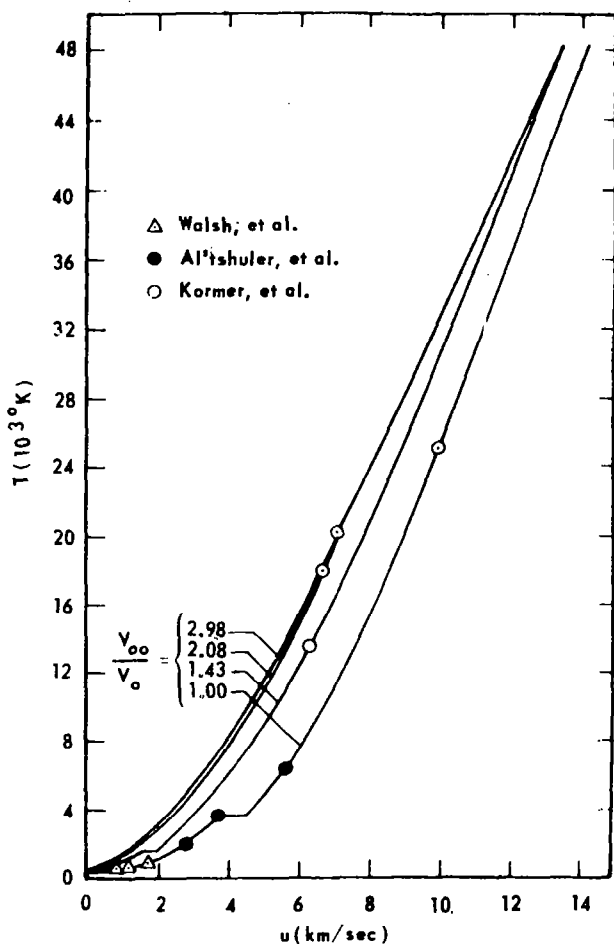


Figure 12. T - u plots. (The data points are shown only to indicate range of temperatures reached by present experimental techniques. The break in the curves indicates that temperature measurement could serve as a method of detecting phase transitions.)

in the temperature curve at the melting region gives a possibility of experimentally detecting the melting point at very high pressures, although such temperature measurement would be extremely difficult to make in solids.

Figure 13 is a plot of entropy as a function of u . As before, the indicated data points are intended only to indicate range of experimental states, not measurements. For comparison, the temperature and phase of aluminum at ambient pressure for various values of entropy is indicated. Assuming the release is adiabatic and isentropic, an estimate of the release temperature can be made. Attempts have been made to measure the release temperature of shock compressed solids. Taylor [13] reports a favorable

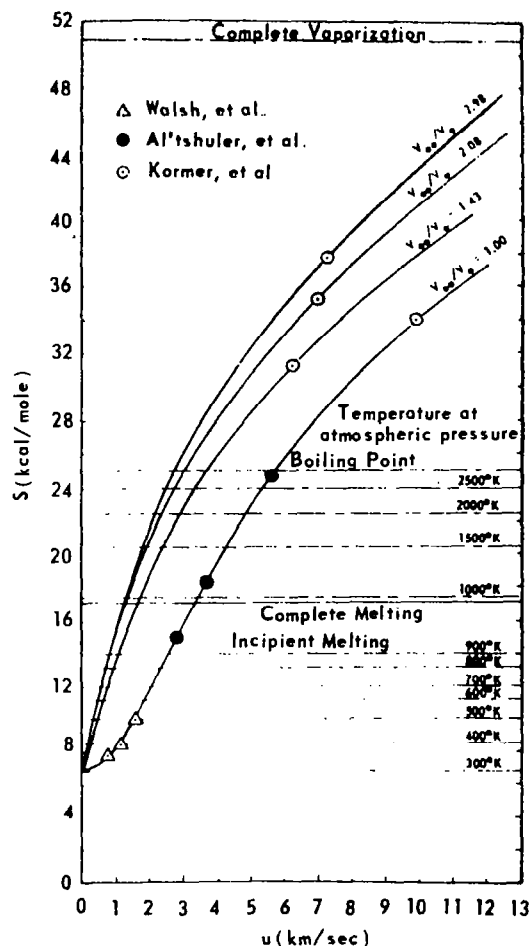


Figure 13. S - u plots. (The data points indicate measurement range rather than actual measurements. The dashed lines indicate entropy values corresponding to the stated temperatures at ambient pressure. If the release is assumed to be isentropic, these can be used to indicate release temperature.)

comparison between calculated and measured release temperatures for Cu up to the melting point.

CONCLUSIONS

A complete equation of state for metals that describes both the solid and liquid-dense vapor phase has been developed. All empirical constants required can be obtained from elementary thermodynamic data at ambient conditions. Since all thermodynamic functions are derived from the partition function, thermodynamic consistency is guaranteed. Phase transitions between the solid and liquid come about

naturally by using the Gibbs energy to determine the stable phase for a given state. Detailed computations were carried out for aluminum and the ability for the model to predict the behavior of aluminum for pressures of 5 Mb and temperatures of 20 000°K was demonstrated. Since only elementary thermodynamic data at ambient conditions are required to configure the model, extension to other metals is straightforward by insertion of their appropriate constants.

The model can be extended to higher temperatures with some additional computational effort to obtain the electron contributions for temperatures comparable to the Fermi temperature. The model can also be extended to lower densities, provided the temperatures are low enough to completely neglect electronic contributions.

REFERENCES

1. Al'tshuler, L. V.; Bakanova, A. A.; and Trunin, R. F.: JETP, vol. 15, no. 477, 1962.
2. Pastine, D. J.: J. Appl. Phys., vol. 35, no. 3407, 1964.
3. Slater, J. C.: Introduction to Chemical Physics. Chapter XXII, McGraw Hill, New York, 1939.
4. Lennard-Jones, J. E.; and Devonshire, A. F.: Proc. Roy. Soc., London, vol. A163, no. 53, 1937.
5. Pastine, D. J.: Phys. Rev., vol. 166, no. 703, 1968.
6. Liebfried, G.; and Ludwig, W.: Solid State Physics. Vol. 12, Academic Press, New York, 1961.
7. Kormer, S. B.; Urlin, V. D.; and Popova, L. T.: Soviet Physics — Solid State, vol. 3, no. 1547, 1962.
8. Urlin, V. D.: Soviet Physics — JETP, vol. 22, no. 341, 1966.
9. Huang, K.: Statistical Mechanics. Chapter 9, Wiley and Sons, New York, 1963.
10. Stull, D. R.; and Sinke, G. C.: Thermodynamic Properties of the Elements. American Chemical Society, Washington, D. C., 1956.
11. Slater, J. C.: Introduction to Chemical Physics. Chapter XIV, McGraw Hill, New York, 1939.
12. Kittel, C.: Solid State Physics. Chapter 11, Wiley and Sons, New York, 1956.
13. Taylor, J. W.: J. Appl. Phys., vol. 34, no. 2727, 1963.

N70-35513

LOW LIGHT LEVEL TV OBSERVATIONS

By

Stuart Clifton

A number of ways have been employed to investigate the mass-flux characteristics of the near-earth meteoroid environment. Visual and photographic means have been used to define such characteristics in the larger mass region to as small as 10^{-1} gm, while satellites, notably the Pegasus spacecraft, have extended observations of small mass meteoroids to as large as 10^{-6} gm. The mass region between 10^{-1} gm and 10^{-6} gm is a most important region in regard to long term spacecraft such as the S-IVB workshop. This region has been investigated primarily with radar observations. However, problems and uncertainties inherent in the analysis of the radar data have led to the desirability of using alternate methods to examine this mass region.

Such a method is provided through the use of low light level television systems such as the image orthicon, the SEC vidicon, or the image isocon. For this reason, the Meteoroid Physics Branch of the Space Sciences Laboratory has undertaken meteor observations using an image orthicon system. With this system, observations of larger mass meteoroids may be extended to as small as 10^{-4} gm. The system that is used for meteor observations is a Maryland Telecommunications, Inc. Camera Chain with a GE 7967 low light level tube. The camera system uses a 525 line scan at the normal television frame rate of 30 frames per second. The optics used is an Aerojet Delft Rayxar lens with an aperture of approximately 5.5 inches and a speed of f/0.75. The results are video taped by Ampex 660 B/C tape recorders.

Observational procedures are rather simple in that the entire system is portable and may be easily transported to different sites. Once in place, the camera is simply pointed to a selected region of the sky and the system is operated. Although our main observing site is presently on the south end of Redstone Arsenal, the system may be mounted in a DC-3 aircraft as shown in Figure 1 and flown to altitudes of 10 000 ft. This helps to alleviate the poor visibility which often prevails in the Huntsville area. With the Rayxar lens the field of view is approximately 13 by 16 degrees. Viewing at a 45-degree elevation, the observed area of the upper atmosphere in which meteor phenomena occur is approximately 1000 km².

Analysis of the observed results is a very painstaking effort. Many hours of analysis are required for each hour of observation, and a large backlog of data easily develops. The fact that procedures are still being developed to more easily and accurately analyze the data also increases that backlog.

The first step in the analysis is to examine each video tape thoroughly to locate all detectable meteors. Our present analysis procedures require that each observed area of sky be examined twice, since faint meteors are often difficult to detect. When a meteor is detected, its place on tape is noted along with information concerning its direction, spatial position, brightness, and speed. A meteor as observed by the image orthicon system is shown in Figure 2.

Scanning the tapes results in meteor numbers and hourly rates. To date nearly 600 meteors have been detected. On the basis of the results recorded by other observers, hourly rates of from 15 to 20 were expected. However, our analysis procedures have detected consistently higher rates than this; hourly rates often rise above 30 per hour and occasionally rise as high as 60 to 70 per hour. It should be mentioned that the higher rates were observed during late summer and fall of last year, and the highest rates were observed in the vicinity of the Leonid meteor shower. However, because of inclement weather, no observations were made during the actual shower period.

The next step of the analysis is to determine the angular rates of the observed meteors. This consists of establishing two points along the trajectory of the meteor, finding the time required by the meteor to traverse this distance, and, with the aid of star charts, calculating the angular distance between the points. This results in the angular rate of the meteor in degrees per second.

The distribution of angular rates as observed by the camera for 200 meteors is shown in Figure 3. This does not necessarily reflect the actual distribution of angular rates, since it is easier for the orthicon to detect slower meteors. This results from the fact that a faster meteor has a faster writing speed across the photocathode, and fewer photons are deposited in each resolving element. Therefore,



Figure 1. Image orthicon and accessory equipment mounted in the DC-3 for airborne meteor observations.

given two meteors of equal brightness, the slower object will appear brighter to the camera than the faster one.

This effect is shown more clearly in Figure 4. In a laboratory test an object of steady brightness was observed at different angular velocities. It may be seen that the faster the object moved, the more difficult it was to detect. For meteors this means that as the angular rate becomes greater, the limiting magnitude becomes brighter. Limiting magnitudes for stars usually occur at about the 9th or 10th magnitude, and in exceptional cases, at the 11th magnitude, but meteors this faint could only be detected if they possessed nearly a zero angular rate, and then the lack of a trail would probably render them unobserved.

Determination of the magnitude of a meteor and the calculation of the integrated light curve of the meteor have presented the most difficult problems associated with the analysis to date. A complete analysis must take into consideration not only how to interpret what is actually observed, but also the manner in which the television system records what is observed. Low light level photometry through the use of television systems is a relatively new area of endeavor compared with the more frequent use of pattern discernment, and the analysis procedures are somewhat uncertain. A number of methods have been attempted to calculate the meteor magnitudes, but no single method has shown itself able to determine these magnitudes over the range of observed brightnesses. It is possible that any complete analysis will have to rely upon more than

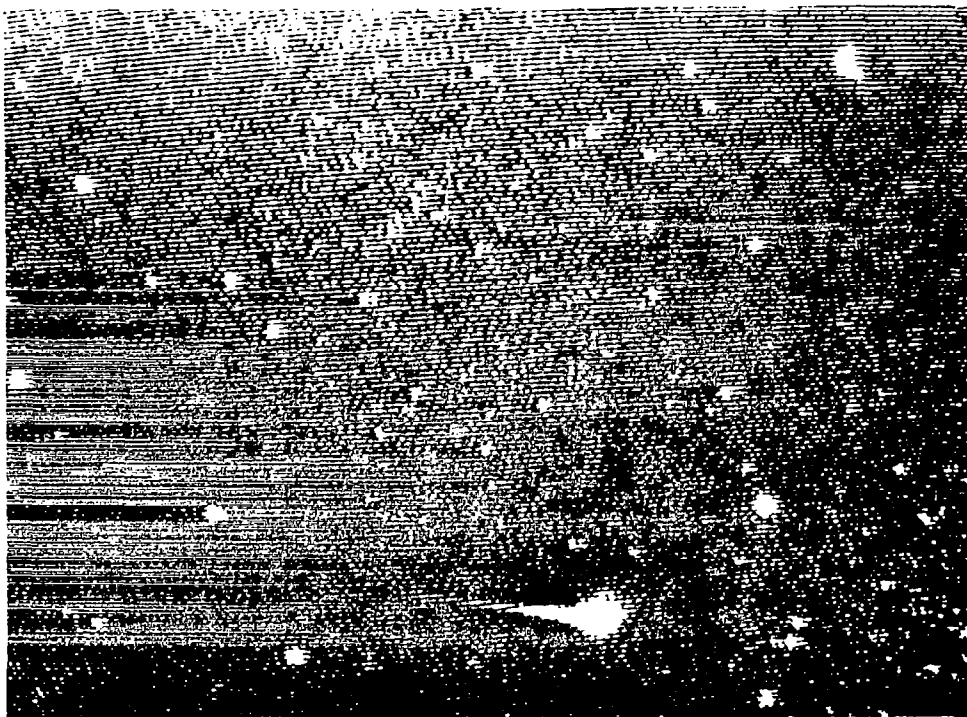


Figure 2. A meteor as observed by the image orthicon system.

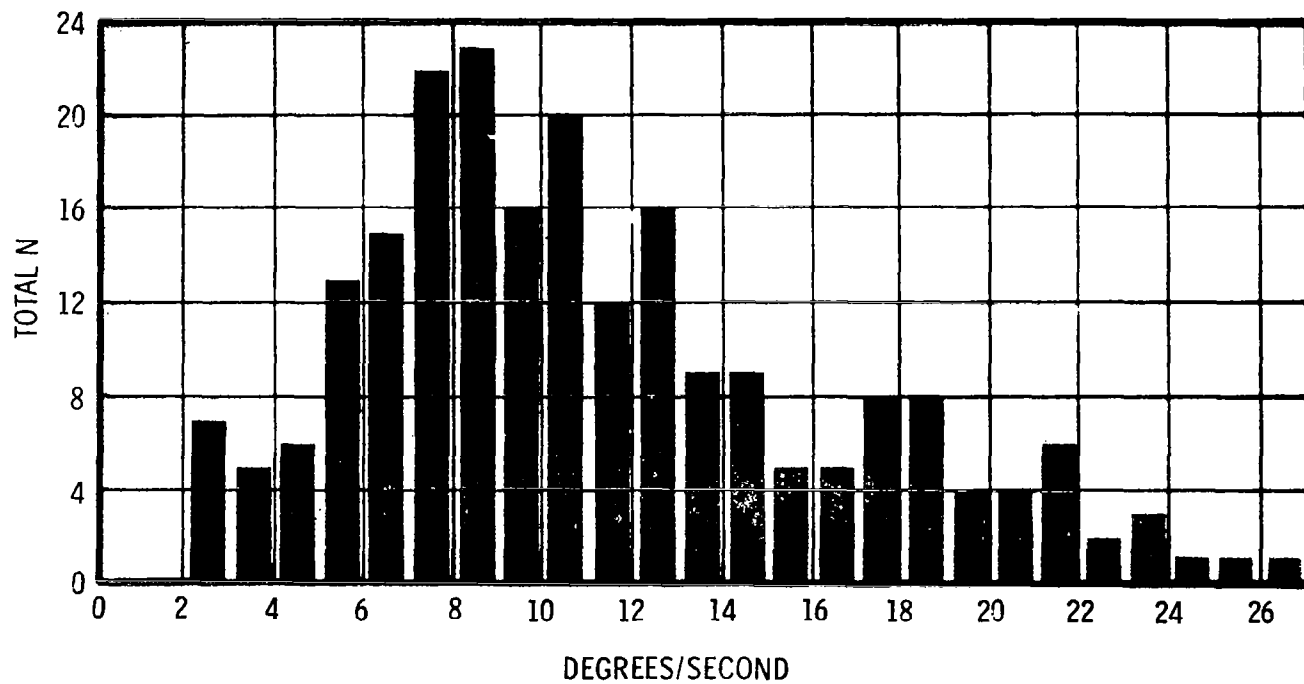


Figure 3. An angular rate distribution of meteors as recorded by the image orthicon during observations throughout November, 1969.

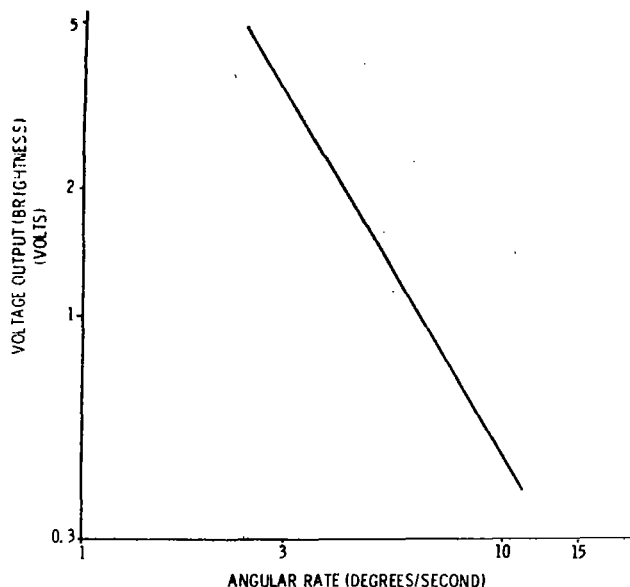


Figure 4. The decrease in apparent brightness of an object with increasing angular velocity.

one method of brightness determination. Basically, the voltage output of a meteor will define its magnitude when a comparison is made with stars of known magnitude panned across the field of view at known rates.

At present, analysis is accomplished by viewing the television monitor with a photomultiplier tube. The face of the monitor is masked off except for a small slit through which the passage of the meteor may be observed. A peak-height light curve is then read from the photomultiplier tube by a storage oscilloscope. A typical light curve of a bright meteor is shown in Figure 5. Forty such light curves have been obtained. This method works for brighter meteors, and meteor brightnesses have been determined to the seventh magnitude. Fainter meteors are lost in the background noise and must be examined by an alternate method.

By the end of the summer, a second television system, an SEC vidicon, will complement our observations. Using the two systems stationed at different sites, the meteor orbit, velocity, and height may be

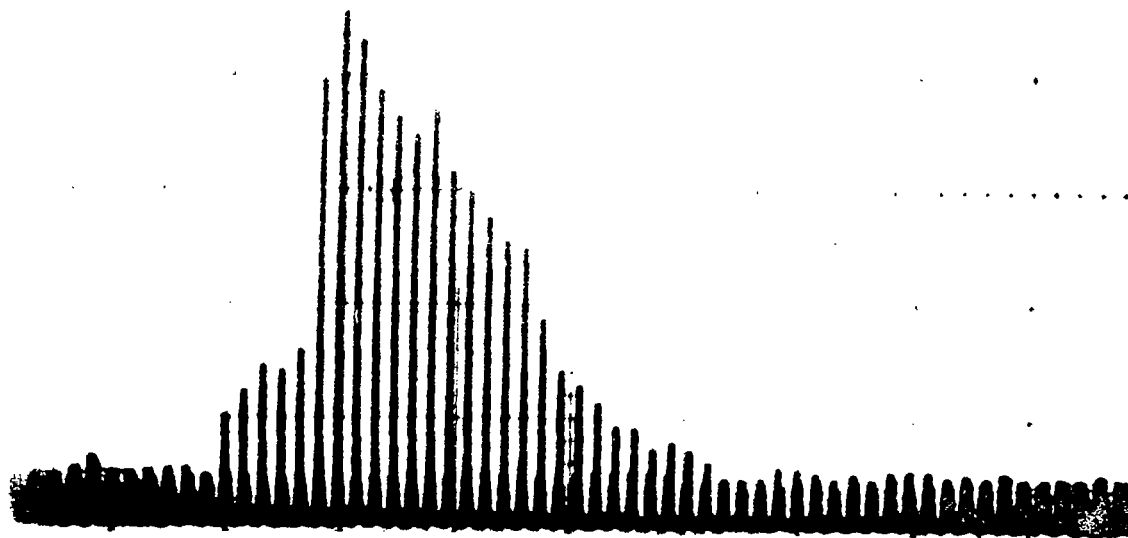


Figure 5. A typical peak-height light curve as recorded by a photomultiplier tube observing the television monitor.

calculated in addition to the information already recorded. The use of the two systems will also allow

investigations to be made into other areas of low light level astronomy.

N70-35514

PHOTOELECTRIC OBSERVATIONS OF METEORS TO 6.4 MAGNITUDE

By

R. J. Naumann

SUMMARY

A photoelectric technique for detection and photometric measurement of meteors has been demonstrated. Through this technique meteors as faint as 6.4 magnitude have been observed, although sky conditions at the present observing site limit the useful sensitivity to approximately 5.0 magnitude. The present observations indicate somewhat higher influx than expected by extrapolation of the photographic results, but the limited observations to date do not allow a determination of whether this result is caused by shower effects or by difference in calibration techniques.

INTRODUCTION

The definition of the meteoroid environment has been the object of a considerable effort within NASA. The presently accepted environment [1] depends heavily on photographic and visual observations to define the influx of the larger masses. The observational limit of such techniques is approximately fifth magnitude, but the useful limit, beyond which the probability of detecting a meteor is substantially diminished, is approximately 2.5 magnitude. This corresponds to approximately 0.1 gm mass. The present NASA environment extrapolates from these data to the Pegasus data at 10^{-6} gm. The most critical region for large manned spacecraft is in the mass range of 10^{-2} to 10^{-4} gm, which is exactly in the middle of the five orders of magnitude extrapolation between existing data points. Since meteoroid impacts may represent the most serious hazard to long-term operation of large orbital space stations, it is imperative to refine our present knowledge of the meteoroid environment in this critical region.

The most obvious approach is to extend the existing photographic data to fainter magnitudes by using more sensitive equipment such as extremely low light level TV systems. The Meteoroid Physics

Branch of the Space Sciences Laboratory of Marshall Space Flight Center is currently using such a system that can observe meteors as faint as eighth magnitude. However, such magnitudes can only be obtained for meteors with slow angular rates. This is because a fast meteor spends only a small fraction of the integration time of the instrument in a single resolving element. Consequently, the difference in output of that element is small compared with statistical fluctuations in surrounding elements, and the contrast is too low to allow detection unless the intensity is substantially above threshold.

To supplement these TV observations and to aid in the photometry of meteors observed with video techniques, a 1.5-m searchlight mirror is used to image a portion of the sky on the photocathode of an Amperex 150 UVP photomultiplier tube. The output of the photomultiplier tube is displayed on a memory oscilloscope through a type 1A7A plug-in with the bandpass set for 0.1 to 100 Hz. This was done to eliminate the dc background and the high-frequency shot noise from the sky. Meteors passing the field of view are seen as a momentary increase in signal that is stored on the memory scope and photographed by the observer.

A similar technique was used by Davis [2] to determine color indices of meteors as faint as fourth magnitude. Davis' system used a much larger 120-mm photomultiplier tube with no optics. A 50-degree field of view was defined by an aperture above the tube. Our system is more sensitive because of the smaller field and larger light-gathering capability.

THEORETICAL LIMIT OF A PHOTOMULTIPLIER METEOR DETECTION SYSTEM

The determining factor in the limiting detectability of the system is the fluctuations in the background. These fluctuations occur because energy is quantized, and the arrival of these quanta is a purely random process. In any random process, if N events are

expected in some interval of time t , the standard deviation is $\pm\sqrt{N}$ (provided $N \gg 1$). In a photo-detector, photoelectrons are produced by photons within a certain energy range striking the photo-cathode. The number of electrons produced is ϵN_b where ϵ is the quantum efficiency and N_b is the number of photons within the energy range from the background.

The average current is

$$i_{av} = \frac{\epsilon N_b e}{t} = \epsilon \dot{N}_b e$$

where e is the electronic charge and \dot{N}_b is the average number of photons per unit time.

A standard deviation in i is

$$(\Delta i)_{rms} = \frac{\sqrt{\epsilon \dot{N}_b} e}{t}$$

Since $N_b = \dot{N}_b t$,

$$(\Delta i)_{rms} = e \sqrt{\frac{\epsilon \dot{N}_b}{t}}$$

Notice that the root mean square noise current can be reduced by increasing the measuring time t . This is equivalent to reducing the bandwidth of the system by excluding higher frequencies, since $t = (2\Delta f)^{-1}$.

Having defined the root mean square noise photocathode current, we now consider the signal current. If signal photons arrive at rate \dot{N}_s , the average signal current is

$$i_{sig} = \epsilon \dot{N}_s e$$

The signal-to-noise ratio is

$$SNR = \frac{i_{sig}}{(\Delta i)_{rms}} = \dot{N}_s \sqrt{\frac{\epsilon}{2\Delta f \dot{N}_b}}$$

If a randomly occurring signal is less than the noise, there is no way of detecting it. As the signal is made larger than the noise, the detection probability is increased. A signal-to-noise ratio of five is generally considered sufficient to assure detection. This is equivalent to rejection of all but five sigma statistical fluctuations.

Amplification will increase both signal and noise while adding additional noise. It will be assumed here that the added noise is negligible so that the system will be limited by the fundamental quantum noise at the input. This, of course, will set an upper limit on the performance of the system which no amount of design can surpass.

Let us now turn to the task of computing the noise background \dot{N}_b and the signal \dot{N}_s . The rate at which signal photons strike the detector is

$$\dot{N}_s = (\text{collecting area})$$

$$\times (\text{flux of photons within the proper spectral region})$$

It is useful to describe the source in terms of stellar magnitude. By definition of stellar magnitude, the intensity of an M th magnitude object is related to a zero magnitude object by

$$I(M) = I(0) 10^{-0.4M}$$

A zero magnitude star produces a spectral flux of $3 \times 10^{-8} \text{ W/m}^2/\mu$ on earth at a wavelength of 0.5μ . Assume that this spectral flux is constant over a small $\Delta\lambda$ centered about 0.5μ . The energy flux from an M th magnitude object within spectral range $\Delta\lambda$ is

$$I = 3 \times 10^{-8 - 0.4M} \Delta\lambda \text{ W/m}^2$$

To convert this to number of photons, we must divide by the average energy of a photon. A photon with a wavelength of 0.5μ has an energy of

$$E = \frac{hc}{\lambda} = \frac{6.63 \times 10^{-34} \times 3 \times 10^8}{0.5 \times 10^{-6}} \text{ J}$$

$$E = 4 \times 10^{-19} \text{ J}$$

Therefore,

$$\dot{N}_s = \frac{\pi d^2}{4} \times 0.75 \times 10^{11-0.4M} \Delta\lambda \frac{\text{photons}}{\text{sec}},$$

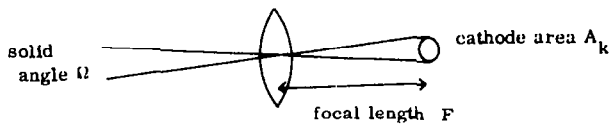
where $\Delta\lambda$ is in microns, and d is the diameter of the objective lens in meters.

The background sky is an extended source and therefore the \dot{N}_b is

$$\begin{aligned} \dot{N}_b &= (\text{collecting area}) \\ &\times (\text{no. of photons/area/solid angle}) \\ &\times (\text{solid angle seen by detector}) \end{aligned}$$

The steradiancy, or brightness, of the sky is often expressed in terms of a sky index, N_{10} , the equivalent number of 10th-magnitude stars per square degree. From the result derived above, the number of photons in interval $\Delta\lambda$ centered at 0.5μ from a 10th-magnitude star is $0.75 \times 10^7 \Delta\lambda$ photon/sec/m².

The solid angle subtended by the photocathode depends on the focal length and the photocathode area,



By definition of solid angle and the fact that rays pass through the vertex of the lens undeviated,

$$\Omega = \frac{A_k}{F^2} \text{ sr}$$

Since 1 degree is 0.01745 radian, one square degree subtends $(0.01745)^2$.

Finally,

$$\begin{aligned} \dot{N}_b &= \frac{\pi d^2}{4} (\text{m}^2) \\ &\times 0.75 \times 10^7 \Delta\lambda \left(\frac{\text{photons}}{\text{sec m}^2 \text{ 10th mag star}} \right) \\ &\times N_{10} \left(\frac{\text{10th mag star}}{\text{deg}^2} \right) \times \frac{A_k}{(0.01745)^2 F^2} \text{ deg}^2. \end{aligned}$$

To extend to as faint objects as possible, it is evident that d must be as large as practical, ϵ should be as large as possible, $\Delta\lambda$ as large as possible, and N_{10} as small as possible. Decreasing the solid angle will increase the sensitivity, and will also limit the number of events seen. This will be considered later.

The present system uses a photomultiplier tube with broad response to increase $\Delta\lambda$ and a large area searchlight mirror. Approximate values are

$$d = 1.5 \text{ m}$$

$$F = 0.5 \text{ m}$$

$$A_K = \frac{\pi (0.032)^2}{4} \text{ m}^2$$

$$\epsilon = 0.15 \text{ electrons/photon}$$

$$\Delta\lambda = 0.1\mu$$

$$N_{10} = 2000 \text{ 10th magnitude stars/deg}^2.$$

The solid angle is

$$\Omega = \frac{\pi (0.032)^2}{4 \cdot 5^2 (0.01745)^2} = 10.5 \text{ deg}^2$$

The area of the collector is

$$\text{Area} = \frac{\pi(1.5)^2}{4} = 1.76 \text{ m}^2$$

$$\dot{N}_b = 1.76 \times 0.75 \times 10^7 \times 0.1 \times 2000 \times 10.5$$

$$= 2.8 \times 10^{10} \text{ photons/sec}$$

$$\dot{N}_s = 1.76 \times 0.75 \times 10^{11-0.4M} \times 0.1$$

$$= 1.32 \times 10^{10-0.4M} \text{ photons/sec}$$

$$i_{av} = 2.8 \times 10^{10} \times 15 \times 1.6 \times 10^{-19}$$

$$= 0.67 \times 10^{-9} \text{ A}$$

$$(\Delta i)_{rms} = 1.6 \times 10^{-19} \sqrt{0.15 \times 2.8 \times 10^{10} \Delta f}$$

$$= 1.47 \times 10^{-14} \sqrt{\Delta f A}$$

With a bandpass of 100 Hz, the root mean square background is $1.47 \times 10^{-13} \text{ A}$ at the photocathode. The faintest meteor that could be detected against this background is obtained by requiring

$$\text{SNR} = \dot{N}_s \sqrt{\frac{\epsilon}{2\Delta f \dot{N}_b}} = 5$$

or

$$1.32 \times 10^{10-0.4M} = 5 \sqrt{\frac{2.8 \times 10^{10} \times 2 \times 100}{0.15}}$$

$$1.32 \times 10^{10-0.4M} = 30.6 \times 10^6$$

Taking logarithms,

$$10 - 0.4M = \log 23.2 + 6 = 7.364$$

$$0.4M = 2.636$$

$$M_{Lim} = 6.6$$

The ultimate performance of this technique may be estimated by considering possible improvements. The expression for limiting magnitude is

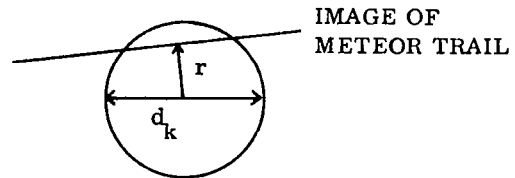
$$M_{Lim} = \text{const} + 1.25 \log \left(\frac{\epsilon d^2 \Delta \lambda}{N_{10} \Omega \Delta f} \right)$$

Not much improvement can be expected in ϵ or $\Delta \lambda$. The collecting area is as large as can be obtained for a reasonable cost. The biggest potential gain lies in the sky background, N_{10} . The value of 2000 was used for the vicinity of Huntsville. An improvement factor of four could be realized by moving the system to a darker site which would increase the limiting magnitude by 0.75. The solid angle could be reduced by using a smaller photocathode or a longer focal length. However, this is accompanied by a reduction in data acquisition rate since a smaller area is viewed and by increased bandwidth requirements if the meteor duration is limited by the field of view.

The transit time of a meteor across the field of view is

$$t = \frac{d_k}{\omega F} \left(1 - \frac{(2r)^2}{d_k^2} \right)^{1/2}$$

where d_k is the diameter of the photocathode, F is the focal length, ω is the angular rate, and r is the smallest distance from the center of the photocathode to the image of the meteor trail.



But

$$\left(1 - \frac{4r^2}{d_k^2} \right)^{1/2} = \left(1 - \frac{Ar}{A_k} \right)^{1/2}$$

where Ar is the area included by radius r . Setting this radical to a value of 0.1 assures that 99 percent of all meteors within the field will have transit times greater than

$$t = \frac{d_k^{0.1}}{F\omega} = \frac{3.2}{500\omega} = \frac{6.4}{\omega} \text{ ms}$$

For $\omega_{\max} = 0.7 \text{ rad/sec}$, the shortest time that need be considered is 9 ms. The minimum bandwidth is $\sim 50 \text{ Hz}$.

The product $\Omega\Delta f$ must therefore be considered together. Since

$$\Delta f = \frac{1}{2t} = \frac{F \cdot 0.7}{2d_k^{0.1}} = \frac{3.5 F}{d_k}$$

and

$$\Omega \sim \frac{d_k^2}{F^2}$$

then

$$\Omega\Delta f \sim \frac{d_k}{F}$$

Thus sensitivity can be improved by 0.375 magnitudes by reducing d_k/F by two, but the field of view and data acquisition rate are reduced by a factor of four.

The practical limit would then appear to be the present system using an 11-mm photomultiplier, a bandwidth of 100 Hz^1 (which will still accommodate 97 percent of even the fastest meteors) in a location with sky index of 500. This will gain

0.75 magnitudes from better sky
1.16 magnitude from smaller solid angle
<hr/>
1.91 total gain
6.60 existing system
<hr/>

$$M_{\text{Lim}} = 8.51$$

The area will be reduced by a factor of nine, but this will be approximately compensated for by the increase in meteor population for decreasing size.

CALIBRATION

Since the system is always operated in a region where the anode current is small enough to assure linearity, the voltage observed can be related to the magnitude of a meteor by

$$V - V_b = (V_o - V_b) 10^{-0.4M}$$

where $V - V_b$ is the observed signal above background, $V_o - V_b$ is the voltage associated with a zero magnitude meteor above background, and M is the magnitude of the observed source. The quantity $V_o - V_b$ is obtained by calibration against known stars.

In practice, since the background sky in the 3-degree field of view is approximately the same as a zero magnitude star, the calibration star should be as bright as possible to reduce errors in obtaining the difference $V_{\text{obs}} - V_b$. Sirius is an ideal calibration star because of its -1.58 magnitude and also because it is a type A1 star for which photographic and visual magnitude nearly coincide. For this reason, no correction will be made for color index, and all meteor magnitudes will be referred to type A1 spectral class.

A calibration for a typical observing night is described. A recording, integrating digital voltmeter was used to minimize fluctuations from twinkling. An average of 19.364 V was obtained from Sirius. As Sirius moved out of the field, the reading dropped to 3.890 V. Thus,

$$19.364 - 3.890 = (V_o - V_b) 10^{-0.4(-1.58)}$$

$$V_o - V_b = 3.60$$

Several other stars were measured to check this calibration. The results are summarized in the following table:

1. For very faint meteors the duration may be limited by the meteor being consumed rather than by the field of view. For this reason 100 Hz is the smallest bandwidth that should be considered.

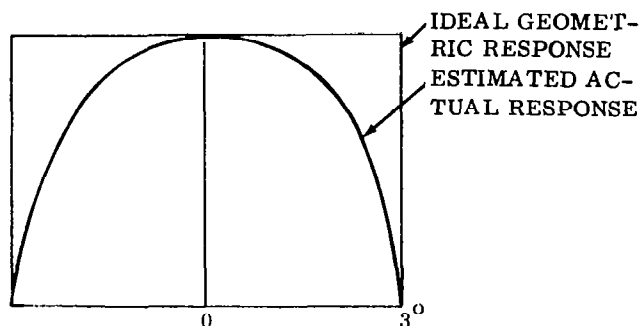
Star	Type	M_v	V_{obs}	V_b	M (calculated)
Capella	G8	0.21	6.40	3.51	0.24
Procyon	F5	0.48	5.92	4.12	0.753
Betelgeuse	M2	0.92	5.06	4.12	1.58
Pollux	K0	1.21	4.47	4.03	2.28
Castor	A1	1.58	4.69	4.03	1.84

The M(calculated) was found from

$$M_{cal} = 1.39 - 2.5 \log (V - V_b)$$

There are several possible reasons for the differences between M and M_v . Probably the major source of error lies in obtaining the sky background. For these stars the mirror was moved to a region adjacent to the star, and the voltage was read. A slight difference in the sky background will make a substantial error for the fainter magnitudes. Also, the different spectral classes can be expected to require increasing correction for increasing redness since the tube used has an S-13 UV response.

The sky index can be obtained by setting $V - V_b = V_{b(obs)}$. The $V_{b(obs)}$ ranged from 3.2 V at zenith to 4.12 V at an elevation of approximately 30 degrees. This corresponds to 0.128 magnitude at zenith and -0.145 magnitude at 30-degrees elevation. In terms of 10th-magnitude stars/deg², assuming a field of 10.5 deg², the sky index is 850 at zenith and 1100 at 30 degrees. These are probably low for the sky in the vicinity of Huntsville, where fourth-magnitude stars are barely visible to the eye. The response of the system falls off with angle before the geometric limit is reached because of spherical aberration. The exact shape of the response curve has not yet been determined, but from observing stellar transits, the response appears to be parabolic in nature with the vertex on the optical axis and the intercept at the geometric limit. It is estimated that the effective solid angle is 50 to 67 percent of the geometric solid angle.



This correction will increase the sky index to 1500 through 2000.

A substantial portion of the sky background is backscatter from Huntsville lights. This is evident from the 120-Hz component in the sky background that is typical of mercury lamps (Fig. 1). This is averaged out in the calibration procedure by using an integration time of 1/60 sec, but, as will be seen later, this component severely hampers the detection of faint meteors.

METEOR OBSERVATIONS

For the preliminary results described in this report, meteors were detected by an observer monitoring the memory scope on slow scan. Typical meteors are shown in Figure 2. The broad band of noise of the 120-Hz component is caused by Huntsville mercury vapor lamps. Brighter meteors show up as a temporary level shift. However, fainter meteors of short duration can be detected only if their peak intensity coincides with a peak in the background. This caused many of the fainter

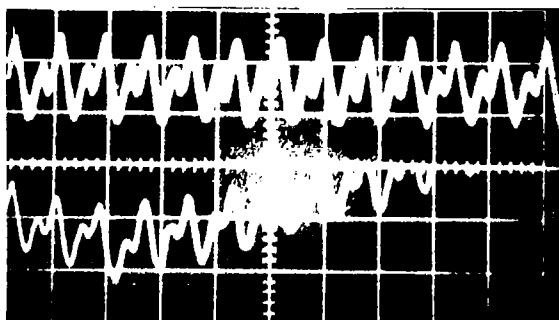


Figure 1. 120-Hz sky background and level shift caused by a 3.45 magnitude meteor (50 mV/cm, 10 ms/cm).

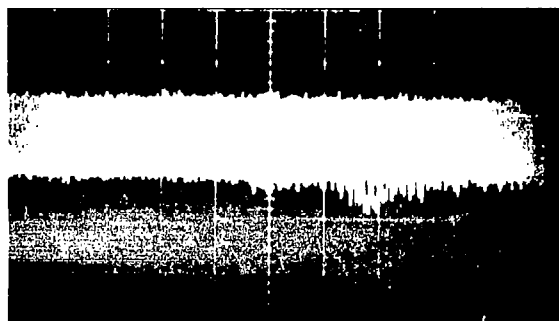


Figure 2b. 5.16-magnitude meteor (50 mV/cm, 50 ms/cm).

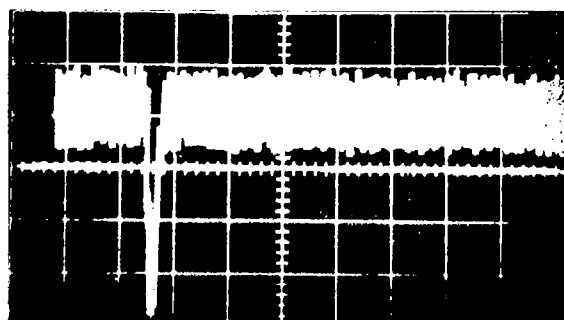


Figure 2a. Typical meteors observed — 3.58-magnitude meteors (50 mV/cm, 100 ms/cm).

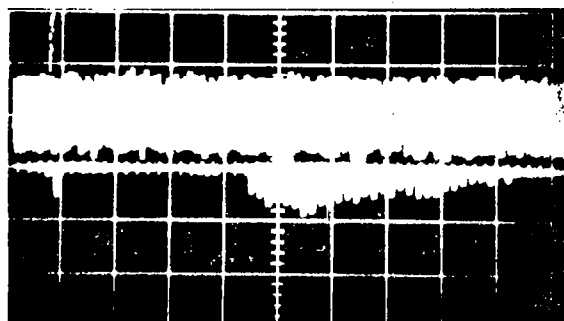


Figure 2c. 4.5-magnitude meteor (50 mV/cm, 50 ms/cm).

meteors to be missed, as can be seen in the histogram (Fig. 3). Apparently, detection probability diminishes beyond fifth magnitude. This, of course, can be rectified by observing from a site with better viewing conditions and by using electronic techniques to trigger a counter when an event occurs that is 5X background noise. The goal for the present phase was to demonstrate that the technique could be used to extend optical meteor data to fainter magnitudes.

The results of 18 hours of observation are listed in Table 1. The voltages associated with the meteors have been corrected for filter attenuation (Fig. 4), which was obtained experimentally by feeding pulses of various shapes and duration into the system and observing the ratio of the observed pulse to input pulse. The voltages were then converted to magnitude using the calibration result

$$M = 1.39 - 2.5 \log_{10} (V - V_b) .$$

The results of these observations are plotted along with those of Hawkins and Upton [3] in Figure 5. The area was obtained by taking the portion of sky included in 10.5 deg^2 at a distance of 100 km.

It is interesting to note that the present study compares reasonably with the extrapolated results of Hawkins and Upton. The slope indicated by the observed data is practically identical with that deduced by Hawkins and Upton. The present observations indicate an influx rate about a factor of three to four higher than expected from extrapolating the Hawkins and Upton curve. It is not yet certain that this is real. The present observations were made over a limited time (approximately 1 month), and it is known that fluctuations occur from month to month. The observations also contain the time of the Geminids shower which may have added significantly to the number observed. At present, limited statistics do not allow a determination of the effect of showers. There is also the problem of definition

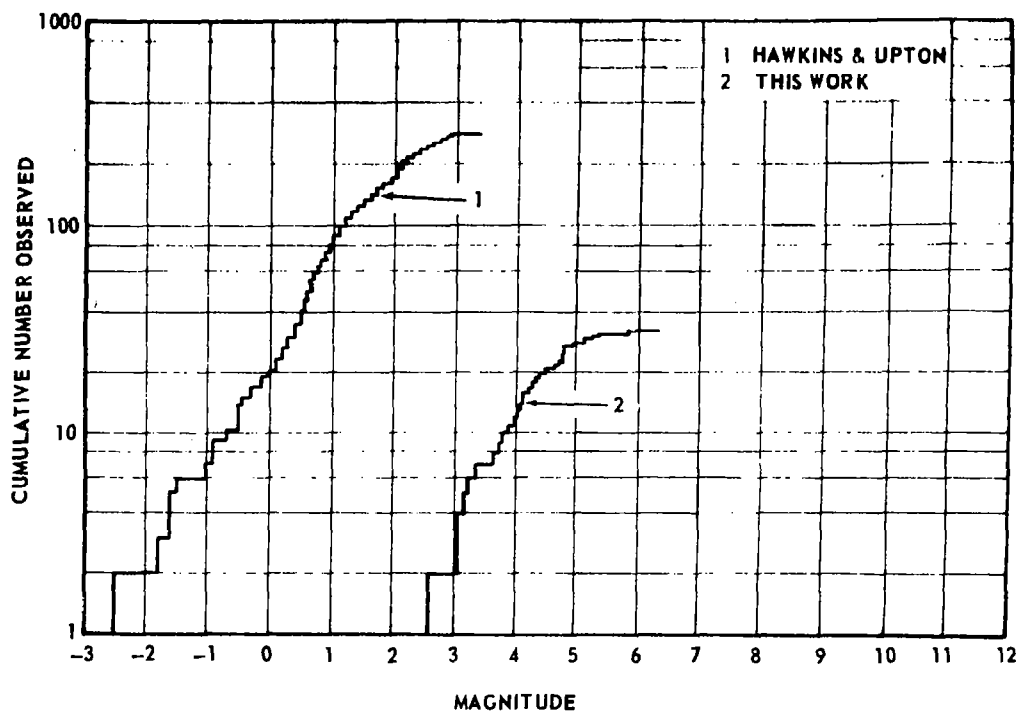


Figure 3. Results of this study compared with photographic work of Hawkins and Upton.

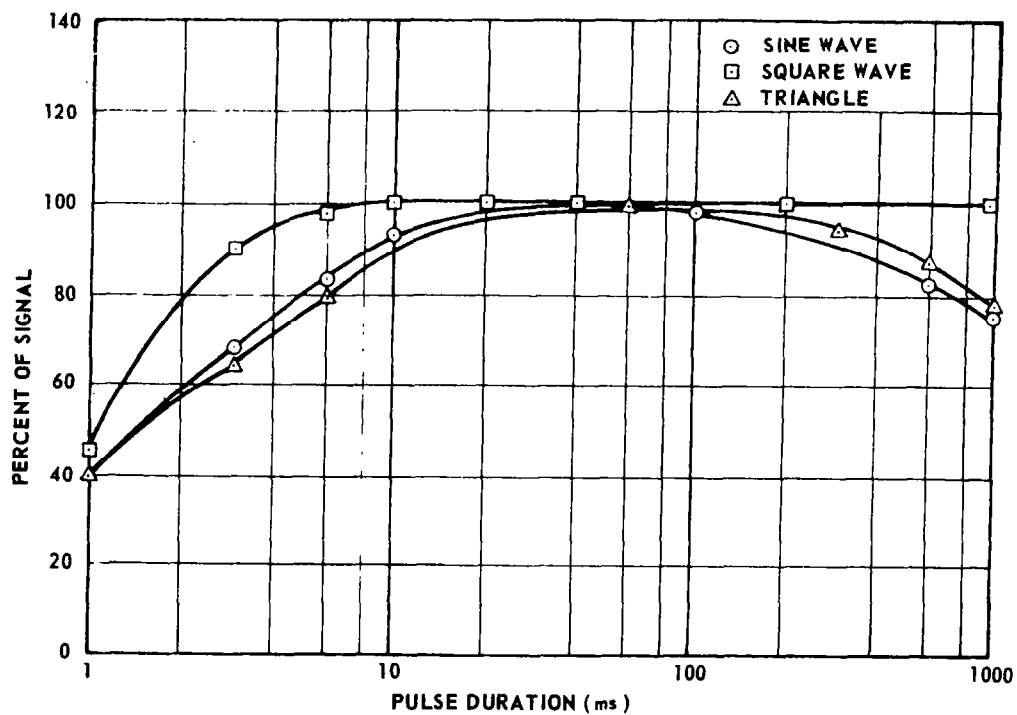


Figure 4. Filter attenuation at different pulse durations.

TABLE 1. METEORS OBSERVED IN 17 HOURS, 22 MINUTES OBSERVING TIME

No.	Time	dc Level V	Pulse Height mV	Duration msec	Magnitude
<u>11-20-68</u>					
1	12:45	4.5	187	150	3.22
<u>11-21-68</u>					
2	1:25	4.15	150	100	3.45
3	1:34	4.00	90	94	4.01
4	2:12	3.85	41	80	4.86
5	2:45	3.85	12	34	4.86
<u>11-22-68</u>					
6	12:05	3.0	500	150	2.14
7	12:36	4.1	160	80	3.58
8	12:40	4.1	170	60	3.32
9	12:45	4.1	57	380	4.50
9a	12:45	4.1	36	26	5.00
10	1:02		75	52	4.20
11	1:50	3.0	13	13	6.11
12	1:58	3.0	322	80	2.62
<u>12-13-68</u>					
13	10:05	3.7	95	42	3.95
14	11:10	4.6	25	226	5.40
15	10:40	3.7	171	19	3.27
16	10:45	3.7	40	226	4.89
17	10:47	3.6	10	42	6.39
18	11:03	3.5	70	17	4.28
19	11:15	3.5	208	47	3.09
20	12:00	4.2	62	80	4.41
21	12:15	3.9	60	316	4.44
22	12:32	4.1	82	190	4.11
23	12:45	3.9	102	270	3.87
<u>12-16-68</u>					
24	9:00	5.2	107	26	3.82
25	9:03	5.2	35	231	5.03
26	9:05	5.0	60	35	4.44
27	9:36	4.4	43	10	4.81
28	9:37	4.4	40	210	4.89
29	9:40	4.4	71	42	4.26
30	9:41	4.4	70	37	4.28
31	12:20	4.7	50	90	4.64
<u>1-13-69</u>					
(9:05 - 12:00)					
32	8:56	4.01	27	80	5.31
33	10:03	3.87	31	150	5.16
34	11:06	3.62	41	21	4.86

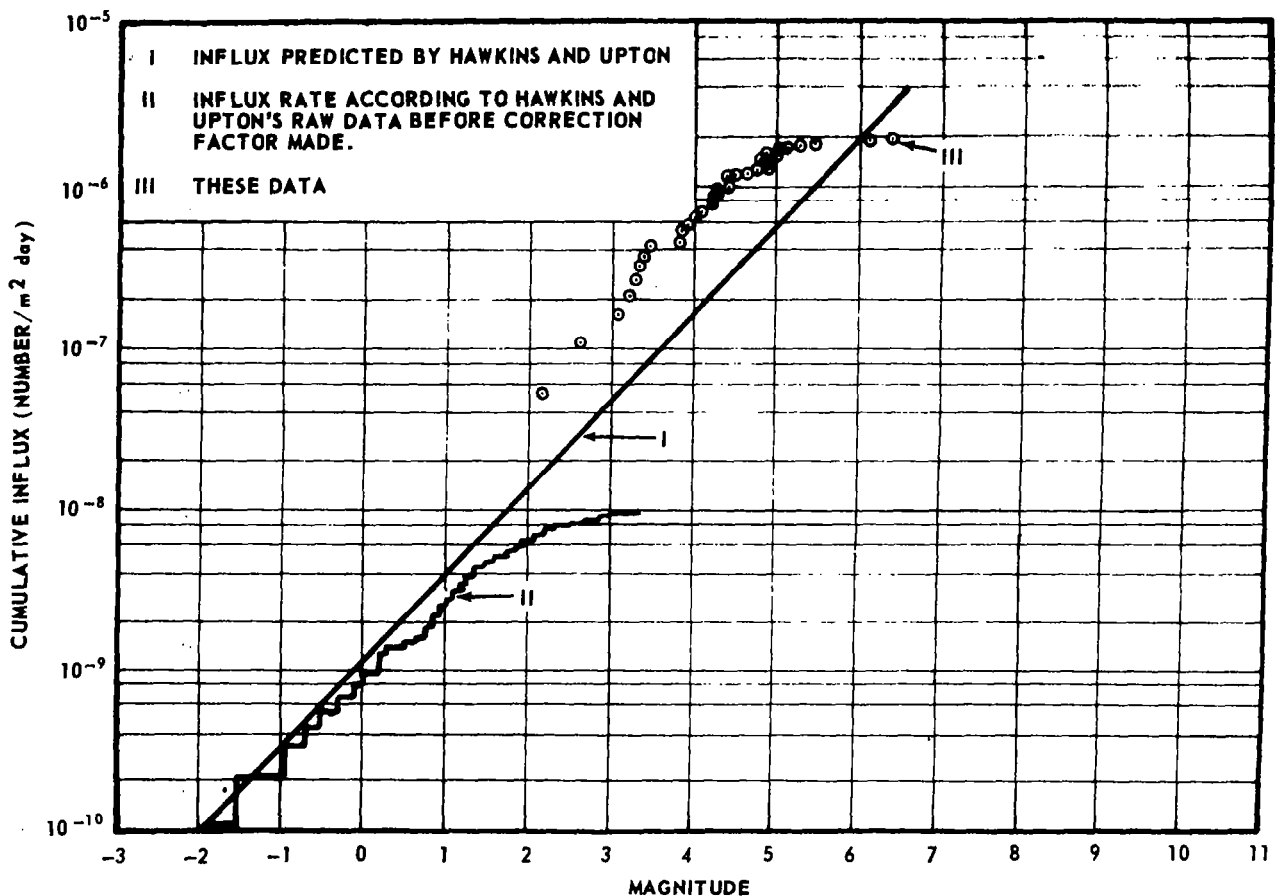


Figure 5. Influx rates of this study compared with those observed by Hawkins and Upton.

of magnitude since our system has a response different from that of photographic film.

CONCLUSIONS

The use of a photomultiplier tube and a large objective mirror appears to be a useful technique

for counting and obtaining photometric data for faint meteors. The present study extended the Hawkins and Upton results from 2.5 to 5.0 magnitude. Meteors near the theoretical limit of 6.6 were observed but with low detection probability. The technique appears to have an ultimate capability of 8.51, which corresponds to masses of 4×10^4 gm.

REFERENCES

1. Models of the Meteoroid Environment — 1969 (Near Earth to Lunar Surface). NASA SP-8013, National Aeronautics and Space Administration, Washington, D. C., 1969.
2. Davis, John: Photoelectric Meteor Observations and the Colour Indices and Visual Magnitudes of Meteors. Astronomical Contributions, Univ. of Manchester, vol. 126, 1963, pp. 445-467.
3. Hawkins, G. S.; and Upton, E. K. L.: The Influx Rate of Meteors in the Earth's Atmosphere. Astrophys. J., vol. 128, no. 3, July - Nov., 1958, pp. 727-735.

OBSERVATORY PLANS AND ASTRONOMICAL APPLICATIONS

By

James McGuire

The observatory constructed at the southern end of Redstone Arsenal was developed to improve the meteor observation program at MSFC and to aid in developing other astronomical programs. The area for the site, shown in Figure 1, was selected because of its favorable location and the good visibility conditions present. Table 1 shows that the observational conditions in the Huntsville area are more desirable than at 50 percent of the other observatory sites in the United States. The data in this table were obtained from the U. S. Weather Bureau and a Brown Engineering Company report.

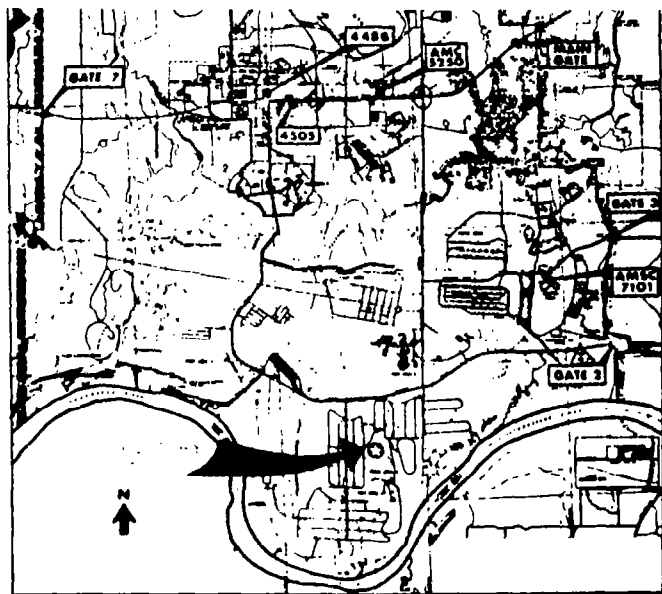


Figure 1. Location of observatory site at Redstone Arsenal.

The views of the horizon observed from the site are shown in Figures 2 through 5. Figure 2 is a view of the eastern horizon; Figure 3, the southern horizon; Figure 4, the western horizon; and Figure 5 is a view of the northern horizon. The building shown in Figure 2 is not a part of the observatory, but belongs to the Army. The site is atop a hill approximately 300 feet tall, the same height as the vibration test tower pictured in the background of Figure 5.

TABLE 1. OBSERVATIONAL CONDITIONS OF OBSERVATORY SITE

Sky Glow:	40 percent better than Monte Sano; 40 percent worse than the best location within 30 miles of Huntsville.
Resolution Limitation:	0.15 second of arc
Clear Nights:	15 percent better here than for the average eastern and midwestern observatory; 15 percent worse here than for the average western observatory.

Two telescopes and two domes will be used when the site becomes operational. The domes are made by Ash-Domes Corporation; the larger is 18 feet in diameter and the smaller, shown in Figure 6, is 12 feet in diameter. One of the telescopes is manufactured by Ferson and has a 16-inch primary mirror (Fig. 7). This model can be used as a Newtonian telescope with a 53-minute field of view or as a Cassegrain telescope with a 15-minute field of view. The second telescope, shown in Figure 8, was made by Celestron Pacific and is also a 16 inch. This telescope is similar to a Schmidt telescope since it has a correcting lens for the spherical primary mirror. The advantage of this type of telescope is that it is a closed system and is therefore easier to keep clean and is not affected by heat waves in the telescope tube. When used in the Cassegrain mode, this telescope has a 20-minute field of view. The Celestron telescope also has a rich field adaptor that will allow a 1-degree field of view.

The instruments to be used on the telescope will be low light level TV systems, photographic equipment in conjunction with image intensifiers, photometric equipment, and, possibly, a spectrograph. Figure 9 shows a Celestron telescope with a low light level TV camera attached and the rich field adaptor being used.

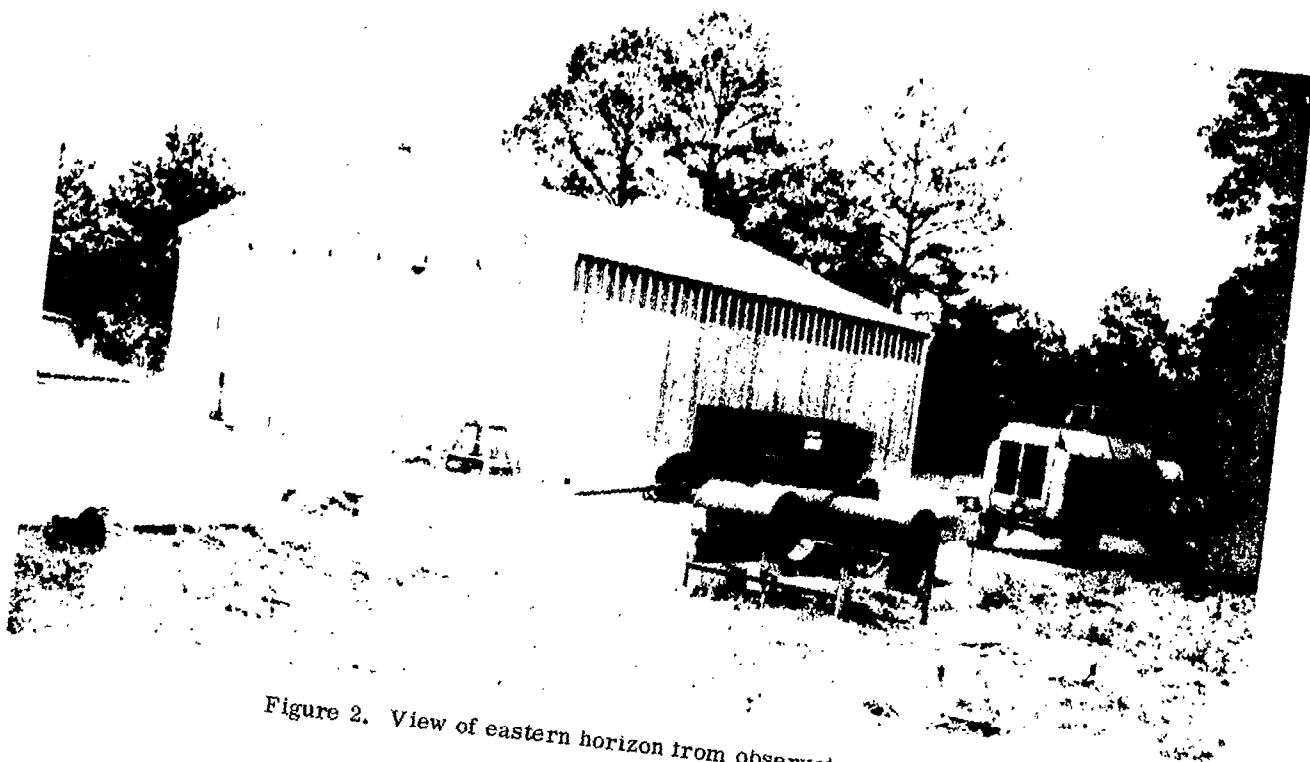


Figure 2. View of eastern horizon from observatory site.

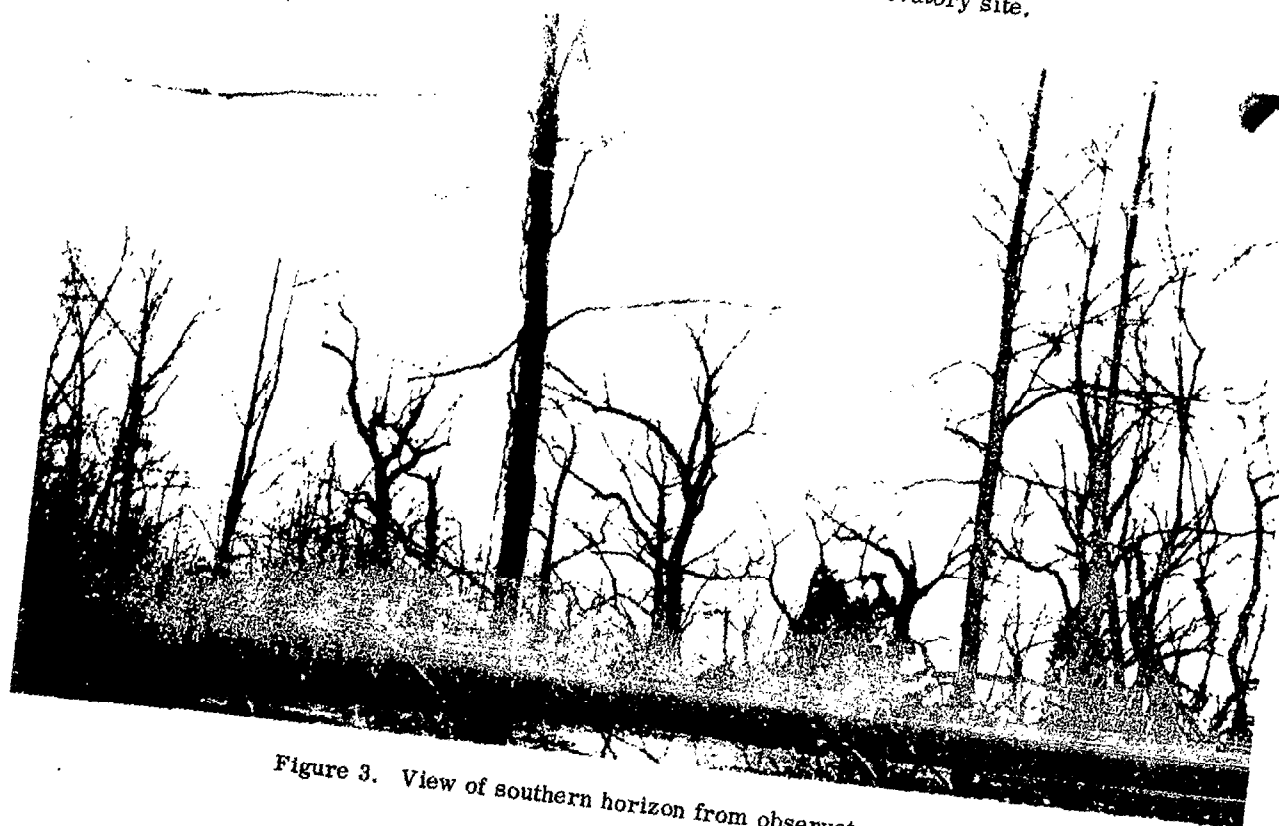


Figure 3. View of southern horizon from observatory site.



Figure 4. View of western horizon from observatory site.



Figure 5. View of northern horizon from observatory site.

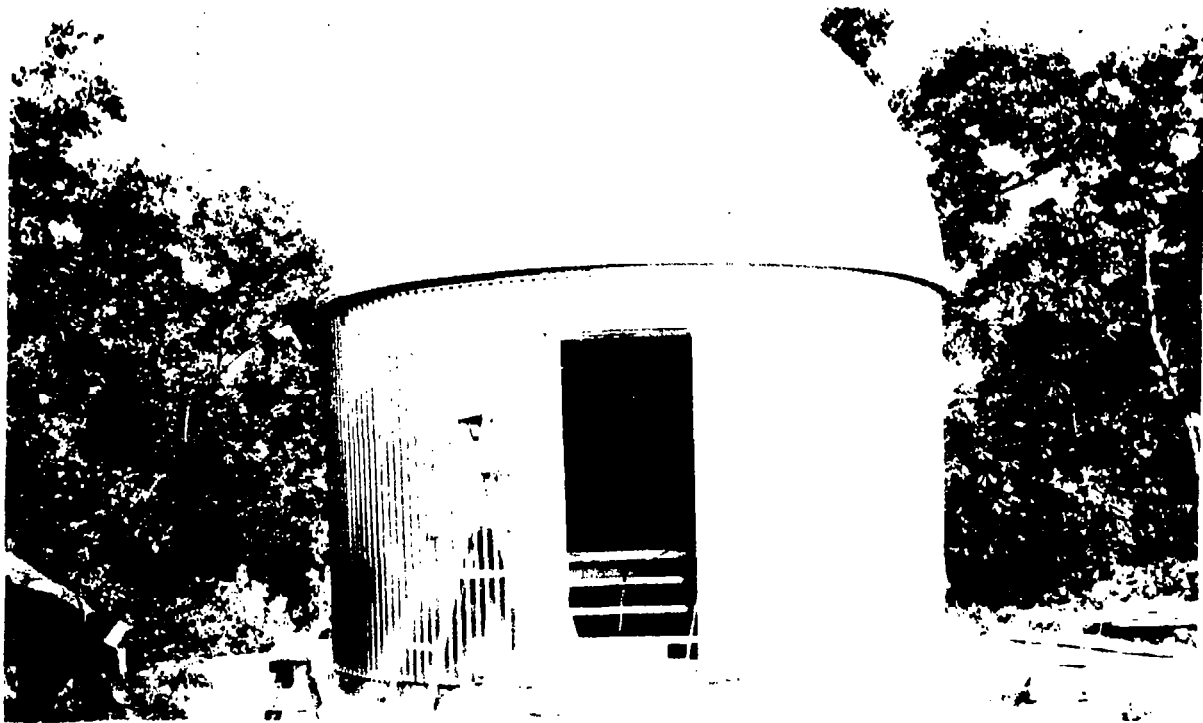


Figure 6. 12-foot diameter dome located at observatory site.

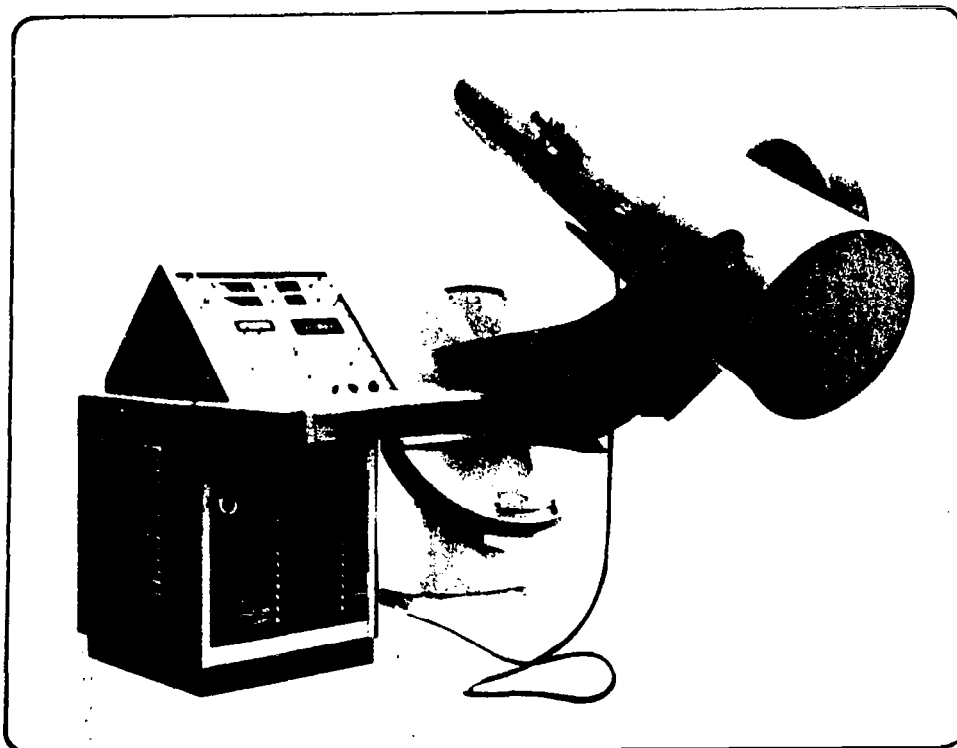


Figure 7. Ferson telescope having a 16-inch primary mirror.



Figure 8. Celestron Pacific telescope.

It is hoped that astronomical observations of meteors can be extended to the 11th magnitude with these telescopes. The Ferson model is now being

used to obtain photometric data on eclipsing binary systems. In the future, such objects as comets, novae, and nebulae could be studied using these telescopes.

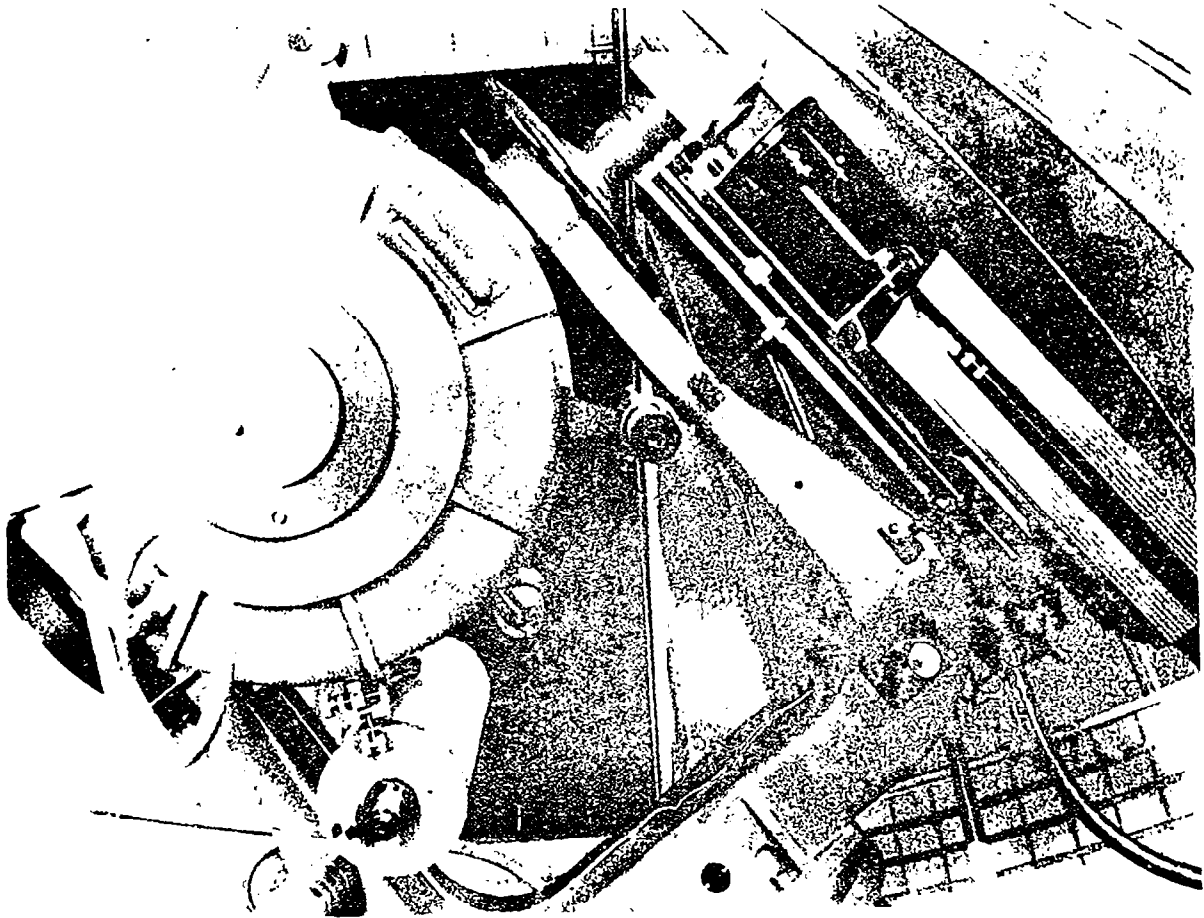
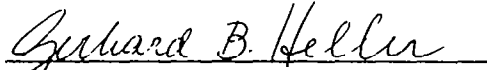


Figure 9. Celestron telescope with a low light level TV camera and rich field adaptor attached.

RESEARCH ACHIEVEMENTS REVIEW
VOLUME III REPORT NO. 8

The information in these reports has been reviewed for security classification. Review of any information concerning Department of Defense or Atomic Energy Commission programs has been made by the MSFC Security Classification Officer. These reports, in their entirety, have been determined to be unclassified.

These reports have also been reviewed and approved for technical accuracy.


GERHARD B. HELLER
Director, Space Sciences Laboratory

MSFC-RSA, Ala

UNITS OF MEASURE

In a prepared statement presented on August 5, 1965, to the U. S. House of Representatives Science and Astronautics Committee (chaired by George P. Miller of California), the position of the National Aeronautics and Space Administration on Units of Measure was stated by Dr. Alfred J. Eggers, Deputy Associate Administrator, Office of Advanced Research and Technology:

"In January of this year NASA directed that the international system of units should be considered the preferred system of units, and should be employed by the research centers as the primary system in all reports and publications of a technical nature, except where such use would reduce the usefulness of the report to the primary recipients. During the conversion period the use of customary units in parentheses following the SI units is permissible, but the parenthetical usage of conventional units will be discontinued as soon as it is judged that the normal users of the reports would not be particularly inconvenienced by the exclusive use of SI units."

The International System of Units (SI Units) has been adopted by the U. S. National Bureau of Standards (see NBS Technical News Bulletin, Vol. 48, No. 4, April 1964).

The International System of Units is defined in NASA SP-7012, "The International System of Units, Physical Constants, and Conversion Factors," which is available from the U. S. Government Printing Office, Washington, D. C. 20402.

SI Units are used preferentially in this series of research reports in accordance with NASA policy and following the practice of the National Bureau of Standards.

CALENDAR OF REVIEWS

FIRST SERIES (VOLUME I)

REVIEW	DATE	RESEARCH AREA	REVIEW	DATE	RESEARCH AREA
1	2/25/65	RADIATION PHYSICS	12	9/16/65	AERODYNAMICS
2	2/25/65	THERMOPHYSICS	13	9/30/65	INSTRUMENTATION
3	3/25/65	CRYOGENIC TECHNOLOGY	14	9/30/65	POWER SYSTEMS
4 *	3/25/65	CHEMICAL PROPULSION	15	10/28/65	GUIDANCE CONCEPTS
5	4/29/65	ELECTRONICS	16	10/28/65	ASTRODYNAMICS
6	4/29/65	CONTROL SYSTEMS	17	1/27/66	ADVANCED TRACKING SYSTEMS
7	5/27/65	MATERIALS	18	1/27/66	COMMUNICATIONS SYSTEMS
8	5/27/65	MANUFACTURING	19	1/6/66	STRUCTURES
9	6/24/65	GROUND TESTING	20	1/6/66	MATHEMATICS AND COMPUTATION
10	6/24/65	QUALITY ASSURANCE AND CHECKOUT	21	2/24/66	ADVANCED PROPULSION
11	9/16/65	TERRESTRIAL AND SPACE ENVIRONMENT	22	2/24/66	LUNAR AND METEOROID PHYSICS

SECOND SERIES (VOLUME II)

REVIEW	DATE	RESEARCH AREA	REVIEW	DATE	RESEARCH AREA
1	3/31/66	RADIATION PHYSICS	7	3/30/67	CRYOGENIC TECHNOLOGY
2	3/31/66	THERMOPHYSICS	8 **	5/25/67	COMPUTATION
3	5/26/66	ELECTRONICS	9	7/27/67	POWER SYSTEMS
4	7/28/66	MATERIALS	10	9/28/67	TERRESTRIAL AND SPACE ENVIRONMENT
5	9/29/66	QUALITY AND RELIABILITY ASSURANCE	11	11/30/67	MANUFACTURING
6	1/26/67	CHEMICAL PROPULSION	12	1/25/68	INSTRUMENTATION RESEARCH FOR GROUND TESTING

THIRD SERIES (VOLUME III)

REVIEW	DATE	RESEARCH AREA	REVIEW	DATE	RESEARCH AREA
1	3/28/68	AIRBORNE INSTRUMENTATION AND DATA TRANSMISSION	6	1/30/69	THERMOPHYSICS
2	5/22/68	ASTRODYNAMICS GUIDANCE AND OPTIMIZATION	7	3/27/69	RADIATION PHYSICS
3	7/25/68	CONTROL SYSTEMS	8	6/28/69	METEOROID PHYSICS
4	9/26/68	AEROPHYSICS	9	9/25/69	COMPUTATION RESEARCH
5	11/21/68	COMMUNICATION AND TRACKING	10	12/18/69	MATERIALS RESEARCH FOR SHUTTLE AND SPACE STATION
			11	1/29/70	MICROELECTRONICS RESEARCH FOR SHUTTLE AND SPACE STATION
			12	3/26/70	COMPUTATION RESEARCH

* Classified. Proceedings not published.

** Proceedings summarized only.

Correspondence concerning the Research Achievements Review Series should be addressed to:
Research Planning Office, S&E-R, Marshall Space Flight Center, Alabama 35812